

Dirac cones and defect charges

PhD thesis, Utrecht University, April 2018

About the cover: straws that form a hexagonal pattern

Printed by Proefschriftmaken

Dirac cones and defect charges

Dirac kegels en defect ladingen

(met een samenvatting in het Nederlands)

Proefschrift

ter verkrijging van de graad van doctor aan de Universiteit Utrecht op
gezag van de rector magnificus, prof.dr. H.R.B.M. Kummeling,
ingevolge het besluit van het college voor promoties in het openbaar
te verdedigen op woensdag 13 juni 2018 des middags te 2.30 uur

door

Guido Christiaan Paulus van Miert

geboren op 15 februari 1990
te Amstelveen

Promotor: Prof. dr. C. Morais Smith
Copromotor: Dr. C. Ortix

Contents

1	Introduction	1
1.1	Outline	8
2	Topological origin of edge states in 2D inversion-symmetric insulators and semi-metals	11
2.1	Symmetry of the Bloch Hamiltonian	12
2.2	Band topology in 1D	13
2.3	\mathbb{Z}_2 classification	14
2.4	Bulk-Boundary Correspondence	15
2.5	Surface Charge Quantization	18
2.6	Few-layer Black Phosphorus	22
2.7	Conclusion and Discussion	26
	Appendices	29
A.1	Relation between the Zak phase and eigenvalues of inversion .	29
A.2	Properties of Zak connection and curvature	30
A.3	Parameters for the two-band toy model	31
A.4	Tight-binding model corresponding to the band structure shown in Fig. 2.3	31
3	Berry phase approach to excess charges	33
3.1	Edge charge of 1D systems	35
3.1.1	Notation	36
3.1.2	Derivation	36
3.1.3	Termination dependence	42
3.1.4	Time-reversal symmetry	44
3.1.5	Numerical considerations	48
3.2	Edge charge as a probe of band structure topology	49
3.3	Conclusions	60
	Appendices	61

B		61
B.1	Relation between the Zak phase and the Berry phase	61
B.2	Current operator	61
4	Dislocation charges as probes of crystalline topology	65
4.1	Berry phase formulation of the dislocation charge	66
4.2	Inversion- and rotation-symmetric insulators.	70
4.3	Honeycomb lattice	74
4.4	Time-reversal symmetry	76
4.5	Spinful honeycomb lattice	77
4.6	Conclusion	78
	Appendices	79
C		79
C.1	Useful identities	79
C.2	Derivation of Eq. (4.7)	81
C.3	Relation $W_{\mu_1-\mu_3}^{1/2}(\mathcal{S}_{C_{3,A}})$ and $\det(\mathcal{S}_{\tilde{C}_{3,A}}(K^+))$	86
C.4	Derivation of Eq. (4.10)	87
5	Dirac cones beyond the honeycomb lattice: a symmetry-based approach	89
5.1	Band crossing points	91
5.2	2D lattices with cones along high-symmetry lines	93
5.2.1	Square lattice	94
5.2.2	Rectangular lattice	96
5.2.3	Triangular lattice	97
5.2.4	Centered rectangular lattice	100
5.3	Away from high-symmetry lines	100
5.3.1	P6	101
5.3.2	P4	102
5.3.3	P2	102
5.3.4	P6mm	103
5.3.5	P4mm and P4mg	103
5.3.6	P2mm, P2mg, and C2mm	105
5.4	Conclusions and discussion	105

6	Band structure engineering on Cu(111)	109
6.1	Experimental results	112
6.2	Numerical results	116
6.3	Conclusion	120
7	Conclusion and Outlook	121
7.1	Summary of the results	121
7.2	Outlook	123
8	Samenvatting	125
8.1	De symmetrie en topologie van een kristal	125
8.2	Ladingsophoping en topologie	127
8.3	Dirac kegels	128
8.4	En hoe nu verder?	130
	List of Publications	131
	Bibliography	133
	CV	141

Preface

“Overaftelbaar oneindig.”

– N.N.

This thesis is the result of four years of research, done at the Institute for Theoretical Physics under supervision of Prof. dr. Cristiane Morais Smith and Dr. C. Ortix.

Chapter 1 gives an introduction to, and outline of, the main part of the thesis. The results of our research are described in Chapters 2-6. At the end of the thesis, the reader will find a list of our publications, the bibliography, a Dutch summary, and a resume of the author.

I wish the reader much joy and inspiration while reading my thesis.

Guido van Miert
April 2018, Utrecht

1 Introduction

Most of us are familiar with symmetry. In particular, we easily tell symmetric and asymmetric things apart. For example, we see that Fig. 8.1 (a) stays the same under reflection, whereas Fig. 8.1 (b) does not. For this reason we call Fig. 8.1(a) reflection-symmetric. The most symmetric picture we can imagine is an infinite blank page. It is invariant under arbitrary rotations, translations, and reflections. We do not want to judge your taste, but we suspect that most people find this rather dull. Periodic tilings provide a nice middle ground, since they are invariant under discrete translations, but on smaller scales they may be completely asymmetric, see Fig. 1.2 for some examples. In fact, mathematicians have systematically classified all possible patterns based on their symmetry. For example, they have shown that it is only possible to construct a periodic tiling with a two-, three-, four-, or six-fold rotational symmetry. In fact, if you would like to decorate a palace like the Alhambra in Granada, then you may choose from just 17 distinct patterns. At the one extreme end you find the plain white tile, see Fig. 1.2(a), whereas at the other end, we find a tile which gives rise to a pattern that only has discrete translation symmetry in the horizontal and vertical directions, see Fig. 1.2(d). We leave it as an exercise to the reader to spot the differences.

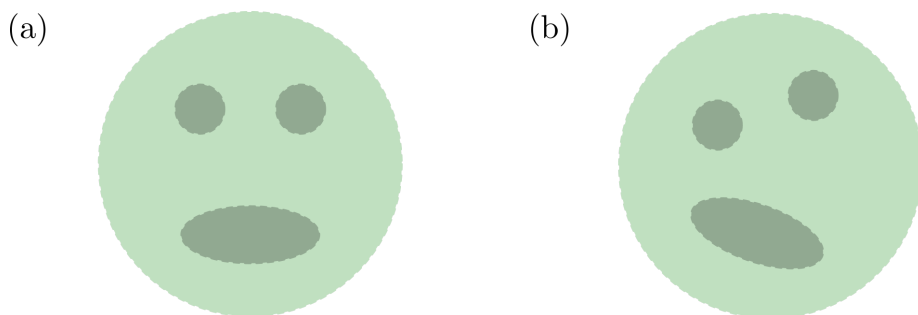


Figure 1.1: (a) Symmetric (b) asymmetric.

1 Introduction

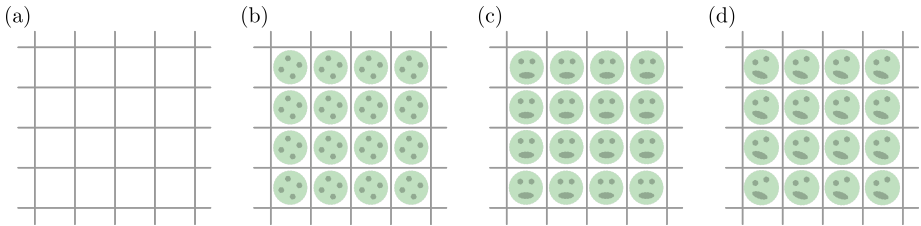


Figure 1.2: Four distinct patterns.

Suppose you have finally found your favorite pattern, then you might go one step further. In particular, one might ask if two tilings with the same symmetry are different from a topological point of view. Topology studies the properties of objects that are left invariant under smooth deformations. For example we may wonder whether it is possible to deform two mirror-symmetric patterns into each-other. It turns out that one can easily change two mirror-symmetric patterns into each-other, see for example Fig. 1.3 (a). Hence, we cannot distinguish two patterns from a topological point of view. In order to further distinguish periodic patterns, we have to add more structure. One way of achieving this, is requiring that the tiles are decorated with objects that are not allowed to vanish, or fade away. For concreteness let us imagine that the tiles are decorated with indestructible green triangles. It turns out that even then we can deform the two patterns, see Fig. 1.3 (b). There is a subtlety involved, namely, during the deformation we had to break the reflection symmetry. Now suppose that we rule out these symmetry-breaking deformations. Then one can say that the two periodic tilings are topologically distinct. Hence, we have seen that one can tell different patterns apart based on their symmetry, or absence thereof. But in the presence of some additional structure one can do more, one can tell patterns with the same symmetry apart based on their topology.

This thesis is not about the symmetry and topology of periodic tilings. Instead, we study electrons that move around in crystals. But, the two subjects do exhibit some similarities. For one, we also tell different crystals apart based on their symmetry. Moreover, (crystalline) insulators, like decorated tiles, can be topologically distinct. To study the electrons in crystals, it will prove useful to know what a band structure is. In a typical introductory course on quantum mechanics, we are taught about free electrons and

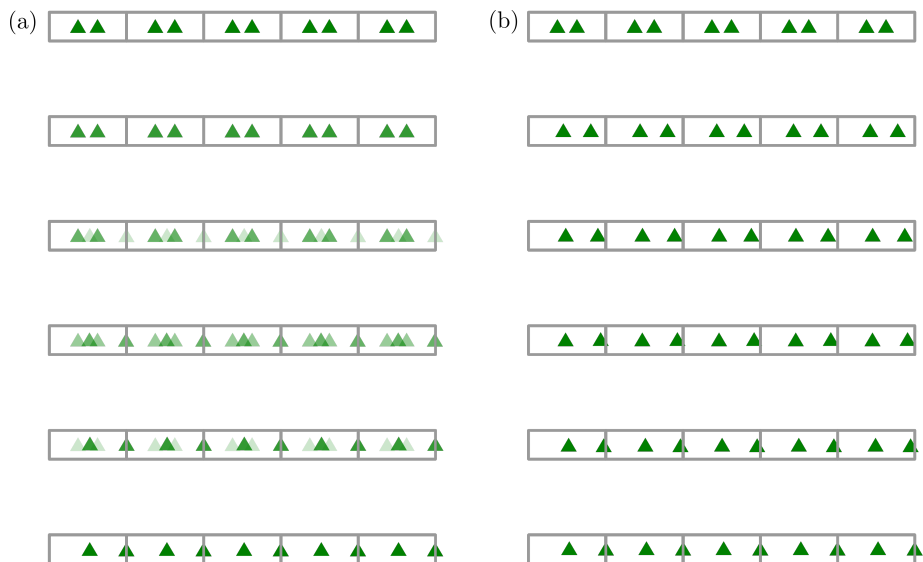


Figure 1.3: Two ways of deforming two mirror-symmetric patterns into each other. In both cases we start at the top with two triangles mirror-symmetrically positioned with respect to the center of the unit-cell, and at the bottom we find a single triangle in the center of the unit cell, and another one at the boundary of the unit cell. In (a) we deform the two patterns into each other by fading. This means that we have simply superimposed the bottom and top image and gradually change the weight of the top image from 1 to 0, and the the weight of the bottom image from 0 to 1. In (b) we explicitly break the mirror-symmetry during the deformation.

1 Introduction

a particle in a box. In the former case, we find that the wave-functions are plane waves, which we label with a wave-vector $q \in \mathbb{R}$, whereas in the latter case the energies and eigenstates are labeled by a discrete index $j \in \mathbb{N}_{>0}$. In a crystal the situation is a hybrid between the two. Indeed, Bloch's theorem guarantees that we can label the eigenstates by a discrete index j , that we call a band index, and a quasi-wave vector $q \in [-\pi/a, \pi/a)$. In fact this theorem states that the wave functions, or Bloch waves as one calls them, are modulated plane waves, i.e.

$$\Psi_{j,q}(r) = e^{iqx} u_{j,q}(x),$$

with $u_{j,q}(x) = u_{j,q}(x + a)$, where a denotes the lattice constant. In Fig. 1.4 we plot the energies of the Bloch waves as a function of q ; such a figure is known as a band structure, and a single curve is referred to as a band. Compared to a free electron, we find that there are certain ranges of energy that are forbidden, a band gap separates different energy bands, whereas compared to a particle in a box the density of states is not simply a collection of sharp peaks, but spread out in energy. The presence of a band gap is ultimately the reason why most insulators are insulating (exceptions include interaction-driven insulators, like Mott insulators). Namely, the Pauli exclusion principle dictates that the zero-temperature ground state is given by the Slater determinant of all single particle eigenstates with energies lower than the Fermi level E_F . Now suppose that this Fermi level lies in the band gap; then the system does not host low-lying excitations: you have to pay a finite amount of energy to create an electron-hole pair.

To make matters a bit more concrete, let us introduce a toy-model. Here, we consider the so-called Rice-Mele model [1], which describes a bi-partite lattice, see Fig. 1.5 (a). The electrons can hop between neighboring sites with hopping amplitudes t_1 and t_2 and in addition they experience a staggered on-site potential $\pm m$. The corresponding Hamiltonian is given by

$$\hat{H} = - \sum_i \left(t_1 a_i^\dagger b_i + t_2 a_i^\dagger b_{i-1} + h.c. \right) + \sum_i m \left(a_i^\dagger a_i - b_i^\dagger b_i \right),$$

where a_i^\dagger (b_i^\dagger) creates an electron in the i th unit cell on the A (B) sublattice. Such a Hamiltonian is a tight-binding model, which means that we have projected the full Hamiltonian onto a finite set of localized orbitals per unit-cell. To obtain the band structure, we apply a Fourier transformation. If we

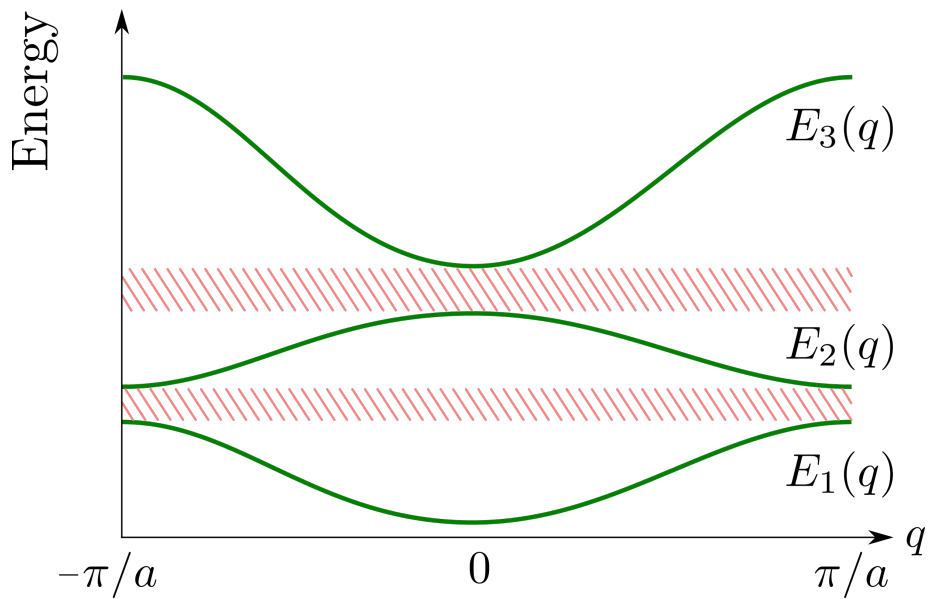


Figure 1.4: A sketch of a band structure. The different bands are the green curves, and the forbidden ranges of energy are depicted by the red dashed regions.

1 Introduction

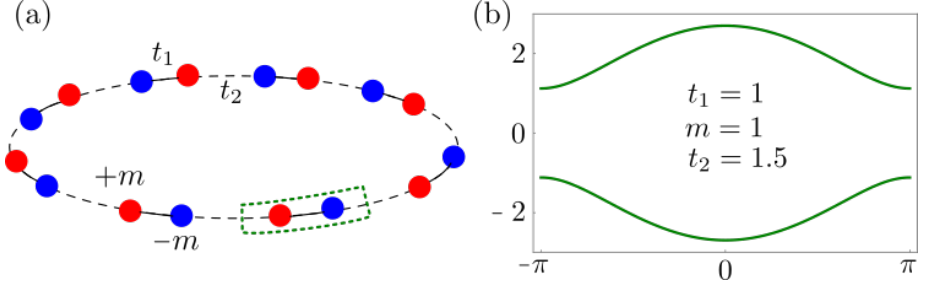


Figure 1.5: (a) Pictorial representation of the Rice-Mele model. The A (B) sublattice is shown in red (blue). (b) Corresponding band structure.

put the lattice constant a to 1, we can write

$$\hat{H} = - \sum_q (a_q^\dagger, b_q^\dagger) \tilde{H}(q) (a_q, b_q)^T,$$

with $\tilde{H}(q)$ a 2×2 matrix given by

$$\tilde{H}(q) = \begin{pmatrix} m & t_1 + t_2 e^{-iq} \\ t_1 + t_2 e^{iq} & -m \end{pmatrix}.$$

The eigenvalues of $\tilde{H}(q)$ then yield the band structure. In this case, these are given by $\pm \sqrt{m^2 + t_1^2 + t_2^2 + 2t_1 t_2 \cos(q)}$, see also Fig. 1.5(b) for a specific example.

Now suppose we are given two insulators: then, one may ask whether they are topologically equivalent. By this we mean that we ask whether we can deform the two insulators into each other without closing the band gap. It turns out that, in general, all one-dimensional insulators are topologically identical. However, if we impose additional symmetries this is no longer true. For example we may consider chiral symmetry. Technically, this means that there exists a unitary matrix \tilde{U} , which anti-commutes with $\tilde{H}(q)$. In the Rice-Mele model we can implement this symmetry by setting $m = 0$. In that case, we find that the unitary operator $\tilde{U} = \sigma_z$ anti-commutes with $\tilde{H}(q)$. More importantly, this symmetry ensures that $\tilde{H}(q)$ is an off-diagonal Hermitian matrix. This allows us to assign a topological invariant to the Hamiltonian that can only change if the band gap closes. Indeed, we can simply track the winding of the off-diagonal term, given by $t_1 + t_2 e^{iq}$, in the

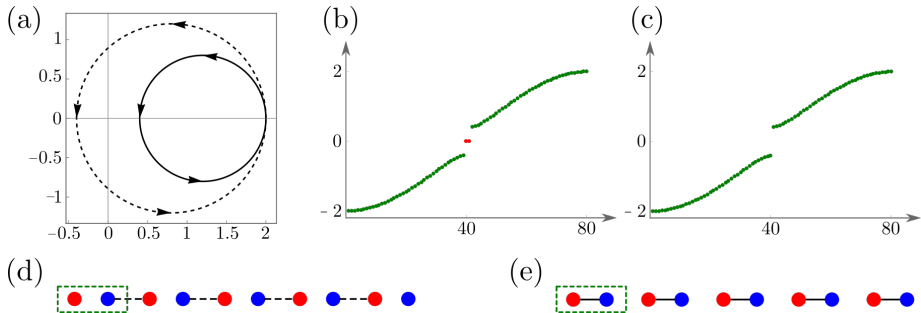


Figure 1.6: (a) Winding of the off-diagonal term in the complex plane. The dashed (solid) contour corresponds to the case $t_1 = 0.8$ (1.2) and $t_2 = 1.2$ (0.8). (b) and (c) spectra for the corresponding chains with open boundary conditions. (d) Open chain with $N = 5$ unit cells, $t_1 = 0$, and $t_2 = 1$. (e) Open chain with $N = 5$ unit cells, $t_1 = 1$, and $t_2 = 0$.

complex plane as q changes from $-\pi$ to π . In Fig. 1.6 (a) we have plotted two of these contours. We find that the dashed curve encircles the origin precisely once, whereas the solid curve does not. From this, we immediately infer that there is a topological obstruction to deform the corresponding toy-models into each other without closing the gap. Indeed, if the winding number changes the contour has to cross the origin of the complex plane. But this means that the Hamiltonian is gapless. Hence, like decorated tiles, we also find that 1D systems with a chiral symmetry can be topologically distinct.

Visual inspection reveals whether two patterns of decorated tiles are topologically distinct. Unfortunately, this does not apply to insulators. In fact, one can probe the topology by looking at what happens at the edge of your system. This is known as the bulk-edge correspondence, which plays a central role in the field of topological insulators. To illustrate this point, we have plotted the spectra for two models with winding number (W) 1 and 0 and open boundary conditions in Figs. 1.6 (b) and (c). The spectra look almost identical, in fact their bulk band structures are identical. However, the chain with winding number 1 exhibits two in-gap states at zero energy, whereas the other chain does not. Of course one should not confuse correlation with causation, but at least one is tempted to hypothesize that if the winding number is 1 (0), then the system with edges will (not) host a

1 Introduction

pair of in-gap states at zero energy. One can show this by noting that if $W = 1$, then one may deform the chain to the case $t_1 = 0$ and $t_2 = 1$. The corresponding open chain is displayed in Fig. 1.6(d). We count $N - 1$ dimers and two uncoupled sites, one to the left and one to the right. The latter correspond to the two zero-energy edge states. The crux is that, if we now change the hopping parameters, then the chiral symmetry ensures that these two states are pinned at zero energy. Similarly, the chain with $W = 0$ can be deformed to the case $t_1 = 1$ and $t_2 = 0$. In that case the open chain, shown in Fig. 1.6(e), does not feature any uncoupled sites, but simply contains N dimers. Therefore, there are no zero-energy states. Hence, chiral-symmetric systems can exhibit different topologies, and these can be probed by counting the number of in-gap states pinned at zero energy.

Nature provides us many symmetries, and therefore there are many questions that one can ask. This thesis primarily studies inversion, rotation, and mirror symmetries. The goal is to understand how the corresponding topologies can be probed around edges, but also around other defects, like dislocations. Furthermore, we investigate how these symmetries can stabilize degeneracies in the band structure. The outline of the thesis is presented below.

1.1 Outline

In Chapter 2 we consider the topology of two-dimensional inversion-symmetric insulators and semi-metals. In particular, we show that these systems allow for a \mathbb{Z}_2 -classification based on the Zak phase. However, in this case there is no chiral symmetry that pins any edge states to zero energy. Hence, it is unclear what the precise relationship is between the Zak phase and the presence of edge states. Then, in Chapter 3, we will study this issue in greater detail. In particular, we resolve the origin and unit-cell ambiguity present in the Zak phase. In addition, we show that even for spinful systems one can define and probe a \mathbb{Z}_2 -invariant. In Chapter 4 we extend these results to two-dimensional insulators. In particular, we show that edge dislocations provide an ideal setting to measure crystalline topologies. Then, in Chapter 5, we provide a symmetry analysis of two-dimensional Dirac materials. These are systems with a degeneracy/node in the band structure that is topologically protected. Finally, in Chapter 6, we discuss a bottom-up

1.1 Outline

approach to engineer novel electronic lattices.

2 Topological origin of edge states in 2D inversion-symmetric insulators and semi-metals

The characterization of topological states of matter is a central topic in condensed-matter physics [2, 3]. A beautiful example is given by the Altland-Zirnbauer (AZ) table [4], which classifies topological insulators and superconductors depending on their dimensions and discrete symmetries [5–7]. A 2D Chern insulator, for example, is characterized by a \mathbb{Z} invariant and relies on the absence of time-reversal (\mathcal{T}) symmetry [8]. The presence of this symmetry is instead crucial for \mathbb{Z}_2 topological insulators that exhibit the quantum spin Hall effect [9]. In these topologically non-trivial insulators, there is a one-to-one correspondence between the topological invariant and the number of gapless modes localized at the edge, known as the bulk-boundary correspondence [10]. In Chern insulators the edge states are chiral, which means that they all propagate in the same direction, whereas topological time-reversal invariant insulators exhibit helical edge states, with electrons of opposite spins counterpropagating at the sample boundaries.

There are, however, insulators and semimetals, which are topologically trivial according to the AZ-table, although they generally do exhibit edge states. A natural question is then whether these “*trivial*” edge states are related to a topological invariant that exists in the presence of a discrete or continuous symmetry. For 2D chiral systems, for instance, the existence of zero-energy edge states can be inferred from a 1D winding number [11, 12]. This explains the origin of trivial edge states in a minimal tight-binding model for graphene. More recently, this symmetry has been used to predict edge states in single-layer black phosphorus (sometimes also called phosphorene) [13]. However, this explanation is quite unsatisfactory for insulators and semimetals because we do not expect the presence of a chiral symmetry: both in graphene and black phosphorus, the next-nearest neighbor hopping breaks the chiral symmetry.

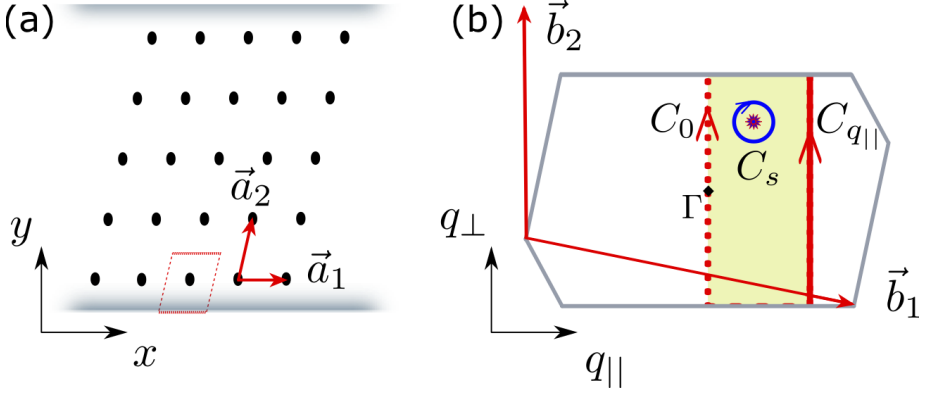


Figure 2.1: (a) Oblique lattice with lattice vectors \vec{a}_1 and \vec{a}_2 . The red dashed rhomboid shows the unit-cell. (b) The corresponding 2D Brillouin zone, with the reciprocal lattice vectors \vec{b}_1 and \vec{b}_2 . The red dashed line corresponds to the contour C_0 , whereas the solid line corresponds to $C_{q_{||}}$, the blue circle denotes the contour C_s , and the enclosed area S is shown in yellow.

Here, we reveal the importance of inversion (\mathcal{I})-symmetry, which has been overlooked in previous studies. We demonstrate that the existence of edge states in 2D crystalline insulators without spin-orbit coupling (SOC) in the presence of \mathcal{T} and \mathcal{I} symmetry is related to a 1D \mathbb{Z}_2 invariant. We then apply this result to a generic toy model, and elucidate the relation between the edge states and this topological invariant. Moreover, we discuss the quantization of the surface charge in the absence of edge states. Finally, we apply our results to single and bilayer black phosphorus.

2.1 Symmetry of the Bloch Hamiltonian

Let us consider a 2D crystalline insulator, described by a Bloch Hamiltonian $\tilde{H}(\vec{q})$. We assume negligible SOC, such that we can model the system using spin-less fermions. In the presence of \mathcal{I} and \mathcal{T} symmetry, the Hamiltonian satisfies the following constraints:

$$\tilde{H}(\vec{q}) = \tilde{I}\tilde{H}(-\vec{q})\tilde{I}, \quad \tilde{H}(\vec{q}) = \tilde{H}(-\vec{q})^*, \quad (2.1)$$

where \tilde{I} is the inversion operator and $*$ denotes complex conjugation. Note that in the absence of SOC, there is no distinction between inversion and

two-fold rotation (C_2) symmetry. Therefore, our results also apply to C_2 -symmetric systems. Moreover, we consider a system with an inversion-symmetric unit-cell, which means that the inversion operator is momentum independent. Since we are interested in the existence of edge states, we put the system on a cylinder, as in Fig. 2.1(a), and limit ourselves to crystalline edges, characterized by one of the lattice vectors $\vec{a}_1 = (a_1, 0)$. We will assign a topological invariant to the projected Bloch Hamiltonian $\tilde{H}_{q_{\parallel}}(q_{\perp}) = \tilde{H}(q_{\parallel}, q_{\perp})$, where $q_{\parallel}(q_{\perp})$ denotes the momentum along (perpendicular to) the edge. To discuss the consequences of the constraints in Eq. (2.1), we first briefly revisit the topology of band insulators in 1D.

2.2 Band topology in 1D

According to the AZ-table, insulators in 1D, belonging to classes A, AI, and AII, are trivial. Despite this fact, band topology does play an important role for these crystalline insulators. In particular, the surface charge at the end of such an insulator is directly related to the Zak phase[14, 15]

$$\gamma_{\text{Zak}} = \int_{-\pi/a}^{\pi/a} dq A(q), \quad (2.2)$$

where a is the lattice constant and $A(q) = \sum_{i \in \text{occ}} \langle u_{q,i} | i \nabla_q | u_{q,i} \rangle$ denotes the Zak connection, with $|u_{q,i}\rangle$ the periodic part of the Bloch wave function with band index i , momentum q , and “occ” denotes the set of occupied bands. Generically, the Zak phase is not quantized. However, in the presence of 1D \mathcal{I} -symmetry, one finds $\gamma_{\text{Zak}} = -\gamma_{\text{Zak}} \bmod 2\pi$ (see Appendix A.1). Hence,

\mathcal{I}	\mathcal{T}	\mathcal{IT}	1D
✓	✓	✓	\mathbb{Z}_2
✓	×	×	\mathbb{Z}_2
×	✓	×	0
×	×	✓	\mathbb{Z}_2
×	×	×	0

Table 2.1: Classification of 1D insulators in the presence or absence of \mathcal{I} , \mathcal{T} , and \mathcal{IT} symmetry, based on the Zak phase. Here, we consider spinless fermions.

2 Topological origin of edge states in inversion-symmetric insulators and semi-metals

either $\gamma_{\text{Zak}} = 0$ or $\gamma_{\text{Zak}} = \pi$, and as such it defines a \mathbb{Z}_2 invariant [16]. Moreover, we do not need to compute the integral in Eq. (2.2); instead, we can write

$$e^{i\gamma_{\text{Zak}}} = \prod_{i \in \text{occ}} \xi_i(0)\xi_i(\pi/a) \in \mathbb{Z}_2, \quad (2.3)$$

where $\xi_i(q_{\text{inv}}) = \langle \Psi_{q_{\text{inv}},i} | \tilde{I} | \Psi_{q_{\text{inv}},i} \rangle$ is the parity of the full Bloch wave function $|\Psi_{q_{\text{inv}},i}\rangle$ at the \mathcal{I} invariant momenta q_{inv} . By considering \mathcal{T} -symmetry, one can construct five different classes. In 1D, three of these allow for a \mathbb{Z}_2 classification, based on the Zak phase, see Table 2.1 and Appendix A.1. Next, we employ this invariant to characterize a 2D system.

2.3 \mathbb{Z}_2 classification

Let us now return to the set of 1D Hamiltonians $H_{q_{\parallel}}(q_{\perp})$ parameterized by q_{\parallel} . Note that for $q_{\parallel} = 0$, the symmetry constraints given in Eq. (1) are inherited. In particular, the 2D \mathcal{I} symmetry yields $H_0(q_{\perp}) = \tilde{I}H_0(-q_{\perp})\tilde{I}$. Therefore, the associated Zak phase $\gamma_{\text{Zak}}(0)$ is quantized, and defines a \mathbb{Z}_2 invariant [16],

$$\chi_1 = e^{i\gamma_{\text{Zak}}(0)} = \prod_{i \in \text{occ}} \xi_i(0)\xi_i(\vec{b}_2/2). \quad (2.4)$$

Here, \vec{b}_2 is the reciprocal-lattice vector pointing in the direction perpendicular to the edge, see Fig. 2.1(b), and the subscript in χ_1 reminds us of the fact that this invariant is associated with an edge parallel to \vec{a}_1 . If the edge would be along \vec{a}_2 , then we should simply consider the invariant $\chi_2 = \prod_{i \in \text{occ}} \xi_i(0)\xi_i(\vec{b}_1/2)$. The definition of the invariant in Eq. (2.4) is, strictly speaking, only valid for $q_{\parallel} = 0$. However, we can express the difference in the Zak phases $\gamma_{\text{Zak}}(q_{\parallel}) - \gamma_{\text{Zak}}(0)$ as an integral of the Zak connection \vec{A} along the contour $C_{q_{\parallel}} - C_0$, see Fig. 2.1(b). Using Stokes' theorem, this can be rewritten as a surface integral of the Zak curvature $F(q_{\parallel}, q_{\perp}) = \partial_{q_{\parallel}}A_{\perp} - \partial_{q_{\perp}}A_{\parallel}$, see Fig. 2.1(b). Since the two symmetry constraints in Eq. (2.1) ensure that $F = 0$ (see Appendix A.2), we find $\gamma_{\text{Zak}}(q_{\parallel}) = \gamma_{\text{Zak}}(0)$. It follows that even in the absence of chiral symmetry, we can still associate a \mathbb{Z}_2 invariant with each of the 1D Hamiltonians $H_{q_{\parallel}}$.

2.4 Bulk-Boundary Correspondence

So far, we have implicitly assumed that $H_{q_{||}}$ and H_0 are adiabatically connected, such that F is actually well defined within the yellow area in Fig. 2.1(b). Therefore, our proof does not apply to systems with band-crossing points, like semimetals. In the latter case, we can modify our proof, by assuming that the band-crossing point is located inside the contour C_s , as indicated in Fig. 2.1(b). Then, we can apply Stokes' theorem to the new contour $C_{q_{||}} - C_0 - C_s$, which yields

$$\gamma_{\text{Zak}}(q_{||}) - \gamma_{\text{Zak}}(0) = \oint_{C_s} d\vec{q} \cdot \vec{A}(q_x, q_y) = j\pi, \quad (2.5)$$

where j is an integer. This result follows from the quantization of the Zak phase $\gamma_{\text{Zak},s} = \oint_{C_s} d\vec{q} \cdot \vec{A}(q_x, q_y)$ associated with the band crossing in multiples of π (see Appendix A.2). Thus, for a semimetal, the Zak phase $\gamma_{\text{Zak}}(q_{||})$ is quantized, but changes by $j\pi$ as one encloses a $j\pi$ -Zak phase degeneracy. Henceforth, for both 2D insulators and semimetals, we can introduce a topological \mathbb{Z}_2 invariant χ_1 protected by \mathcal{I} and \mathcal{T} symmetry, which reflects the fact that the Zak phase $\gamma_{\text{Zak}}(q_{||})$ is quantized for all values of $q_{||}$.

2.4 Bulk-Boundary Correspondence

Next, we discuss the bulk-boundary correspondence, which relates the \mathbb{Z}_2 invariant χ_1 to the edge behavior. For this purpose, we consider a two-band toy model on an oblique lattice. Specifically, we study a system with edges as in Fig. 2.1(a), for which every site hosts an s and a p orbital. The corresponding bulk Hamiltonian can be written as $\tilde{H}(\vec{q}) = h_I(\vec{q})\mathbb{1} + h_y(\vec{q})\sigma_y + h_z(\vec{q})\sigma_z$, where h_I , h_y , and h_z are real-valued even functions due to the constraints in Eq. (2.1), and σ_i are the Pauli matrices. Moreover, in this basis the inversion operator is given by $\tilde{I} = \sigma_z$, such that $\tilde{I}|s\rangle = |s\rangle$ and $\tilde{I}|p\rangle = -|p\rangle$. At half-filling, we have $\xi(\vec{q}_{\text{inv}}) = \text{sgn}[h_z(\vec{q}_{\text{inv}})]$. Hence, we can express the \mathbb{Z}_2 invariant as

$$\chi_1 = \text{sgn}[h_z(0)]\text{sgn}[h_z(\vec{b}_2/2)]. \quad (2.6)$$

2 Topological origin of edge states in inversion-symmetric insulators and semi-metals

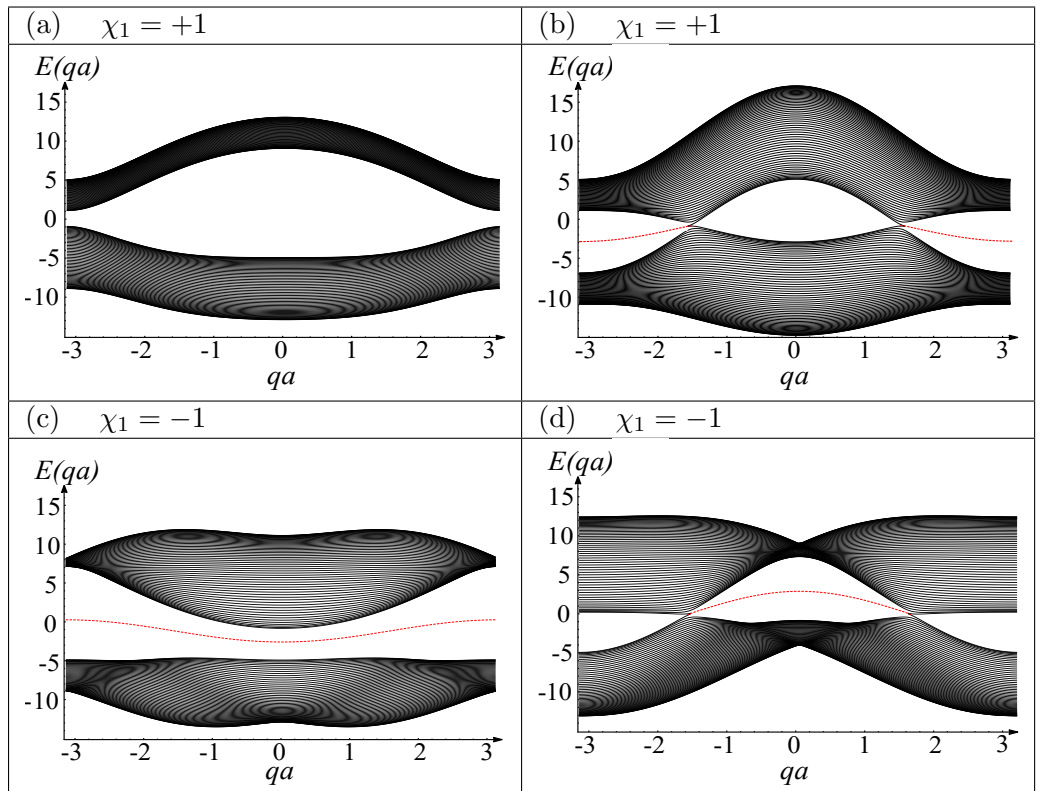


Table 2.2: Four different band structures for a two-band model, with both \mathcal{I} and \mathcal{T} symmetry. Bulk (edge) states are indicated by solid (dashed) black (red) lines. (a) Spectrum of an insulator with a trivial \mathbb{Z}_2 invariant; (b) Dirac semimetal with a trivial \mathbb{Z}_2 invariant; (c) Again an insulator, but now with a non-trivial \mathbb{Z}_2 invariant; (d) Dirac semimetal with a non-trivial \mathbb{Z}_2 invariant. The parameters used for these four dispersion relations are given in Appendix A.3.

2.4 Bulk-Boundary Correspondence

If one only includes nearest-neighbor hopping, the bulk Hamiltonian is specified by

$$\begin{aligned} h_I + h_z &= e_s + 2t_{s,1} \cos(\vec{q} \cdot \vec{a}_1) + 2t_{s,2} \cos(\vec{q} \cdot \vec{a}_2), \\ h_I - h_z &= e_p + 2t_{p,1} \cos(\vec{q} \cdot \vec{a}_1) + 2t_{p,2} \cos(\vec{q} \cdot \vec{a}_2), \\ h_y &= 2t_{sp,1} \sin(\vec{q} \cdot \vec{a}_1) + 2t_{sp,2} \sin(\vec{q} \cdot \vec{a}_2), \end{aligned}$$

where e_s and e_p denote the on-site energies, $t_{s,i}$ and $t_{p,i}$ are the nearest-neighbor-hopping parameters in the direction i , and $t_{sp,i}$ is the hybridization among s and p orbitals. In Table 2.2, we display four spectra, which are realized for values of the above parameters chosen *ad hoc*, in a way to provide an example of the four qualitatively different scenarios (see Appendix A.3). We will shortly discuss below how their distinct features can be understood in terms of the \mathbb{Z}_2 invariant.

(i) *Gapped bulk with a trivial \mathbb{Z}_2 invariant:*

For $\chi_1 = +1$, and in the absence of band-crossing points, the Zak phase $\gamma_{\text{Zak}}(q_{\parallel}) = 0$ for all q_{\parallel} . In this case, the trivial value of the Zak phase for all values of the momentum is reflected in the absence of edge states. This behavior is confirmed by plotting the spectrum for an insulator with $\chi_1 = +1$ in Table 2.2(a), which only shows bulk states.

(ii) *Gapless bulk with a trivial \mathbb{Z}_2 invariant:*

The combination of a trivial \mathbb{Z}_2 invariant, $\chi_1 = +1$, and two π -Zak phase band-crossing points yields a trivial Zak phase $\gamma_{\text{Zak}}(q_{\parallel}) = 0$ for momenta adiabatically connected to 0, and a non-trivial Zak phase $\gamma_{\text{Zak}}(q_{\parallel}) = \pi$ for q_{\parallel} outside this region. Hence, for momenta contained in the latter region, the bulk topology gives rise to edge states. This is indeed the case for the spectrum shown in Table 2.2(b), which corresponds to a Dirac semimetal with $\chi_1 = +1$.

(iii) *Gapped bulk with a non-trivial \mathbb{Z}_2 invariant:*

For a non-trivial insulator, with $\chi_1 = -1$, the Zak phase $\gamma_{\text{Zak}}(q_{\parallel}) = \pi$ for all q_{\parallel} . The non-trivial Zak phase manifests itself via the presence of edge states for all momenta. This is verified in the example shown in Table 2.2(c) (where $\chi_1 = -1$), which features in-gap edge states for all momenta.

(iv) *Gapless bulk with a non-trivial \mathbb{Z}_2 invariant:*

Finally, we consider a gapless system with a non-trivial invariant, $\chi_1 = -1$. Then, the Zak phase $\gamma_{\text{Zak}}(q_{\parallel}) = \pi$ for the values of q_{\parallel} that are adiabatically connected to $q_{\parallel} = 0$, whereas for q_{\parallel} outside this region $\gamma_{\text{Zak}}(q_{\parallel}) = 0$.

Hence, we expect the presence of edge states for q_{\parallel} that are adiabatically connected to $q_{\parallel} = 0$. The band structure shown in Table 2.2(d) confirms this expectation.

Thus, for insulators the \mathbb{Z}_2 invariant determines the presence or absence of edge states, whereas for a Dirac semimetal it encodes whether the two Dirac cones are connected by edge states which go through zero or π . In particular, we might view Dirac semimetals as systems that interpolate between different \mathbb{Z}_2 insulators. Moreover, our results show that edge states are a generic feature of Dirac semi-metals.

2.5 Surface Charge Quantization

We now explain the deep connection between the \mathbb{Z}_2 invariant χ_1 and the emergence of in-gap states. It is a direct consequence of the boundary-charge theorem [14], which states that for a one-dimensional crystalline spin-degenerate insulator the surface charge σ is well defined modulo $2e$, and is given by

$$\sigma = \pm \left(-\frac{e\gamma_{\text{Zak}}}{\pi} + e \sum_{j=1}^{\mathcal{N}} Z_j u_j + e \sum_{j \in \text{surf}} Z_j \right). \quad (2.7)$$

Here, e is the electron charge, γ_{Zak} is the Zak phase, \mathcal{N} is the total number of atoms within a unit cell, and Z_j and u_j denote, respectively, the atomic number and position of the j th atom within the unit cell. The second term vanishes for \mathcal{I} -symmetric insulators. Moreover, the third term counts the total ionic charge of the atoms contained in the set ‘‘surf’’. These are the atoms that remain at the edges when tiling the finite system with unit cells. Note that this term precisely cancels the unit-cell ambiguity stemming from the first two terms. The \pm refers to the left and right surface charge. In the presence of \mathcal{I} -symmetry, σ is quantized to 0 or e modulo integer multiples of $2e$. In principle, this $2e$ ambiguity allows for different right- and left-surface charges; however, when the open chain is \mathcal{I} -symmetric, we find that $\sigma_{\text{left}} = \sigma_{\text{right}}$. Hence, the net charge present on the open chain is then $Q_{\text{net}} = \sigma_{\text{right}} + \sigma_{\text{left}} = 2\sigma_{\text{right}}$ modulo $4e$. The relation between the net charge and in-gap states can be brought to light using the following adiabatic

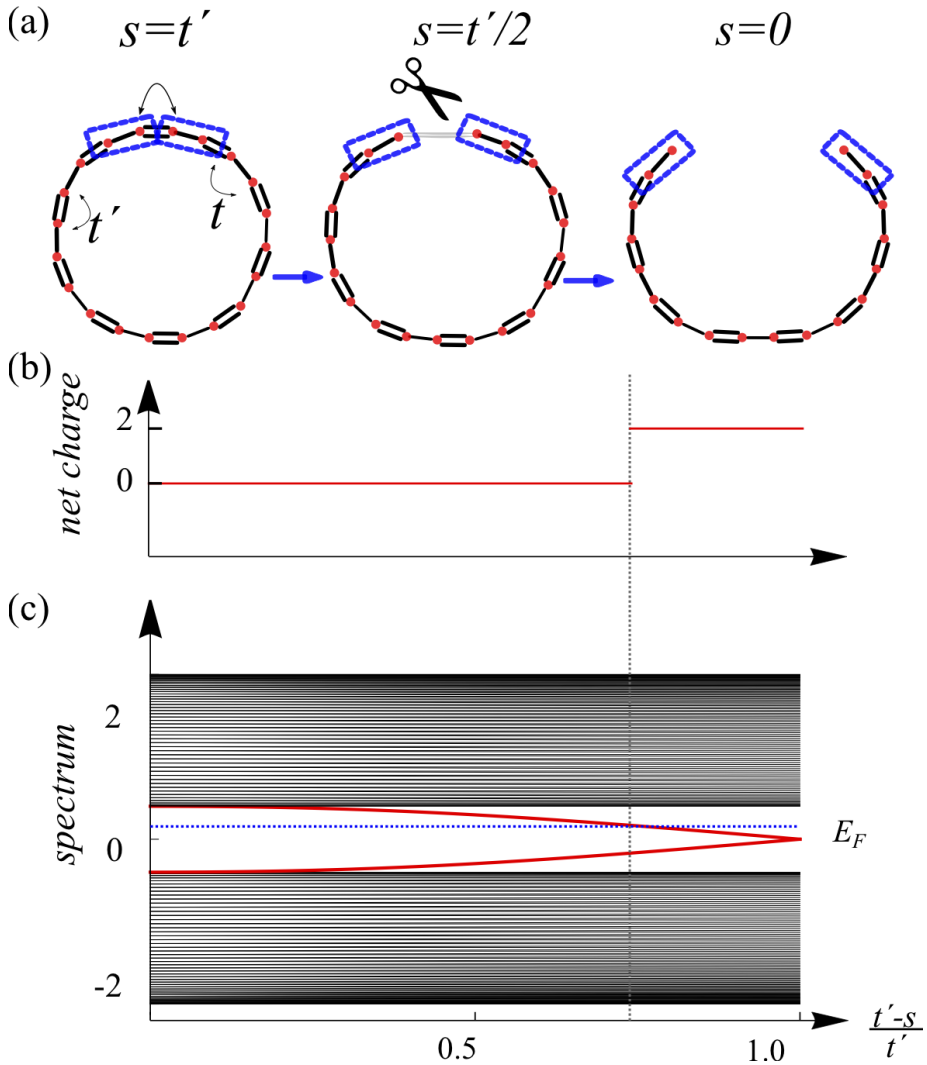


Figure 2.2: (a) Sketch of a periodic Su-Schrieffer-Heeger chain, which is adiabatically deformed into a chain with open ends. The parameter s is the hopping parameter that connects the two blue unit-cells. (b) Net charge present on the chain as a function of the hopping parameter s , which is adiabatically turned off. (c) Corresponding spectrum. Here, we have considered a chain containing 100 unit cells.

continuity argument, which we illustrate for a Su-Schrieffer-Heeger chain that we put in a ring geometry, as depicted in Fig. 2.2(a). Electrons on the chain can hop with hopping parameters t and t' , corresponding to the single and double bonds. For simplicity, we set $t = -0.8\text{eV}$ and $t' = -1.2\text{eV}$. In addition, we consider a weak link with hopping parameter s , that can be varied. The presence of the weak link defines a preferential unit cell, which contains a single bond in our example. The Zak phase is then $\gamma_{\text{Zak}} = \pi$. From the boundary-charge theorem, it follows that, for an open chain ($s = 0$), both ends of the chain will have a surface charge $\sigma = e$. Therefore, the net charge will be $2e$ modulo $4e$. This implies, that if one adiabatically changes the weak-link hopping parameter from $s = t'$ to $s = 0$, an odd number of spin-degenerate states crosses the Fermi level: an in-gap state must have appeared, see Figs. 2.2(b) and (c). This does not guarantee that in-gap states will be present at the end of the adiabatic deformation ($s = 0$). In-gap states can dissolve into the bulk, whereas they are pinned at zero energy in systems with particle-hole symmetry.

To demonstrate this statement, we consider the band structure shown in Fig. 2.3(a). The corresponding bulk Hamiltonian is still described by the two-band toy model, with $\chi_1 = -1$ (see Appendix A.4 for the details). The in-gap edge states are absent for $q_{\parallel} = 0$, while for sufficiently large values of q_{\parallel} , they emerge from the bulk. Hence, the in-gap state that must have traversed the band gap leaves no clear trace in the spectrum at $q_{\parallel} = 0$. Despite the trivial spectrum at $q_{\parallel} = 0$, we find that the non-trivial topology is captured by the net charge distribution $\rho(i)$, as shown in Fig. 2.3(b), thereby verifying the validity of the boundary-charge theorem, Eq. (2.7). In particular, it follows that for 2D insulators in the presence of \mathcal{I} - and \mathcal{T} -symmetry, the surface charge associated with $H_{q_{\parallel}}$ is either 0 or e , as numerically confirmed in Fig. 2.3(b).

To verify the absence of bound states at $q_{\parallel} = 0$, we have analyzed the inverse participation ratio (IPR), which quantifies over how many sites a particular state is distributed [17]. For a given state $|\Psi\rangle$ in a 1D system, the IPR is defined as

$$IPR(|\Psi\rangle) = \sum_{i,\alpha} |\langle i, \alpha | \Psi \rangle|^4, \quad (2.8)$$

where $|i, \alpha\rangle$ denotes the state localized at site i , and α labels the orbital. For a proper bulk state, the IPR as a function of the chain length N should be

2.5 Surface Charge Quantization

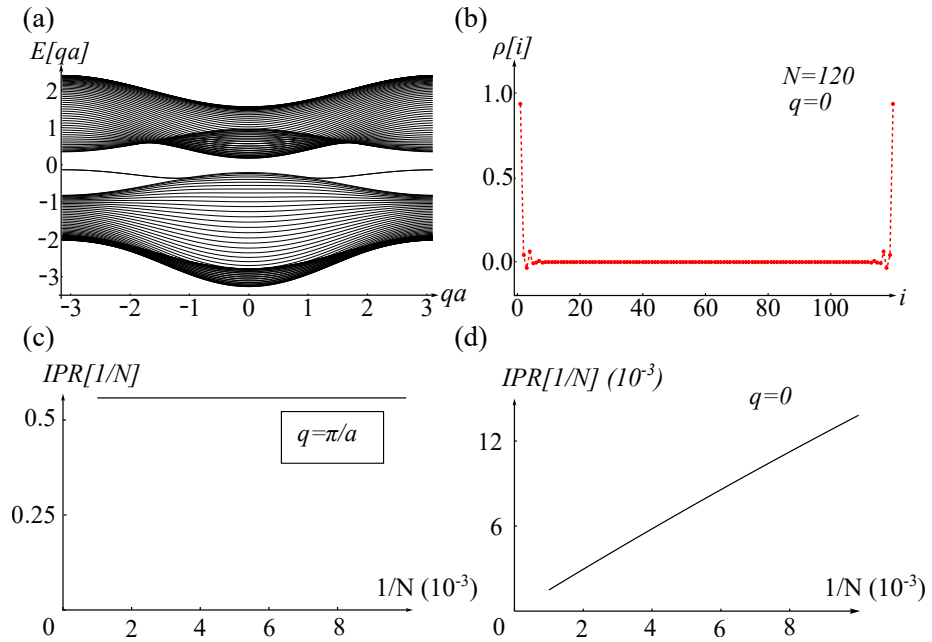


Figure 2.3: (a) Spectrum of a two-band model with $\chi_1 = -1$. (b) Net charge density $\rho(i)$ as a function of the lattice site for $q = 0$ and chain length $N = 120$. (c) IPR of one of the in-gap states at $q = \pi/a$. (d) IPR of the highest-valence band states at $q = 0$.

proportional to $1/N$, whereas for an edge state the IPR goes to a constant value. In Fig. 2.3(c), we plot the IPR for one of the in-gap states at $q_{\parallel} = \pi/a$. We can clearly see that this is indeed an edge state. In contrast, in Fig. 2.3(d) we plot the IPR for the highest-valence band state at $q_{\parallel} = 0$, which can be identified as a bulk state.

2.6 Few-layer Black Phosphorus

Next, we apply our results to an actual 2D material: black phosphorus, which consists of stacked sheets coupled by Van der Waals forces. Recently, it has been possible to isolate individual layers of black phosphorus (phosphorene) by mechanical exfoliation [18–22]. In Figs. 2.4(a) and (b), we display a sketch of such a layer. Like graphene, phosphorene has a honeycomb lattice; however, the bonds in phosphorene result from sp^3 hybridization, which leads to the puckered structure. Phosphorene is a semiconductor, with a band gap that goes from 0.3eV to 2eV, depending on the number of layers. This sizable gap makes it a very promising material for electronic applications. Here, we demonstrate that this novel material features edge states. For this purpose, we use a simple tight-binding model, where each atom hosts one p_z -like orbital [23]. The model can be used to describe both valence- and conduction-band edges in black phosphorus. For a single layer, we can write

$$H = \sum_{i \neq j} t_{i,j}^{\parallel} c_i^{\dagger} c_j, \quad (2.9)$$

where $c_i^{\dagger}(c_i)$ creates (annihilates) an electron at site i , and $t_{i,j}^{\parallel}$ denotes the hopping parameter from site i to site j . In Fig. 4(c), we plot the resulting band structure along the high-symmetry lines connecting the $X - \Gamma - Y$ points, evaluated for the hopping parameters obtained from first-principles calculations [23]. This parametrization includes in total ten different parameters, although qualitatively only the two nearest-neighbor-hopping parameters $t_1^{\parallel} = -1.486\text{eV}$ and $t_2^{\parallel} = 3.729\text{eV}$, shown in Fig. 2.4(a), are required. Inspection of Fig. 2.4(b) indeed confirms that phosphorene exhibits \mathcal{T} symmetry around the center of the unit-cell. In particular, if we label the inequivalent sites in the unit-cell as in Fig. 2.4(b), we find that $\tilde{I} = \sigma_x \otimes \sigma_x$. The \pm signs in the band structure denote the eigenvalues of \tilde{I} . Using these eigenvalues, we can easily calculate the \mathbb{Z}_2 invariants χ_x and χ_y associated

2.6 Few-layer Black Phosphorus

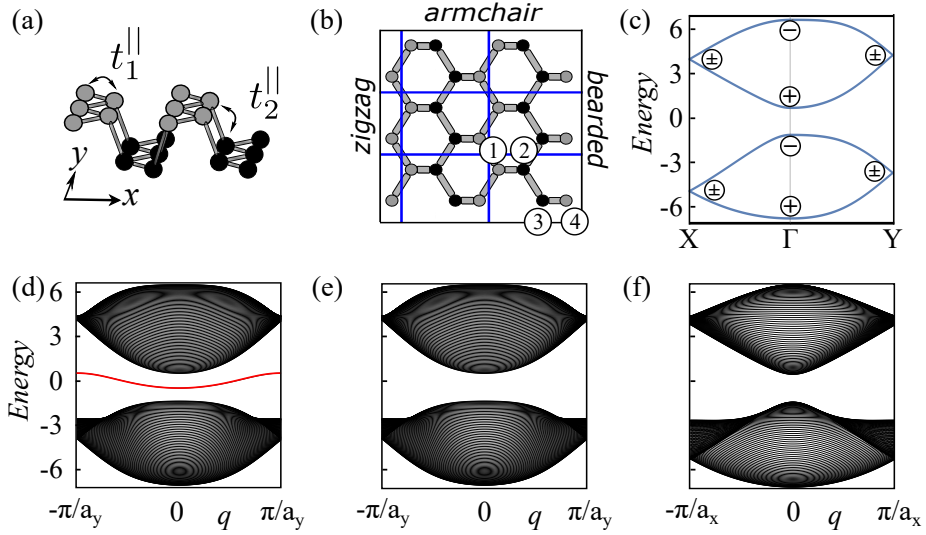


Figure 2.4: (a) Bird's eye view of single-layer black phosphorus. (b) Top view. (c) Bulk band structure along high-symmetry lines, where the \pm signs indicate the parities of the Bloch waves. (d), (e), and (f) Spectra of ribbons single-layer black phosphorus with zigzag, bearded, and armchair edges, respectively.

2 Topological origin of edge states in inversion-symmetric insulators and semi-metals

with edges along the x and y directions, respectively; we find $\chi_x = \chi_y = +1$. From this result, we can immediately infer that both bearded and armchair phosphorene [see Fig. 2.4(b)], do not feature edge states. However, zigzag-terminated phosphorene cannot be tiled with an integer number of unit-cells. Therefore, we cannot simply infer the presence of edge states from χ_y . Instead, Eq. (2.7) states that we need to account for the ionic charge e contained in the broken unit cell at the edge, see Fig. 2.4(b). The surface charge is given by $\sigma(q_{\parallel}) = e\gamma_{\text{Zak}}(q_{\parallel})/\pi + e = e$. Hence, we expect the presence of edge states for zigzag-terminated phosphorene. These conclusions are confirmed by plotting the three different spectra, see Figs. 2.4(d), (e), and (f). Here, only zigzag-terminated phosphorene exhibits one pair of in-gap edge states, which can be attributed to the surface charges (shown in red).

We can repeat this analysis for *bilayer* black phosphorus, for which the structure is shown in Figs. 2.5(a) and (e). Note that the second layer is displaced by half a lattice vector in the zigzag direction, but the stacking respects the C_2 symmetry. One can also study this system using a tight-binding model

$$H = \sum_{i \neq j} t_{i,j}^{\parallel} c_i^{\dagger} c_j + \sum_{i \neq j} t_{i,j}^{\perp} c_i^{\dagger} c_j, \quad (2.10)$$

where we have now included interlayer hopping $t_{i,j}^{\perp}$. In Fig. 2.5(a), we have pictured the dominant interlayer hopping $t_1^{\perp} = 0.524\text{eV}$. The resulting bulk-band structure is shown in Fig. 5(i). The two bulk \mathbb{Z}_2 invariants are trivial, $\chi_x = \chi_y = +1$. This implies that both bearded and armchair bilayer ribbons do not exhibit edge states. For zigzag bilayer phosphorene, we still need to account for the ionic charge in the broken unit-cell at the edge. Inspection of Fig. 5(e) reveals that this contribution is equal to $2e$. However, the surface charge is only well defined modulo $2e$, and thus we expect that all three terminations are topologically trivial. This is confirmed by plotting the three spectra, see Figs. 2.5(b), (c), and (d). Both armchair and bearded bilayer phosphorene do not feature any in-gap states, whereas the zigzag terminated one exhibits two pairs. Although bearded and zigzag terminated bilayer phosphorene feature very different edge physics, they are topologically identical, owing to the \mathbb{Z}_2 nature of the invariant.

It has been noticed in *ab initio* calculations that a potential bias ΔV applied between the two layers can drastically affect the band structure [24].

2.6 Few-layer Black Phosphorus

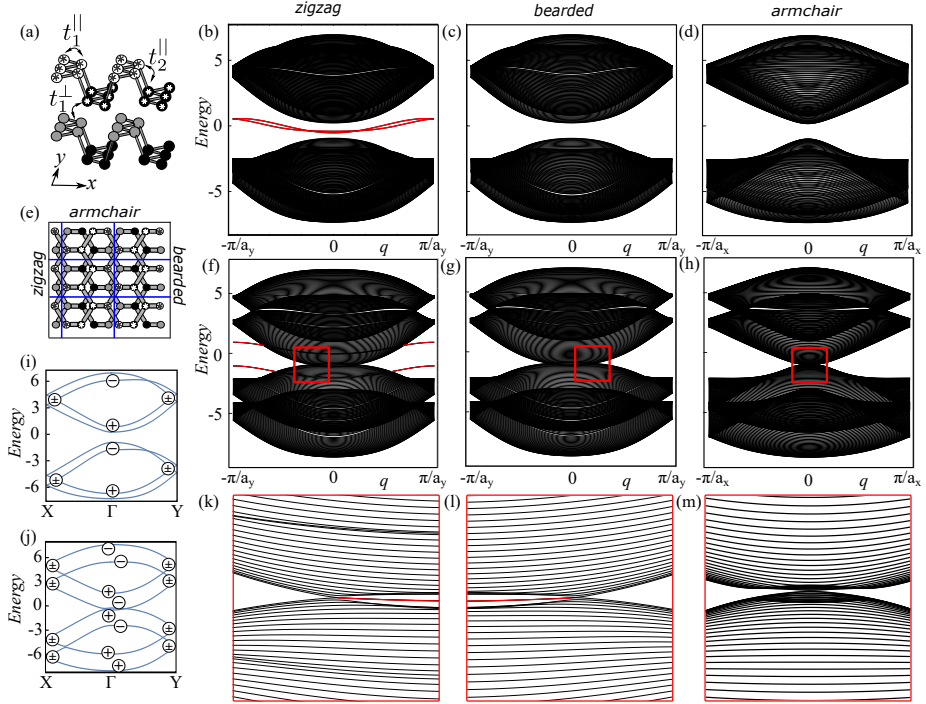


Figure 2.5: (a) Bird's eye view of bilayer black phosphorus. (b) , (c), and (d) Spectra of a ribbon of bilayer black phosphorus with zigzag, bearded and armchair edges, respectively. (e) Top view of bilayer black phosphorus. (f), (g), and (h) Spectra of a biased ribbon of bilayer black phosphorus ($\Delta V = 2eV$), with zigzag, bearded and armchair edges, respectively. (i) and (j) Bulk band structure along high-symmetry lines, for bilayer black phosphorus with $\Delta V = 0$ and $\Delta V = 2eV$, respectively. (k), (l), and (m) close-up of Figs. (f), (g), and (h) around the band-crossing point.

In particular, one can induce a Lifshitz transition if ΔV exceeds a critical value. Then, the valence and conduction band invert, and a band-crossing point emerges along the line connecting the $\Gamma - Y$ points, whereas a small gap is opened along the line connecting the $\Gamma - X$ points, see Fig. 5(j). This band inversion is accompanied by a topological phase transition, such that now $\chi_x = \chi_y = -1$. Hence, by varying this bias potential one transforms an insulator with a trivial \mathbb{Z}_2 invariant, as in Table 2.2(a), into a semimetal with a non-trivial \mathbb{Z}_2 invariant, as in Table 2.2(d). In Figs. 2.5(f) and (g), we plot the spectra for zigzag and bearded bilayer phosphorene. Here, one can indeed see the in-gap edge states located between the two band-crossing points [see also the close-ups in Figs. 2.5(k) and (l)]. These spectra are qualitatively similar to the band structure shown in Table 2.2(d). However, for the ribbon with armchair termination, the spectrum does not exhibit any edge states, see Figs. 2.5(h) and (m). This behavior is grounded on the fact that for this termination, the two band-crossing points coincide at $q_{\parallel} = 0$. This example provides a good illustration of our claim that edge states are a robust feature of Dirac semimetals, and that their existence can be attributed to the Zak phase $\gamma_{\text{Zak}}(q_{\parallel})$, which changes from π to zero as one traverses the band-crossing point. Although we have limited ourselves to single and bilayer black phosphorus, our conclusion can easily be generalized to other few-layer configurations.

2.7 Conclusion and Discussion

In conclusion, we show that the interplay between \mathcal{T} - and \mathcal{I} -symmetry gives rise to a topological \mathbb{Z}_2 invariant χ_1 , which is directly related to the quantization of the Zak phase $\gamma_{\text{Zak}}(q_{\parallel})$ in both insulators and semimetals. In particular, we find that a non-trivial Zak phase generally leads to edge states. Hereby, we have generalized the result by Ryu and Hatsugai [11]. to systems lacking chiral symmetry. Moreover, we have extended the usual classification of 2D \mathcal{I} -symmetric insulators given in Refs. [16, 25].

These results are relevant for a broad range of 2D materials, including graphene, phosphorene and their multi-layer configurations. Our results explain the robust topological origin of edge states in Dirac semimetals, due to the π Zak phase of the Dirac cone. This work, therefore, complements earlier studies on edge states in graphene [26] based on the Dirac equation.

2.7 Conclusion and Discussion

We note that silicene, germanene, stanene, and transition-metal dichalcogenides, which also exhibit similar properties to the previous materials, are excluded from our analysis because of a significant SOC and/or the lack of \mathcal{I} -symmetry.

Experimentally, the presence of edge states may be most easily detected via scanning-tunneling microscope (STM) experiments, which probe the local density of states [27]. For an insulator, the excess density of states at the surface will be quantized, whereas for semimetals it will be proportional to the distance between the two band-crossing points in the reduced 1D BZ [12]. This is particularly relevant for few-layer phosphorene, where a gate voltage can induce an insulator to semimetal transition [24]. In the semimetallic regime, the gate voltage controls the distance in momentum space between the two band-crossing points, and as such it provides new experimental possibilities to verify our predictions. Experimentally, this insulator to semimetal transition has already been realized by depositing potassium atoms on black phosphorus [28, 29]. Therefore, we hope that our work will motivate future STM experiments in few-layer black phosphorus. In order to avoid contamination, one should cleave the black phosphorus and perform the STM experiments in an ultra-high vacuum environment [28].

We would still like to comment on the role of disorder. It has been shown that in 1D insulators, the surface charge is immune to disorder near the edges [30]. Moreover, the surface charges are stable against small amounts of disorder in the bulk, which preserve \mathcal{I} -symmetry on average [31, 32].

Finally, we would like to point out that the relevance of our results is not restricted to 2D materials because the Zak phase has been recently used to explain the existence of drumhead surface states in the three-dimensional materials Cu_3N and Ca_3P_2 [31, 33].

A

A.1 Relation between the Zak phase and eigenvalues of inversion

The Zak phase is defined as $\gamma_{\text{Zak}} = i \int dq \langle u_q | \nabla_q | u_q \rangle$, where u_q is the periodic part of the full Bloch wave function Ψ_q . In a tight-binding model, we find $u_{q,j,\alpha} = e^{-iq(ja+r_\alpha)} \Psi_{q,j,\alpha}$, where j labels the unit-cells, α is an orbital index, and r_α the corresponding location with respect to the center of the j th unit-cell. Note that the inner product is restricted to one unit cell. Furthermore, the Zak phase should be calculated for the periodic gauge, which in terms of the full wave function, translates into $\Psi_q = \Psi_{q+2\pi/a}$. Using the relation between Ψ_q and u_q , we can then rewrite the Zak phase as

$$\gamma_{\text{Zak}} = i \int dq \langle \Psi_q^* | \nabla_q | \Psi_q \rangle + \sum_{\alpha} \int dq |\Psi_{q,\alpha}|^2 r_{\alpha}.$$

The second term on the right-hand side vanishes in the presence of \mathcal{I} -symmetry, since the charge distribution is symmetric around the center of the unit cell. Hence, we can write $\gamma_{\text{Zak}} = i \int dq \langle \Psi_q^* | \nabla_k | \Psi_q \rangle$. Then, for a system without degeneracies, \mathcal{I} -symmetry guarantees that $|\Psi_q\rangle = e^{-i\phi(q)} \tilde{I} |\Psi_{-q}\rangle$, with ϕ some arbitrary phase. Hence, we can rewrite the Zak phase as

$$\begin{aligned} \gamma_{\text{Zak}} &= i \int_0^{\pi} dq \langle \Psi_q | \nabla_q | \Psi_q \rangle + i \int_{-\pi}^0 dq \langle \Psi_q | \nabla_q | \Psi_q \rangle \\ &= i \int_0^{\pi} dq \langle \Psi_q | \nabla_q | \Psi_q \rangle + i \int_{-\pi}^0 dq \langle \Psi_{-q} | \tilde{I} e^{i\phi(q)} \nabla_q e^{-i\phi(q)} \tilde{I} | \Psi_{-q} \rangle \\ &= i \int_0^{\pi} dq \langle \Psi_q | \nabla_q | \Psi_q \rangle + i \int_{-\pi}^0 dq \langle \Psi_{-q} | \nabla_q | \Psi_{-q} \rangle + \int_{-\pi}^0 dq \nabla_q \phi(q) \\ &= i \int_0^{\pi} dq \langle \Psi_q | \nabla_q | \Psi_q \rangle + i \int_{\pi}^0 dq \langle \Psi_q | \nabla_q | \Psi_q \rangle + \int_{-\pi}^0 dq \nabla_q \phi(q) \\ &= \phi(0) - \phi(-\pi). \end{aligned}$$

A

In the penultimate step, we used that $\nabla_q = -\nabla_{-q}$. Although the phase $\phi(q)$ is arbitrary for generic q , this is not true for \mathcal{I} -invariant momenta, as follows from the identity

$$|\Psi_{q_{\text{inv}}}\rangle = e^{i\phi(q_{\text{inv}})} \tilde{I} |\Psi_{q_{\text{inv}}}\rangle = e^{i\phi(q_{\text{inv}})} \xi(q_{\text{inv}}) |\Psi_{q_{\text{inv}}}\rangle.$$

Hence, $\phi(q_{\text{inv}}) = 2\pi j + [\xi(q_{\text{inv}}) - 1]\pi/2$, and thus

$$\gamma_{\text{Zak}} = \phi(0) - \phi(-\pi) = 2\pi(j - j') + [\xi(0) - \xi(-\pi)]\pi/2.$$

A.2 Properties of Zak connection and curvature

In the presence of \mathcal{T} -symmetry, the Zak connection is even up to a total derivative. For simplicity, we consider the case where the \mathcal{T} -operator is represented by complex conjugation \mathcal{K} . Then,

$$\begin{aligned} A(\vec{q}) &= i\langle u_{\vec{q}} | \nabla_{\vec{q}} | u_{\vec{q}} \rangle = i\langle \mathcal{K}u_{-\vec{q}} | e^{-i\phi(\vec{q})} \nabla_{\vec{q}} e^{i\phi(\vec{q})} | \mathcal{K}u_{-\vec{q}} \rangle \\ &= i\langle \mathcal{K}u_{-\vec{q}} | \nabla_{\vec{q}} | \mathcal{K}u_{-\vec{q}} \rangle - \nabla_{\vec{q}}\phi(\vec{q}) = -i\langle u_{-\vec{q}} | \nabla_{\vec{q}} | u_{-\vec{q}} \rangle - \nabla_{\vec{q}}\phi(\vec{q}) \\ &= i\langle u_{-\vec{q}} | \nabla_{-\vec{q}} | u_{-\vec{q}} \rangle - \nabla_{\vec{q}}\phi(\vec{q}) = A(-\vec{q}) - \nabla_{\vec{q}}\phi(\vec{q}). \end{aligned}$$

In the presence of \mathcal{I} -symmetry, the Zak connection is odd up to a total derivative,

$$\begin{aligned} A(\vec{q}) &= i\langle u_{\vec{q}} | \nabla_{\vec{q}} | u_{\vec{q}} \rangle = i\langle u_{-\vec{q}} | e^{-i\chi(\vec{q})} \tilde{I} \nabla_{\vec{q}} \tilde{I} e^{i\chi(\vec{q})} | u_{-\vec{q}} \rangle \\ &= i\langle u_{-\vec{q}} | \nabla_{\vec{q}} | u_{-\vec{q}} \rangle - \nabla_{\vec{q}}\chi(\vec{q}) = -i\langle u_{-\vec{q}} | \nabla_{-\vec{q}} | u_{-\vec{q}} \rangle - \nabla_{\vec{q}}\chi(\vec{q}) \\ &= -A(-\vec{q}) - \nabla_{\vec{q}}\chi(\vec{q}). \end{aligned}$$

Hence, from this it follows that the polarization is quantized for an \mathcal{I} -symmetric system, as $\int A(\vec{q}) = -\int A(-\vec{q}) + \int \nabla\chi(\vec{q}) = -\int A(\vec{q}) + 2\pi j$ where the integral is over a symmetric domain. In the presence of both \mathcal{I} and \mathcal{T} -symmetry, the integral along any closed contour is quantized, as we find that $2A(\vec{q}) = \nabla\chi(\vec{q})$.

Finally, at the level of the Zak curvature, \mathcal{T} -symmetry dictates $F(\vec{q}) = -F(\vec{q})$, as the curl of an even function is odd, and \mathcal{I} dictates $F(\vec{q}) = F(-\vec{q})$ as the curl of an odd function is even. Hence, when both \mathcal{T} and \mathcal{I} -symmetry are present, we find $F = 0$.

A.3 Parameters for the two-band toy model

Table A.1 lists the hopping parameters that have been used to obtain the spectra shown in Table 2.2.

	(a)	(b)	(c)	(d)
e_s	-3	-5	-6	-3
e_p	1	3	7	4
t_{1s}	-2	-2	-1	3
t_{2s}	3	3	2	2
t_{1p}	1	4	2	-1
t_{2p}	-4	-3	-1	-3
t_{1sp}	-2	-2	-2	-2
t_{2sp}	4	3	1	3

Table A.1: Parameters used for the band structures from Table 2.2.

A.4 Tight-binding model corresponding to the band structure shown in Fig. 2.3 .

For the band structure shown in Fig. 2.3(a), we have used a tight-binding model that includes long-range hopping. The Fourier transformed bulk Hamiltonian reads

$$\tilde{H}(\vec{q}) = h_I(\vec{q})\mathbb{1} + h_y(\vec{q})\sigma_y + h_z(\vec{q})\sigma_z,$$

with

$$\begin{aligned} h_I(\vec{q}) + h_z(\vec{q}) &= -0.2 - 0.46 \cos(\vec{q} \cdot \vec{a}_1) + 2.15 \cos(\vec{q} \cdot \vec{a}_2), \\ h_I(\vec{q}) - h_z(\vec{q}) &= -0.52 - 0.29 \cos(\vec{q} \cdot \vec{a}_1) - 0.58 \cos(\vec{q} \cdot \vec{a}_2) + 0.6 \cos(2\vec{q} \cdot \vec{a}_2) \\ &\quad + 0.3 \cos(\vec{q} \cdot (\vec{a}_1 + 2\vec{a}_2)) + 0.3 \cos(\vec{q} \cdot (-\vec{a}_1 + 2\vec{a}_2)), \\ h_y(\vec{q}) &= 1.81 \sin(\vec{q} \cdot \vec{a}_2). \end{aligned}$$

3 Berry phase approach to excess charges

The electronic properties of both insulating and metallic crystals are largely characterized by the electronic band structure: It relates the crystal momentum q to the corresponding energy $E_n(q)$, with n the band index. In an insulator the Fermi level lies in a band gap separating the conduction from the valence bands, whereas in metals the Fermi level intersects an energy-momentum curve. Although the bulk band structure plays an indispensable role in describing optical, magnetic, and electrical properties of materials, it does not describe all the relevant electronic properties, even in a simple single-particle picture. Edge effects are a notable example.

In topological states of matter the presence of metallic edge states mandated by topology cannot be extracted from the bulk band structure [2, 3]. Surface Dirac cones in three-dimensional (3D) topological insulators [34–39] and crystalline topological insulators [25, 40–43], Fermi arcs in 3D Weyl semimetals [44–49], chiral and helical edge states in two-dimensional (2D) insulators [9, 50–53] are all exceptional features escaping the conventional bulk band structure picture. These are instead encoded in the bulk Hamiltonian. Being a completely general phenomenon, however, edge effects inevitably appear also in metals as well as in insulating states of matter which are topologically trivial according to the Altland-Zirnbauer classification [4–7]. In particular, this applies to one-dimensional (1D) insulators that do not carry a topological invariant in the absence of particle-hole and chiral symmetry. In these systems, the presence of edges does not yield additional localized metallic modes but the different boundary conditions do affect the wave function.

Put in simple terms, the electronic wave functions of infinitely large systems with periodic boundary conditions correspond to modulated plane waves, whereas a system with edges exhibits standing waves. Close to the edges, this different nature of the electronic wavefunctions leads to fluctuations in the the total electronic charge density. In metals, these fluctuations are known as Friedel oscillations, which decay algebraically with a wavelength $\lambda_{\text{Friedel}} = 1/(2q_F)$, q_F being the Fermi momentum [54]. In insulators

3 Berry phase approach to excess charges

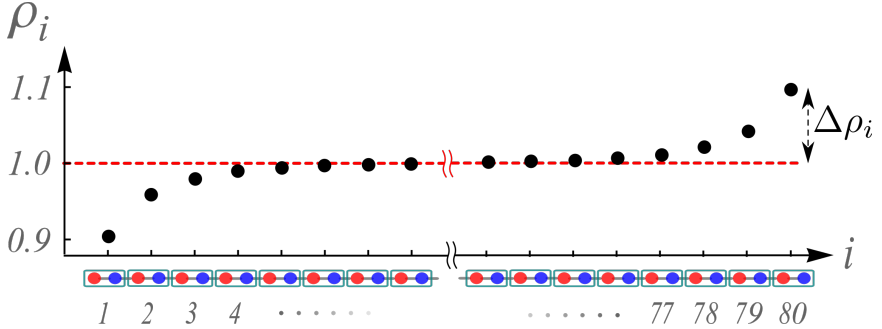


Figure 3.1: Charge density per unit-cell ρ_i for a binary chain with open boundary conditions and $M = 80$: the green rectangle denotes the preferred unit-cell, the red (blue) sites have onsite energies m ($-m$), and the hopping parameter is given by t , which we assume to be positive. Here we used $m/t = 0.25$.

instead, the charge deviations die out exponentially fast [55]. Consider for instance a finite one-dimensional atomic binary chain at half-filling: very close to the edges the electronic charge per unit cell ρ_i starts deviating from its bulk value [c.f. Fig. 3.1]. This deviation can be quantified by defining the total (excess) edge charge Q_L as the sum of the local charge deviations [30, 56, 57] $\Delta\rho_i = \rho_i - N_F$, where N_F denotes the number of filled bands ($N_F = 1$ for a the half-filled binary chain of Fig. 3.1), i.e.

$$Q_L := \lim_{l \rightarrow \infty} \sum_{i=1}^l \Delta\rho_i. \quad (3.1)$$

In the equation above, the thermodynamic limit $l \rightarrow \infty$ explicitly accounts for a semi-infinite system, and we introduced the subindex L to indicate that we refer to the left edge of the atomic chain. The edge charge, as defined in Eq. (3.1), can be numerically calculated up to $1/M$ corrections by considering a finite chain with a large number M of unit cells, and summing the local charge deviations in half of it.

It turns out, however, that this edge effect can be exactly quantified using the geometric phase of the individual bulk electronic Bloch waves. In complete analogy with, e.g., two-dimensional time-reversal symmetry-broken topological insulators, where the number of chiral edge channels is given as an integral of the Berry curvature [8], the total edge charge in conventional

insulators can be expressed as an integral of the Berry potential. Such a relation has been shown in one-dimensional (1D) systems in Ref. [58]. Specifically, the integral of the Berry potential over the one-dimensional Brillouin zone (BZ) yields an intra- and inter-cellular part, with the latter corresponding exactly to the (excess) edge charge Q_L , while the former quantifies the difference between the electronic contribution to the charge polarization and the edge charge itself [14, 15, 59]. In this chapter, we will exploit this relation to show that the excess charge can be formulated in terms of the topological invariants that classify insulating states in one-dimension protected by spatial symmetries [16, 60–63]. In particular, for time-reversal symmetric systems this relation will be uncovered using the notion of partial Berry phases originally introduced by Fu and Kane [64].

The chapter is organized as follows: In Sec. 3.1 we provide the derivation of the relation between the edge charge and the geometric (partial) Berry phase in 1D insulating systems. After reviewing the \mathbb{Z}_2 topology of 1D systems protected by point-group symmetries, we will show in Sec. 3.2 that the edge charge provides a natural probe for these free-fermion symmetry-protected topological (SPT) phases. Finally, we will draw our conclusions in Sec. 3.3.

3.1 Edge charge of 1D systems

In this section, we will demonstrate that the edge charge defined in Eq. (3.1) for an atomic chain can be expressed as:

$$Q_L = -\frac{1}{2\pi} \sum_{n \leq N_F} \int_{-\pi}^{\pi} dq \langle \Psi_n(q) | i\partial_q | \Psi_n(q) \rangle = -\frac{\gamma}{2\pi}. \quad (3.2)$$

Here, $|\Psi_n(q)\rangle$ denotes the entire Bloch wave with band index n and crystal momentum q , and γ is the Berry phase of the Bloch wavefunction $|\Psi_n(q)\rangle$. The inner-product is restricted to a single unit cell. In Appendix B.1 we prove that the Berry phase is identical to the inter-cellular part of the Zak phase identified in Ref. [58]. We stress that Eq. (3.2) holds using the periodic gauge condition: $|\Psi_m(q)\rangle = |\Psi_m(q + 2\pi)\rangle$, where we put the lattice constant $a = 1$. Throughout this chapter we will always require that this periodicity condition will be obeyed.

3 Berry phase approach to excess charges

3.1.1 Notation

Before providing the proof of Eq. (3.2), we introduce our notation. In the remainder we will limit ourselves to tight-binding models. This means that a generic Hamiltonian can be expressed as

$$\hat{H} = \sum_{i,j} \sum_{\alpha,\beta} t_j^{\alpha,\beta} f_{i,\alpha}^\dagger f_{i+j,\beta},$$

where $f_{i,\alpha}^\dagger$ is the creation operator corresponding to an electron in unit-cell i , and the index α , which runs from 1 to N , refers to the electronic internal degrees of freedom. It may therefore correspond to a spin, a sub-lattice or an orbital index. In the example of the binary chain introduced above, α corresponds to the sublattice index. The choice of the unit cell is fixed by the edge under consideration, see for example Fig. 3.1 where the green rectangle denotes a preferred unit cell. To exploit the translation symmetry of the chain, we introduce the Fourier transformed creation and annihilation operators

$$f_{q,\alpha}^\dagger := \sum_{l=1}^M e^{iq_l} f_{l,\alpha}^\dagger / \sqrt{M}.$$

Using these operators we can rewrite the Hamiltonian as

$$\hat{H} = \sum_{q \in BZ} \hat{H}(q) = \sum_{\alpha,\beta} \sum_{q \in BZ} f_{q,\alpha}^\dagger \tilde{H}^{\alpha,\beta}(q) f_{q,\beta},$$

where $\tilde{H}^{\alpha,\beta}(q) = \sum_j t_j^{\alpha,\beta} e^{iqj}$. We refer to $\hat{H}(q)$ as the second-quantized Hamiltonian, while $\tilde{H}(q)$ is its first quantized counterpart. We mention that we will use the same notation for other operators that we will introduce throughout this chapter. We further denote the eigenstates of the first quantized Hamiltonian with $|\Psi_n(q)\rangle = [\Psi_{n,1}(q), \dots, \Psi_{n,N}(q)]^T$, where $n = 1, \dots, N$ is the band index. The real-space wave function with crystal momentum q and band index n within a given unit cell is of course proportional to $|\Psi_n(q)\rangle$.

3.1.2 Derivation

Having introduced the notation, we now move on to derive Eq. (3.2). In Ref. [58], the correspondence between the excess charge and the inter-cellular

3.1 Edge charge of 1D systems

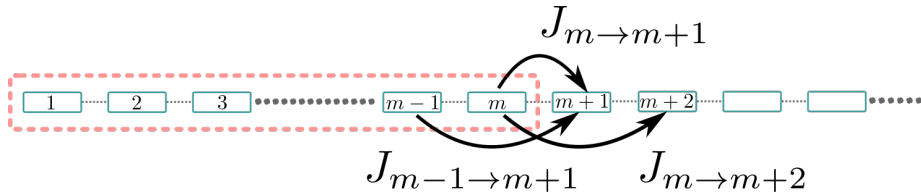


Figure 3.2: One-dimensional chain. The green rectangles denote the unit-cells. The current that flows out of the red rectangular box is given by $J_{m \rightarrow m+1}^{\text{total}} = J_{m \rightarrow m+1} + J_{m-1 \rightarrow m+1} + J_{m \rightarrow m+2} + \dots$

part of the Zak phase has been found making use of Wannier orbitals. Here, we will take instead a different approach. Our proof consists of two parts, and relies on adiabatic deformation of an original Hamiltonian \hat{H}_0 . In the first part, we show that Eq. (3.2) holds for a simple tight-binding model described by the Hamiltonian \hat{H}_0 . In the second part, we imagine that the tight-binding Hamiltonian \hat{H}_0 is adiabatically changed in time. Hence, we assume that we are provided with a one-parameter family of Hamiltonians \hat{H}_λ , where λ denotes the parameter that varies in time. Then, we show that $\Delta Q_L := Q_L(\lambda_f) - Q_L(\lambda_i)$ can be expressed as the difference of the Berry phases $[\gamma(\lambda_i) - \gamma(\lambda_f)]/(2\pi)$. All together, this will prove the validity of Eq. (3.2).

First, let us define \hat{H}_0 by considering an atomic chain where all electrons are completely localized within a unit cell and cannot hop to neighbouring unit cells, i.e. $t_j^{\alpha,\beta} = 0$ for $j \neq 0$. This ensures that for all momenta $\tilde{H}_0(q) = \tilde{H}_0(0)$. Therefore, we find that the corresponding Bloch waves are identical: $|\Psi_n^0(q)\rangle = |\Psi_n^0(0)\rangle$. As a result, the integrand on the right-hand side of Eq. (3.2) vanishes. Since the edge charge for a system of perfectly localized electrons must identically vanish, we have proven that Eq. (3.2) holds for \hat{H}_0 .

Now let us turn to ΔQ_L . By using Eq. (3.1), we can express the derivative of the edge charge as

$$\frac{dQ_L(\lambda(t))}{dt} = \sum_{j=1}^{\infty} \frac{d\rho_j}{dt} \approx \sum_{j=1}^m \frac{d\rho_j}{dt},$$

where m is an arbitrarily large integer and we used that far away from the edges the charge per unit cell is constant. This allows us to write $\frac{d\rho_j}{dt} = 0$

3 Berry phase approach to excess charges

for $j \geq m$. By using the continuity equation, we then find

$$\begin{aligned} \frac{dQ_L(\lambda(t))}{dt} &= -J_{m \rightarrow m+1}^{\text{total}} \\ &= -(J_{m \rightarrow m+1} + J_{m \rightarrow m+2} + J_{m-1 \rightarrow m+1} + \dots) \end{aligned} \quad (3.3)$$

In the equation above, $J_{m \rightarrow m+1}^{\text{total}}$ is the total current flowing through a wall put between unit-cells m and $m+1$ [c.f. Fig. 3.2]. It can be also written as the sum of the currents $J_{j \rightarrow k}$ flowing between two unit cells j and k , with $j \leq m \leq k$. Note that this current does not capture any charge redistributions within the unit cell. These internal charge distributions are important for the charge polarization, but are irrelevant for the edge charge. The corresponding operator can be written as

$$\hat{J}_{m \rightarrow m+1}^{\text{total}}(t) = \sum_{q \in BZ} f_q^\dagger \left[\nabla_q \tilde{H}_{\lambda(t)}(q) \right] f_q + \dots \quad (3.4)$$

where the \dots indicate terms of the form $f_q^\dagger f_{q'}$ that couple different momentum states, *i.e.* $q \neq q'$, and are completely irrelevant for a translational invariant bulk system. We refer the reader to Appendix B.2, for a derivation of Eq. (3.4). Next, we consider the case in which λ varies adiabatically slowly in time. This allows us to use the near-adiabatic approximation [65, 66], and express the wavefunction at time t as

$$\begin{aligned} |\Psi_n(q, t)\rangle &= e^{if(q,t)} \left(|\Psi_n^{\lambda(t)}(q)\rangle + \right. \\ &\quad \left. i \sum_{m \neq n} \frac{|\Psi_m^{\lambda(t)}(q)\rangle \langle \Psi_m^{\lambda(t)}(q)| \partial_t \Psi_n^{\lambda(t)}(q)\rangle}{E_m^{\lambda(t)}(q) - E_n^{\lambda(t)}(q)} \right). \end{aligned} \quad (3.5)$$

Here, $|\Psi_n^{\lambda}(q)\rangle$ denotes the ‘‘snapshot’’ Bloch wave function corresponding to $\hat{H}_\lambda(q)$, $E_n^\lambda(q)$ its instantaneous eigen energy, and f is an arbitrary real-valued function. Combining Eqs. (3.3), (3.4), and (3.5), we then obtain that the change in edge charge reads

$$\begin{aligned} \Delta Q_L &= \frac{-i}{2\pi} \sum_{n \leq N_F} \sum_{m \neq n} \int_{t_i}^{t_f} dt \int_{-\pi}^{\pi} dq \langle \Psi_n^{\lambda(t)}(q) | \left[\nabla_q \tilde{H}_{\lambda(t)}(q) \right] | \Psi_m^{\lambda(t)}(q) \rangle \\ &\quad \times \langle \Psi_m^{\lambda(t)}(q) | \partial_t \Psi_n^{\lambda(t)}(q) \rangle (E_m^{\lambda(t)}(q) - E_n^{\lambda(t)}(q))^{-1} + h.c., \end{aligned}$$

3.1 Edge charge of 1D systems

where we have replaced the sum over q by an integral. To make further progress, we eliminate the sum over m by using

$$\partial_q |\Psi_n^\lambda(q)\rangle = \sum_{m \neq n} \frac{\langle \Psi_m^\lambda(q) | [\nabla_q \tilde{H}_\lambda(q)] | \Psi_n^\lambda(q) \rangle}{E_n^\lambda(q) - E_m^\lambda(q)} |\Psi_m^\lambda(q)\rangle + ig(q) |\Psi_n^\lambda(q)\rangle,$$

where g is an arbitrary real-valued function that does not contribute to the integral. Hence, we find

$$\Delta Q_L = \frac{i}{2\pi} \sum_{n \leq N_F} \int_{t_i}^{t_f} dt \int dq \langle \partial_q \Psi_n^{\lambda(t)}(q) | \partial_t \Psi_n^{\lambda(t)}(q) \rangle + h.c. \quad (3.6)$$

Using Stokes theorem we can rewrite the r.h.s. of the equation above as a line integral. By further imposing the periodic gauge for the wave function $|\Psi_m^\lambda(q)\rangle = |\Psi_m^\lambda(q + 2\pi)\rangle$, Eq. (3.6) assumes the following form

$$\begin{aligned} \Delta Q_L &= -\frac{i}{2\pi} \sum_{n \leq N_F} \int dq \langle \Psi_n^{\lambda_f}(q) | \partial_q \Psi_n^{\lambda_f}(q) \rangle \\ &\quad + \frac{i}{2\pi} \int dq \langle \Psi_n^{\lambda_i}(q) | \partial_q \Psi_n^{\lambda_i}(q) \rangle = \frac{1}{2\pi} (\gamma(\lambda_i) - \gamma(\lambda_f)). \end{aligned}$$

With this, we have shown that the edge charge is indeed given by Eq. (3.2). We note that the Berry phase γ can be conveniently expressed in terms of the trace of the non-Abelian Berry potential $\mathcal{A}_{m,n}(q) = \langle \Psi_m(q) | i\partial_q | \Psi_n(q) \rangle$, with $m, n = 1, \dots, N_F$:

$$\gamma = \int_{-\pi}^{\pi} dq \text{Tr } \mathcal{A}(q). \quad (3.7)$$

This expression is invariant under a $U(N_F)$ gauge transformation $|\Psi_m(q)\rangle \rightarrow \mathcal{U}^{m,n}(q) |\Psi_n(q)\rangle$, for which Eq. (3.7) is transformed accordingly to

$$\text{Tr } \mathcal{A}(q) \rightarrow \text{Tr } \mathcal{A}(q) + i \text{Tr } \mathcal{U}^\dagger(q) \partial_q \mathcal{U}(q) \quad (3.8)$$

Since, \mathcal{U} is a unitary matrix, we find

$$i \text{Tr } \mathcal{U}^\dagger(q) \partial_q \mathcal{U}(q) = i \partial_q \log \det \mathcal{U}(q) \quad (3.9)$$

3 Berry phase approach to excess charges

With this, it follows that $\gamma \rightarrow \gamma + 2\pi j$, with j the winding number $W(\mathcal{U})$ of the determinant of $\mathcal{U}(q)$, which is given by

$$W(\mathcal{U}) = \frac{i}{2\pi} \int_{-\pi}^{\pi} dq \frac{d}{dq} \log \det \mathcal{U}(q).$$

Moreover we point out that the edge charges at the two opposite edges of a one-dimensional chain must compensate each other modulo 1. Note that this is only true if the chain consists of an integer number of unit-cells. Hence, we can generally write

$$Q = \pm \frac{\gamma}{2\pi}, \quad (3.10)$$

where $+$ ($-$) refers to a right (left) edge. We stress that Eq. (3.10) is completely generic, and can be used to calculate the edge charge for any 1D crystalline insulator.

Let us now take into account the binary chain introduced above to illustrate this result. First we have to choose a termination, which fixes the preferred unit cell. The binary chain can only be terminated in two ways, either with a blue site or with a red site. For the blue (red) termination the preferred unit cell is denoted with a solid (dashed) box in the inset of Fig. 3.3. The corresponding Fourier transformed Hamiltonians $\tilde{H}^{\text{red}}(q)$ and $\tilde{H}^{\text{blue}}(q)$ are given by

$$\tilde{H}^{\text{red}}(q) = \begin{pmatrix} m & -t(1 + e^{-iq}) \\ -t(1 + e^{iq}) & -m \end{pmatrix},$$

and

$$\tilde{H}^{\text{blue}}(q) = \begin{pmatrix} -m & -t(1 + e^{-iq}) \\ -t(1 + e^{iq}) & m \end{pmatrix}.$$

At half-filling the left edge charges corresponding to the blue and red termination are plotted as a function of m/t in Fig. 3.3. Note that both vanish in the limit $|m/t| \rightarrow \infty$. This is expected, as it corresponds to the atomic limit in which the hopping amplitude goes to zero. Moreover, from Fig. 3.3 we immediately notice that $Q^{\text{blue}} = -Q^{\text{red}}$. This follows from the fact that the red and blue termination are related by inversion-symmetry. The same symmetry yields a π jump in the Berry phase at $m = 0$. We will discuss this in more detail in Sec. 3.2. The red dots in Fig. 3.3 are obtained by numerically calculating the left edge charge for a chain with 200 unit cells using Eq. 3.1.

3.1 Edge charge of 1D systems

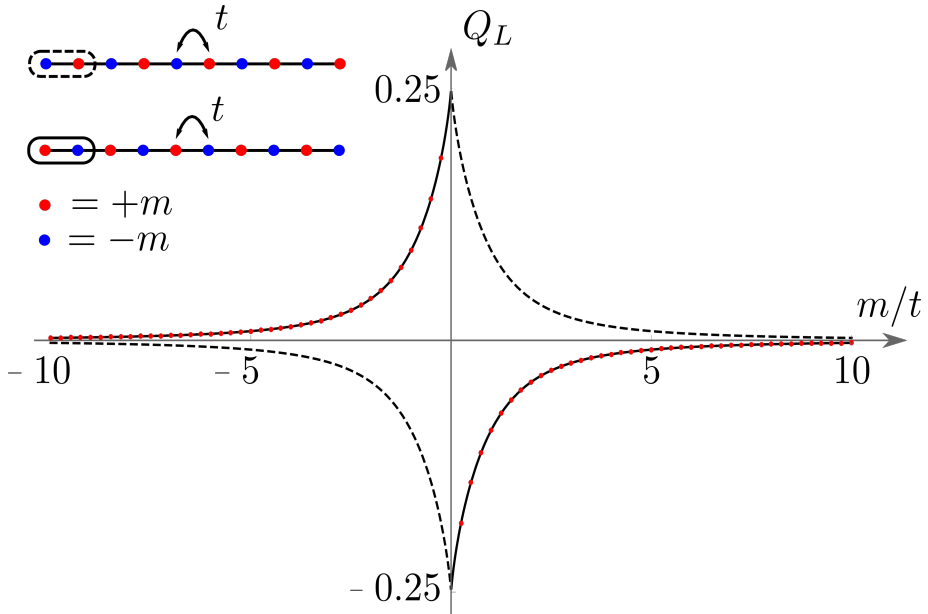


Figure 3.3: The edge charge Q_L for the binary chain. In the inset we display the two possible terminations. The solid and dashed line correspond to the Berry phase result for the red and blue termination, respectively. The red dots denote the values for the edge charge for the red termination, which are obtained by numerical diagonalization for a chain of 200 unit cells at half-filling, using Eq. (3.1).

3 Berry phase approach to excess charges

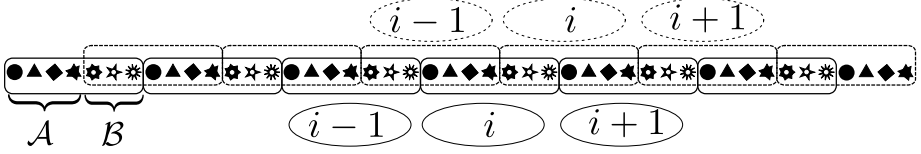


Figure 3.4: One-dimensional chain with two different unit-cells solid and dashed. The solid (dashed) ellipses denote the corresponding labelling of the unit cells. Sites within partition \mathcal{A} are completely black, whereas the sites in partition \mathcal{B} have a white center.

3.1.3 Termination dependence

We next investigate how the edge charges for two different terminations are related. For this purpose we consider a generic tight-binding model, see Fig. 3.4, for a sketch. In addition, we have depicted solid and dashed unit cells, which we refer to as unit cells 1 and 2, respectively. Next, let us analyze how the corresponding creation operators, $f_{i,\alpha,1}^\dagger$ and $f_{i,\alpha,2}^\dagger$ are related. To this end, we partition the unit-cell into two parts, called \mathcal{A} and \mathcal{B} , see Fig. 3.4. We relabel the creation operators in partition $\mathcal{A}(\mathcal{B})$ as $a_{i,\alpha,1}^\dagger(b_{i,\alpha,1}^\dagger)$ and $a_{i,\alpha,2}^\dagger(b_{i,\alpha,2}^\dagger)$. Then, it immediately follows that the creation operators for the two different unit cells are related by

$$\begin{aligned} a_{i,\alpha,1}^\dagger &= a_{i-1,\alpha,2}^\dagger, \\ b_{i,\alpha,1}^\dagger &= b_{i,\alpha,2}^\dagger. \end{aligned}$$

By performing a Fourier transformation and writing $f_{q,1}^\dagger = (a_{q,1}^\dagger, b_{q,1}^\dagger)$ and $f_{q,2}^\dagger = (b_{q,2}^\dagger, a_{q,2}^\dagger)$, we find that

$$f_{q,1}^\dagger = f_{q,2}^\dagger \tilde{U}(q),$$

where the matrix $\tilde{U}(q)$ is given by

$$\tilde{U}(q) = \begin{pmatrix} 0 & 1 \\ e^{iq} & 0 \end{pmatrix}.$$

From this, it follows that the Bloch waves for the two unit-cells are related by $|\Psi_n^2(q)\rangle = \tilde{U}(q)|\Psi_n^1(q)\rangle$. This, in turns, implies that $\gamma^1 = \gamma^2 - 2\pi\rho_{\mathcal{B}}$, where $\rho_{\mathcal{B}}$ denotes the total charge in the \mathcal{B} partition. The knowledge of

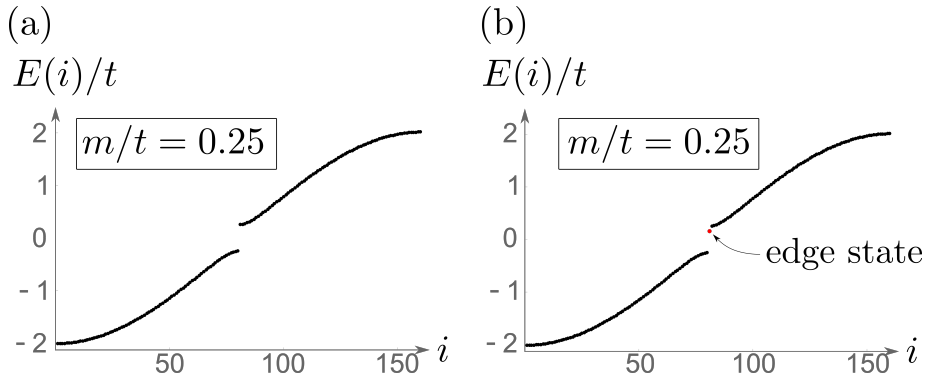


Figure 3.5: Two spectra for the binary chain with 80 unit cells, with different edge potentials. In (a) all red sites are at on-site energy $+m$, whereas in (b) the first red site is at on-site energy $-m$. In (b) the edge potential gives rise to an edge state.

the Berry phase for one unit cell and of the charge distribution within that particular unit-cell then allows to compute the Berry phase for all possible unit cells. For the binary chain we have explicitly verified this relation for the edge charges considering the blue and red terminations.

Finally, let us address the bulk nature of the edge charge. Since the Berry phases are only well-defined up to integer multiples of 2π , we can only predict the fractional part of the edge charge. We emphasize that this is not a limitation of the Berry phase approach, but an intrinsic property of the edge charge. Specifically, the integer part of the edge charge depends on microscopic details of the termination as well as on the Fermi level E_F . For instance, the edge spectrum may host edge states depending on the details of the edge potential. The occupancy of these states, which is controlled by E_F , changes the edge charge by ± 1 . To illustrate this, we consider the binary chain terminated with the red site. If we put the first site at an on-site energy $-m$ instead of $+m$, we find that the spectrum exhibits an in-gap state, see Fig. 3.5. Eq. (3.1) gives $Q_L = (-0.18)0.82$ if this state is (un)-occupied, which agrees with the result of Eq. (3.2) modulo an integer [see Fig. 3.3. This result corroborates the fact that only the fractional part of the excess charge is a bulk quantity, and can be thus expressed as a geometric phase.

3 Berry phase approach to excess charges

3.1.4 Time-reversal symmetry

So far we have considered the edge charge without explicitly invoking time-reversal symmetry. For spin one-half fermions, Kramer's theorem guarantees that every state is necessarily doubly degenerate. In particular, this applies to the in-gap edge states. Using the result above, this also implies that the edge charge can only change by multiples of 2 upon changing the Fermi level, thereby suggesting that the relation between excess charges and quantum-mechanical geometric phases can be refined when explicitly accounting for time-reversal symmetry.

We start out by considering that time-reversal symmetry imposes the following constraints:

$$\hat{H}(q) = \hat{T}\hat{H}(-q)\hat{T}^{-1} \quad \text{and} \quad \hat{T}^2 = -1,$$

with \hat{T} the anti-unitary time-reversal symmetry operator. This constraint ensures that the band structure consists of pairs of bands, which touch at the time-reversal invariant momenta, see Fig. 3.6(b). We label the different pairs by $n = 1, \dots, N_F/2$. Moreover, for a given pair with index n and momentum q , we refer to the two states as $|\Psi_n^I(q)\rangle$ and $|\Psi_n^{II}(q)\rangle$. Let us for the moment assume that we have found a smooth time-reversal symmetric gauge, i.e.

$$|\Psi_n^{II}(q)\rangle = \tilde{T}|\Psi_n^I(-q)\rangle. \quad (3.11)$$

Where \tilde{T} is the first-quantized anti-unitary operator corresponding to \hat{T} . Using this decomposition, we can rewrite Eq. (3.6) as

$$\begin{aligned} \Delta Q_L &= \frac{i}{2\pi} \sum_{n \leq N_F/2} \int_{t_i}^{t_f} dt \int_{-\pi}^{\pi} dq \langle \partial_q \Psi_n^{I,\lambda(t)}(q) | \partial_t \Psi_n^{I,\lambda(t)}(q) \rangle \\ &+ \frac{i}{2\pi} \sum_{n \leq N_F/2} \int_{t_i}^{t_f} dt \int_{-\pi}^{\pi} dq \langle \partial_q \Psi_n^{II,\lambda(t)}(q) | \partial_t \Psi_n^{II,\lambda(t)}(q) \rangle + h.c. \\ &= \frac{i}{\pi} \sum_{n \leq N_F/2} \int_{t_i}^{t_f} dt \int_{-\pi}^{\pi} dq \langle \partial_q \Psi_n^{I,\lambda(t)}(q) | \partial_t \Psi_n^{I,\lambda(t)}(q) \rangle + h.c. \\ &= \frac{1}{\pi} (\gamma^I(\lambda_i) - \gamma^I(\lambda_f)), \end{aligned}$$

3.1 Edge charge of 1D systems

where in the final line we have employed Stokes' theorem to rewrite the surface integral as a contour integral, and introduced the partial Berry phase[64] γ^I which is defined modulo 2π . This confirms that the edge charge in time-reversal symmetric systems is indeed well-defined modulo 2, and expressed in terms of the partial Berry phase by

$$Q = \pm \sum_{n \leq N_F/2} \frac{1}{\pi} \int_{-\pi}^{\pi} dq \langle \Psi_n^I(q) | i\partial_q | \Psi_n^I(q) \rangle = \pm \gamma^I / \pi. \quad (3.12)$$

In the equation above, the $+$ ($-$) refers again to the right (left) edge.

Since it is not always an easy task to find a smooth gauge in time-reversal symmetric systems, we next wish to find a formulation of Eq. (3.12), which is invariant under an arbitrary gauge transformation. First, let us point out that the time-reversal symmetric gauge Eq. (3.11), assures that

$$\langle \Psi_n^I(q) | i\partial_q | \Psi_n^I(q) \rangle = \langle \Psi_n^{II}(-q) | i\partial_{-q} | \Psi_n^{II}(-q) \rangle.$$

This allows us to express the partial Berry phase as an integral of the trace of the non-Abelian Berry potential over half the Brillouin zone

$$\gamma^I = \int_0^{\pi} dq \text{Tr } \mathcal{A}(q). \quad (3.13)$$

Next, we introduce the sewing matrix $\mathcal{S}_{\tilde{T}}(q)$ whose entries are given by

$$[\mathcal{S}_{\tilde{T}}(q)]^{m,n} = \langle \Psi_m(-q) | \tilde{T} | \Psi_n(q) \rangle.$$

The sewing matrix is anti-symmetric at the time-reversal invariant momenta $q = 0, \pi$, and as such can be characterized by its Pfaffian. As long as Eq. (3.11) is obeyed, we find that

$$\text{Pf } \mathcal{S}_{\tilde{T}}(\pi) / \text{Pf } \mathcal{S}_{\tilde{T}}(0) = 1. \quad (3.14)$$

Since, the log of 1 is zero, we can freely add Eq. (3.14) to Eq. (3.13),

$$\gamma^I = \int_0^{\pi} dq \text{Tr } \mathcal{A}(q) + i \log (\text{Pf } \mathcal{S}_{\tilde{T}}(\pi) / \text{Pf } \mathcal{S}_{\tilde{T}}(0)) \quad (3.15)$$

The advantage of this expression is that it is invariant under an arbitrary $U(N_F)$ gauge transformation. Using Eqs. (3.8) and (3.9), we find that under

3 Berry phase approach to excess charges

a gauge transformation the first term in the r.h.s. of the equation above changes by

$$i \log \det \mathcal{U}(\pi) / \det \mathcal{U}(0).$$

The sewing matrices instead transform as

$$\begin{aligned} \mathcal{S}_{\tilde{T}}(0) &\rightarrow \mathcal{U}^\dagger(0) \mathcal{S}_{\tilde{T}}(0) \mathcal{U}(0)^* \\ \mathcal{S}_{\tilde{T}}(\pi) &\rightarrow \mathcal{U}(\pi)^\dagger \mathcal{S}_{\tilde{T}}(\pi) \mathcal{U}(\pi)^*. \end{aligned}$$

Using the fact that $\text{Pf } XAX^T = \text{Pf } A \det X$, we find that the second term in the r.h.s. of Eq. (3.15) changes by

$$i \log \left[\det \mathcal{U}^\dagger(\pi) / \det \mathcal{U}^\dagger(0) \right] = -i \log \left[\det \mathcal{U}(\pi) / \det \mathcal{U}(0) \right].$$

Hence, this proves that the right hand side of Eq. (3.15) is gauge invariant and does not necessitate Eq. (3.11) to be fulfilled.

To numerically confirm these results, let us consider a spinful version of the binary chain. Assuming that the orbitals are real, we find that the time-reversal operator $\tilde{T} = \mathbb{1} \otimes i\sigma_2 \mathcal{K}$, where the identity acts on the orbital and sub-lattice degrees of freedom, the second Pauli matrix σ_2 on the spin, and \mathcal{K} corresponds to complex conjugation. In addition to the spinless part, we add both intrinsic and Rashba spin-orbit coupling. The former manifests itself through complex next-nearest neighbour hoppings, see Fig. 3.6(a). The corresponding Hamiltonian reads

$$\tilde{H}_{\text{ISO}}(q) = \lambda_{\text{ISO}} \begin{pmatrix} 2 \sin(q) & 0 \\ 0 & -2 \sin(q) \end{pmatrix} \otimes \sigma_3$$

The Rashba spin-orbit coupling is given instead by

$$\begin{aligned} \tilde{H}_{\text{RSO}}(q) &= i\lambda_{\text{RSO}} \begin{pmatrix} 0 & 1 \\ -1 & 0 \end{pmatrix} \otimes \left(\frac{\sqrt{3}}{2} \sigma_2 + \frac{1}{2} \sigma_1 \right) - \\ & i\lambda_{\text{RSO}} \begin{pmatrix} 0 & e^{-iq} \\ -e^{iq} & 0 \end{pmatrix} \otimes \left(\frac{\sqrt{3}}{2} \sigma_2 - \frac{1}{2} \sigma_1 \right). \end{aligned}$$

It is easily verified that $\tilde{H}_{\text{ISO}}(q) = \tilde{T} \tilde{H}_{\text{ISO}}(-q) \tilde{T}$ and $\tilde{H}_{\text{RSO}}(q) = \tilde{T} \tilde{H}_{\text{RSO}}(-q) \tilde{T}$. The corresponding band structure is depicted in Fig. 3.6(b), where we used

3.1 Edge charge of 1D systems

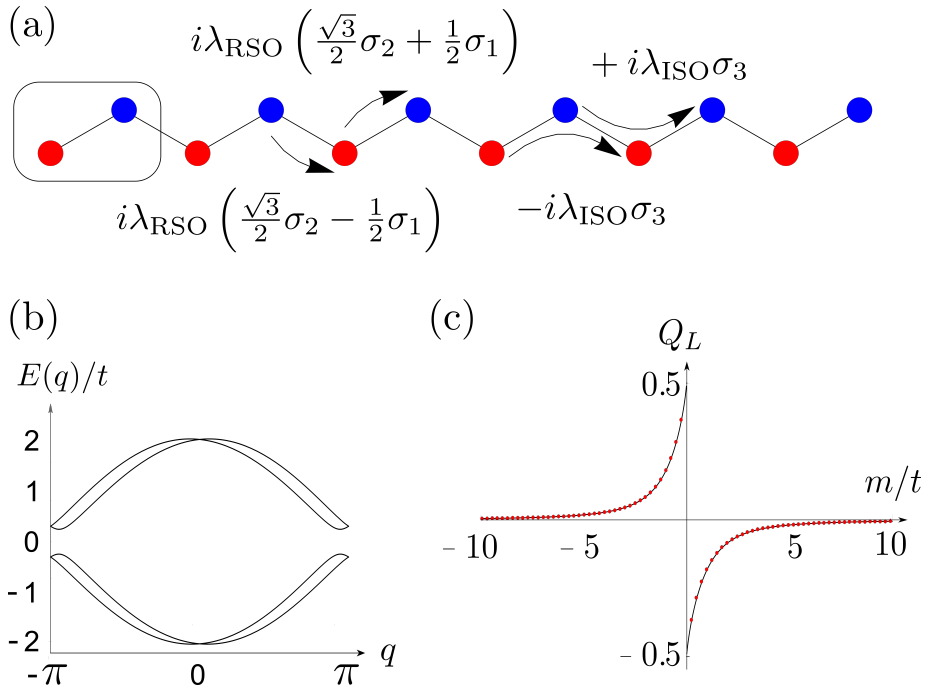


Figure 3.6: Spinfull binary chain. (a) Spin-orbit coupling terms are schematically depicted with arrows. (b) Typical band structure for a system consisting of spin one-half electrons in the presence of time-reversal symmetry. Note the Kramer's degeneracies at $q = 0$ and $q = \pi$. (c) The edge charge for the spin-full binary chain. The solid line corresponds to the partial Berry phase result, whereas the red dots are obtained by numerical diagonalization for an open chain of 200 unit cells. Here, we have chosen $\lambda_{\text{ISO}}/t = \lambda_{\text{RSO}}/t = 1/10$.

3 Berry phase approach to excess charges

$m/t = 0.25$ and $\lambda_{\text{RSO}}/t = \lambda_{\text{ISO}}/t = 1/10$. Note that apart from the time-reversal invariant momenta the bands are completely spin-split. The edge charge is calculated using the partial Berry phase γ^I for various values of m/t , see Fig. 3.6(c). The red dots denote the values obtained for the edge charges by numerical diagonalization for a chain of 200 unit-cells at half-filling. And indeed we find that the partial Berry phase correctly predicts the edge charges mod 2.

3.1.5 Numerical considerations

To compute a (partial) Berry phase one should find a smooth gauge. In practice, this requires to impose a certain gauge-fixing condition. For example, one might fix the gauge by requiring that the wave function is strictly real and positive at a certain site. However, such a gauge-fixing condition becomes ill-defined if the wave-function vanishes at this site. Fortunately, there is an easier method to calculate (partial) Berry phases, see for example Ref. [14]. Here, we briefly discuss these methods.

Suppose that $|\Psi_n(q)\rangle$ is a smooth gauge. Then we can define the $N_F \times N_F$ overlap matrix

$$\mathcal{S}_{m,n}(q_1, q_2) := \langle \Psi_m(q_1) | \Psi_n(q_2) \rangle.$$

This yields

$$\mathcal{S}(q, q + \epsilon) = e^{-i\epsilon \mathcal{A}(q)} + \mathcal{O}(\epsilon^2).$$

Let now $q_j := j2\pi/N$, with $j = 0, 1, \dots, N$, be a discretization of the 1D BZ. If we use that $\det[\mathcal{S}(q, q + \epsilon)] = e^{-i\epsilon \text{Tr}[\mathcal{A}(q)]}$, we find

$$\lim_{N \rightarrow \infty} \det \left[\prod_{i=0}^{N-1} \mathcal{S}(q_i, q_{i+1}) \right] = e^{-i\gamma}.$$

Note that the l.h.s. of the equation above is invariant under an arbitrary $U(N_F)$ gauge transformation $|\Psi_m(q_i)\rangle \rightarrow \mathcal{U}^{m,n}(q_i) |\Psi_n(q_i)\rangle$, as long as the periodicity $|\Psi_m(q_0)\rangle = |\Psi_m(q_N)\rangle$ is respected. This removes the necessity to find a smooth gauge. More importantly, it provides a practical method to calculate the Berry phase.

3.2 Edge charge as a probe of band structure topology

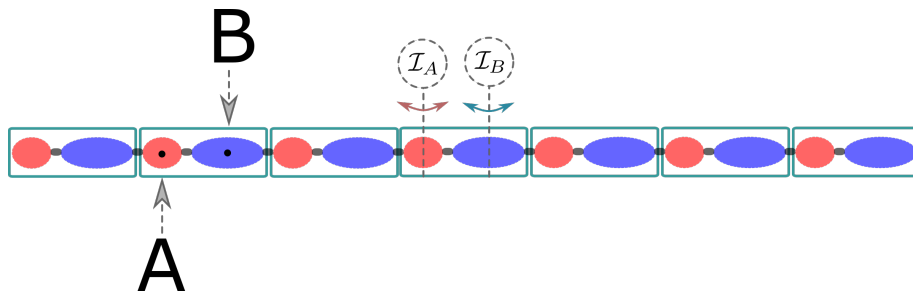


Figure 3.7: Generic inversion-symmetric crystal. The symmetry centers are denoted with **A** and **B**.

Similarly, one can calculate the partial Berry phase γ^I . Following the same steps as above we find

$$\lim_{N \rightarrow \infty} \det \left[\prod_{i=0}^{N-1} \mathcal{S}(\tilde{q}_i, \tilde{q}_{i+1}) \right] \cdot \frac{\text{Pf } \mathcal{S}_{\tilde{T}}(\pi)}{\text{Pf } \mathcal{S}_{\tilde{T}}(0)} = e^{-i\gamma^I},$$

where we introduced the mesh $\tilde{q}_j = j\pi/N$. The l.h.s. of the equation above provides a practical method to calculate the partial Berry phase.

3.2 Edge charge as a probe of band structure topology

In this section we will discuss the \mathbb{Z}_2 -classification of 1D crystalline insulators that are invariant under spatial symmetries interchanging the left and right edges of a chain [67–71], and show that the edge charge can be used to probe the corresponding crystalline topological invariants. We will restrict our analysis to inversion, two-fold rotation, and mirror symmetry, and, as before, we will first not explicitly invoke the fermionic time-reversal symmetry.

When one considers a point-group symmetry in a crystal, one should always specify the symmetry-center. In particular, an inversion-symmetric one-dimensional chain exhibits two points of inversion per unit-cell, to which we refer as *A* and *B*, see Fig. 3.7. Without loss of generality, we consider the case in which *B* sits to the right of *A* within the unit cell. Now let us consider how the canonical creation operators $f_{i,\alpha}^\dagger$ transform under inversion. To be as general as possible, we allow for a non-inversion symmetric unit-cell. We partition this unit cell into two parts, called *A* and *B*, centered

3 Berry phase approach to excess charges

around the inversion points A and B , respectively, see Fig 3.7. We denote the creation operators corresponding to orbitals and spin in part \mathcal{A} (\mathcal{B}) with $a_{i,\alpha}^\dagger$ ($b_{i,\alpha}^\dagger$), such that $f_i^\dagger = (a_{i,1}^\dagger, \dots, a_{i,n_A}^\dagger, b_{i,1}^\dagger, \dots, b_{i,n_B}^\dagger)$. Next, we consider how the electrons transform under inversion. Inspection of Fig. 3.7 shows that under inversion through A (B) the electrons in partition \mathcal{A} within unit cell i transform to partition \mathcal{A} in unit cell $-i$ ($-i + 1$). Hence, if \hat{I}_A (\hat{I}_B) denotes the corresponding inversion operator, then we find

$$\begin{aligned}\hat{I}_A a_{i,\alpha}^\dagger \hat{I}_A^{-1} &= a_{-i,\beta}^\dagger \tilde{I}_A^{\beta,\alpha}, \text{ and} \\ \hat{I}_B a_{i,\alpha}^\dagger \hat{I}_B^{-1} &= a_{-i+1,\beta}^\dagger \tilde{I}_A^{\beta,\alpha}.\end{aligned}$$

Similarly, we find that the electrons in partition \mathcal{B} and unit cell i are sent to partition \mathcal{B} within the $(-i - 1)$ th ($-i$ th) unit cell, upon inverting through point A (B). Hence, we find

$$\begin{aligned}\hat{I}_A b_{i,\alpha}^\dagger \hat{I}_A^{-1} &= b_{-i-1,\beta}^\dagger \tilde{I}_B^{\beta,\alpha}, \text{ and} \\ \hat{I}_B b_{i,\alpha}^\dagger \hat{I}_B^{-1} &= b_{-i,\beta}^\dagger \tilde{I}_B^{\beta,\alpha}.\end{aligned}$$

Next, we apply a Fourier transformation, and combine the above equations by writing $\hat{I}_A f_{q,\alpha}^\dagger \hat{I}_A^{-1} = f_{-q,\beta}^\dagger \tilde{I}_A^{\beta,\alpha}(q)$, with

$$\tilde{I}_A(q) = \begin{pmatrix} \tilde{I}_A & 0 \\ 0 & e^{-iq} \tilde{I}_B \end{pmatrix}.$$

Similarly, we find $\hat{I}_B f_{q,\alpha}^\dagger \hat{I}_B^{-1} = f_{-q,\beta}^\dagger \tilde{I}_B^{\beta,\alpha}(q)$, with

$$\tilde{I}_B(q) = \begin{pmatrix} e^{iq} \tilde{I}_A & 0 \\ 0 & \tilde{I}_B \end{pmatrix}.$$

Since inversion symmetry squares to one, we find

$$\tilde{I}_A(q) \tilde{I}_A(-q) = 1 = \tilde{I}_B(q) \tilde{I}_B(-q). \quad (3.16)$$

In addition, we like to point out that $\tilde{I}_A(q) = e^{-iq} \tilde{I}_B(q)$. Hence, all properties of $\tilde{I}_B(q)$ can be obtained from $\tilde{I}_A(q)$. Therefore we limit ourselves in the following to $\tilde{I}_A(q)$.

3.2 Edge charge as a probe of band structure topology

The fact that the Hamiltonian is inversion symmetric ensures that the Fourier transformed Hamiltonians $\hat{H}(q)$ $\hat{H}(-q)$ are related by

$$\hat{I}_A \hat{H}(q) \hat{I}_A^{-1} = \hat{H}(-q),$$

which reduces to

$$\tilde{I}_A(q) \tilde{H}(q) \tilde{I}_A^{-1}(q) = \tilde{H}(-q), \quad (3.17)$$

using the first-quantized Hamiltonians. Armed with this structure, one can consider the sewing matrix $\mathcal{S}_{\tilde{I}_A}(q)$, given by

$$\left[\mathcal{S}_{\tilde{I}_A}(q) \right]^{m,n} = \langle \Psi_m(-q) | \tilde{I}_A(q) | \Psi_n(q) \rangle. \quad (3.18)$$

Here, Eq. (3.17) guarantees that $\mathcal{S}_{\tilde{I}_A}(q)$ is a unitary matrix. Together with the fact that $\mathcal{S}_{\tilde{I}_A}(q)$ is 2π periodic, we can consider, assuming a smooth gauge for the Bloch wavefunctions, the winding number $W(\mathcal{S}_{\tilde{I}_A})$ of the determinant of the sewing matrix

$$W(\mathcal{S}_{\tilde{I}_A}) := \frac{i}{2\pi} \int_{-\pi}^{\pi} dq \frac{d}{dq} \log \det \mathcal{S}_{\tilde{I}_A}(q) \in \mathbb{Z} \quad (3.19)$$

Naively, one might believe that $W(\mathcal{S}_{\tilde{I}_A})$ yields a \mathbb{Z} classification of 1D inversion-symmetric insulators. However, this winding number is not gauge-invariant. Under a gauge transformation $|\Psi_m(q)\rangle \rightarrow \mathcal{U}^{m,n}(q) |\Psi_n(q)\rangle$, we find that $\det \mathcal{S}_{\tilde{I}_A}(q) \rightarrow \det \mathcal{U}^\dagger(-q) \det \mathcal{S}_{\tilde{I}_A}(q) \det \tilde{\mathcal{U}}(q)$. It follows that $W(\mathcal{S}_{\tilde{I}_A}) \rightarrow W(\mathcal{S}_{\tilde{I}_A}) + 2j$, where j is the winding number of the determinant of $\tilde{\mathcal{U}}(q)$. Hence, the winding number $W(\tilde{I}_A)$ represents a \mathbb{Z}_2 -invariant, instead of a \mathbb{Z} -invariant. To simplify this expression, we use that Eq. (3.16) implies

$$\frac{d}{dq} \left[\det \mathcal{S}_{\tilde{I}_A}(q) \det \mathcal{S}_{\tilde{I}_A}(-q) \right] = 0.$$

Hence, the integrand in Eq. (3.19) is even. As a result, we can write

$$W(\mathcal{S}_{\tilde{I}_A}) = \frac{i}{\pi} \left[\log \det \mathcal{S}_{\tilde{I}_A}(\pi) - \log \det \mathcal{S}_{\tilde{I}_A}(0) \right].$$

3 Berry phase approach to excess charges

This drastically simplifies the calculation of the \mathbb{Z}_2 invariant, since it frees us from the task of finding a smooth gauge over the full Brillouin zone. To define a \mathbb{Z}_2 invariant that takes values in the set $\{-1, 1\}$, we introduce

$$\begin{aligned}\xi_{I_A} &:= e^{-i\pi W(\tilde{I}_A)} = \det \mathcal{S}_{\tilde{I}_A}(\pi) / \det \mathcal{S}_{\tilde{I}_A}(0) \\ &= (-1)^{N_F} \det \mathcal{S}_{\tilde{I}_B}(\pi) / \det \mathcal{S}_{\tilde{I}_B}(0) =: (-1)^{N_F} \xi_{I_B}\end{aligned}$$

In the third line we used that $\det \mathcal{S}_{\tilde{I}_B}(\pi) = \det -\mathcal{S}_{\tilde{I}_A}(\pi)$. We stress that these invariants do not depend in any way on the choice of unit cell or origin, and can therefore be considered as proper bulk invariants.

We can repeat the same analysis for mirror and rotation-symmetric insulators. The difference compared to inversion symmetry is that $\hat{M}_A^2 = \hat{M}_B^2 = (-1)^{2s} = \hat{C}_{2,A}^2 = \hat{C}_{2,B}^2$. Here \hat{M}_A ($\hat{C}_{2,A}$) and \hat{M}_B ($\hat{C}_{2,B}$) are the mirror (rotation)-symmetry operators corresponding to mirror planes (rotation axes) A and B , and s is the total spin. However, this does not affect any of the above derivations. Hence, for mirror-symmetric systems the winding number of the determinant of the sewing matrix $\mathcal{S}_{\tilde{M}_A}$ yields a \mathbb{Z}_2 classification. We characterize the parity of the winding number using the invariants ξ_{M_A} and ξ_{M_B} , which are given by

$$\begin{aligned}\xi_{M_A} &:= e^{-i\pi W(\tilde{M}_A)} = \det \mathcal{S}_{\tilde{M}_A}(\pi) / \det \mathcal{S}_{\tilde{M}_A}(0) \\ &= (-1)^{N_F} \det \mathcal{S}_{\tilde{M}_B}(\pi) / \det \mathcal{S}_{\tilde{M}_B}(0) =: (-1)^{N_F} \xi_{M_B}.\end{aligned}$$

Similarly, we define the invariant $\xi_{C_{2,A}}$ corresponding to rotation symmetry. With this, we have seen that the sewing matrices play a key role within the topological classification of inversion-, rotation, or mirror-symmetric crystalline insulators.

Let us now explore how the edge charge is related to these invariants. Considering inversion-symmetric systems and from the definition of the sewing matrices, it follows that

$$|\Psi_m(-q)\rangle = \left[\mathcal{S}_{\tilde{I}_A}^*(q) \right]^{m,n} \tilde{I}_A(q) |\Psi_n(q)\rangle.$$

3.2 Edge charge as a probe of band structure topology

Therefore, we obtain

$$\begin{aligned}
\text{Tr } \mathcal{A}(-q) &= \sum_n \langle \Psi_n(-q) | i\partial_{-q} | \Psi_n(-q) \rangle \\
&= - \sum_{l,m,n} \langle \Psi_l(q) | \tilde{I}_A^\dagger(q) \left[\mathcal{S}_{\tilde{I}_A}(q) \right]^{n,l} i\partial_q \left[\mathcal{S}_{\tilde{I}_A}^*(q) \right]^{n,m} \tilde{I}_A(q) | \Psi_m(q) \rangle \\
&= - \sum_n \langle \Psi_n(q) | i\partial_q | \Psi_n(q) \rangle - \text{Tr} \left[\mathcal{S}_{\tilde{I}_A}(q) i\partial_q \mathcal{S}_{\tilde{I}_A}^\dagger(q) \right] \\
&\quad - \sum_n \langle \Psi_n(q) | \tilde{I}_A^\dagger(q) i\partial_q \tilde{I}_A(q) | \Psi_n(q) \rangle.
\end{aligned}$$

Next, we note that

$$\tilde{I}_A^\dagger(q) i\partial_q \tilde{I}_A(q) = \begin{pmatrix} 0 & 0 \\ 0 & \mathbb{1}_{n_{\mathcal{B}} \times n_{\mathcal{B}}} \end{pmatrix}.$$

As a result, we find

$$\begin{aligned}
\text{Tr } \mathcal{A}(-q) &= - \text{Tr } \mathcal{A}(q) - \text{Tr} \left[\mathcal{S}_{\tilde{I}_A}(q) i\partial_q \mathcal{S}_{\tilde{I}_A}^\dagger(q) \right] - \rho_{\mathcal{B}}(q) \\
&= - \text{Tr } \mathcal{A}(q) - i \frac{d}{dq} \log(\det \mathcal{S}_{\tilde{I}_A}^\dagger(q)) - \rho_{\mathcal{B}}(q). \tag{3.20}
\end{aligned}$$

Here $\rho_{\mathcal{B}}(q)$ is the charge contained in partition \mathcal{B} . After integrating over all momenta, we finally obtain

$$\gamma = i \log(\xi_{I_A}) - \pi \rho_{\mathcal{B}}.$$

Analogous expressions hold for rotation and mirror-symmetric insulators. Hence, in these systems we can express the edge charge as the sum of a topological and a non-topological part. Since the latter can be measured independently in the bulk, we conclude that the edge charge can indeed probe the topological \mathbb{Z}_2 invariant discussed above. Moreover, we stress that $\rho_{\mathcal{B}}$ depends continuously on external parameters, and therefore any discontinuity in the edge charge can be only ascribed to a change in the band structure topology. Finally, we note that the edge charge can assume any value, except when the preferred unit cell is inversion-symmetric. Then, $\mathcal{B} = \emptyset$, which implies that the excess charge is quantized and given by $Q = i \log(\xi_{X_A})/2\pi$, with $X = I, M$, or C_2 .

3 Berry phase approach to excess charges

Let us now elucidate these results by considering two examples. First, we study the binary chain. Here, we choose the unit cell with the red site at on-site energy $+m$. Note that both the red and blue sites are inversion centers. We refer to the inversion center corresponding to the red sites as A . For this choice of unit cell, the Hamiltonian is given by

$$\tilde{H}(q) = \begin{pmatrix} m & -t(1 + e^{-iq}) \\ -t(1 + e^{iq}) & -m \end{pmatrix}.$$

Moreover, the inversion operator corresponding to the inversion center A reads

$$\tilde{I}_A(q) = \begin{pmatrix} 1 & 0 \\ 0 & e^{-iq} \end{pmatrix}.$$

Hence, at half-filling we find that $\det \mathcal{S}_{\tilde{I}_A}(0) = 1$, since the inversion operator is the identity matrix at $q = 0$. For $q = \pi$, we have $\tilde{I}_A(0) = \sigma_3$. Therefore, we find $\det \mathcal{S}_{\tilde{I}_A}(\pi) = -\text{sign}(m/t)$. Combining these results, we have that $\xi_{I_A} = -\text{sign}(m/t)$, and therefore the edge charge Q is given by

$$Q = \begin{cases} 1/2 + \rho_B/2 & \text{if } \text{sign}(m/t) > 0 \\ \rho_B/2 & \text{if } \text{sign}(m/t) < 0. \end{cases}$$

This result implies that the jump in the edge charge encountered in Fig. 3.3 follows from a change in the topology of the band structure.

Next, let us consider another well known toy-model that is inversion-symmetric: the Su-Schrieffer-Heeger (SSH) chain [72], depicted in Fig. 3.8. This chain consists of alternating solid and dashed bonds. These bonds are centers of inversion, which is in sharp contrast with the binary chain where the sites are inversion centers. We choose a unit cell with the dashed bond as its center. Since, the unit cell itself is inversion-symmetric we find that $\mathcal{B} = \emptyset$. Hence, for this chain we expect a quantized edge charge. We refer to the solid bond as A , and the dashed bond joining the unit cells as bond B . The corresponding hopping parameters are denoted with t_A and t_B . Using this notation, the Hamiltonian is given by

$$\tilde{H}(q) = \begin{pmatrix} 0 & -t_A - t_B e^{-iq} \\ -t_A - t_B e^{iq} & 0 \end{pmatrix}.$$

3.2 Edge charge as a probe of band structure topology

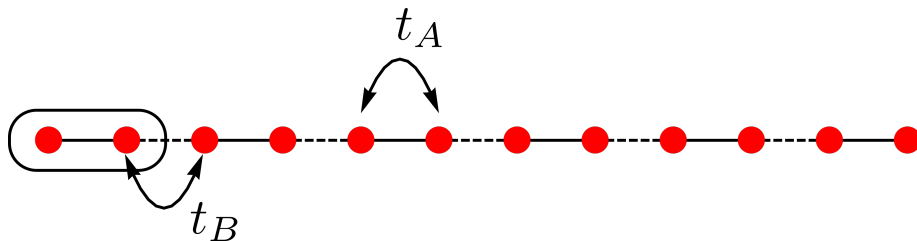


Figure 3.8: Sketch of the SSH chain, the inter- (intra) unit-cell hopping is denoted with a dashed (solid) bond.

Under inversion, we find that the left and right sites are interchanged. Hence, the inversion operator is given by

$$\tilde{I}_A(q) = \begin{pmatrix} 0 & 1 \\ 1 & 0 \end{pmatrix}.$$

Note that the inversion operator is momentum independent, because all electrons belong to partition \mathcal{A} . At half-filling we find that $\xi_{I_A} = \text{sign}(1 - t_B^2/t_A^2)$. Here, we have used that the lowest energy state, assuming t_A to be a positive energy, at $q = 0$ is given by $(1, -\text{sign}(1 + t_B/t_A))^T/\sqrt{2}$ and at $q = \pi$ by $(1, -\text{sign}(1 - t_B/t_A))^T/\sqrt{2}$. Hence, the edge charge is given by

$$Q = \begin{cases} 0 & \text{if } \text{sign}(1 - t_B^2/t_A^2) > 0 \\ 1/2 & \text{if } \text{sign}(1 - t_B^2/t_A^2) < 0. \end{cases}$$

We have numerically confirmed this result by computing the edge charge in a finite chain consisting of 100 unit cells, with $t_A/t_B = 2(\xi_{I_A} = 1)$, and $t_A/t_B = 1/2(\xi_{I_A} = -1)$.

Having established the generic relation between the excess charges and \mathbb{Z}_2 topological crystalline invariants, let us now consider the specific case of spin-one-half systems with time-reversal symmetry. First, we show that time-reversal symmetry implies that the topological invariants ξ_{I_A} , $\xi_{C_{2,A}}$, and ξ_{M_A} introduced above are guaranteed to be trivial. When considering inversion-symmetric systems we can indeed write

$$\det \mathcal{S}_{\tilde{I}_A}(q) = \prod_{j=1}^{N_F} \langle \Psi_j(q) | \tilde{I}_A(q) | \Psi_j(q) \rangle = \prod_{j=1}^{N_F} \zeta_j(q),$$

3 Berry phase approach to excess charges

where $\zeta_j(q)$ denotes the eigenvalues of the sewing matrix and $|\Psi_j(0)\rangle$ the corresponding eigenstate. Then we find $\tilde{I}_A(0)\tilde{T}|\Psi_j(0)\rangle = \zeta^*(0)\tilde{T}|\Psi_j(0)\rangle$, and Kramer's theorem guarantees that these states are orthogonal. Hence, it follows that the $\det S_{\tilde{I}_A}(0) = 1$. We can repeat the same argument for $q = \pi$. Therefore, we find $\xi_{I_A} = 1 = \xi_{I_B}$. This argument can be repeated for systems with two-fold rotation or mirror symmetry.

Fortunately, this also offers new possibilities. Due to the π -periodicity of the determinant, for inversion-symmetric crystals we might consider the winding number $W_{\tilde{I}_A}^{1/2}$ of $\det S_{\tilde{I}_A}$ over half of the Brillouin zone, i.e. from 0 to π

$$W^{1/2}(S_{\tilde{I}_A}) := \frac{i}{2\pi} \int_0^\pi dq \frac{d}{dq} \log(\det S_{\tilde{I}_A}(q)) \in \mathbb{Z}. \quad (3.21)$$

When considering an arbitrary gauge transformation, however, this winding number changes by an arbitrary integer. As such $W^{1/2}(S_{\tilde{I}_A})$ has no meaning at all. However, if one imposes the time-reversal symmetric gauge, Eq. (3.11), then this winding number can only change by integer multiples of 2. To see this, let us suppose that we have found such a smooth time-reversal symmetric gauge. Then under a gauge transformation $|\Psi_m^\alpha(q)\rangle \rightarrow \mathcal{U}_{\alpha,\beta}^{m,n}(q)|\Psi_n^\beta(q)\rangle$. To respect the time-reversal symmetry constraint, one requires

$$\mathcal{U}_{\alpha,\beta}^{m,n}(q)^* = - \sum_{\gamma,\delta} \epsilon_{\alpha,\gamma} \mathcal{U}_{\gamma,\delta}^{m,n}(-q) \epsilon_{\delta,\beta}. \quad (3.22)$$

Where, $\epsilon_{\alpha,\beta} = -\epsilon_{\beta,\alpha}$, and $\epsilon_{I,II} = 1$. This implies that $\det \mathcal{U}^\dagger(q) = \det -\mathcal{U}(-q) = \det \mathcal{U}(-q)$. Hence, under this gauge transformation we have $\det S_{\tilde{I}_A}(q) \rightarrow \det S_{\tilde{I}_A}(q)(\det U(q))^2$. Moreover, Eq. (3.22) ensures that $\det U(0) = \det U(\pi) = 1$. Combining these relations, we find $W_{\tilde{I}_A}^{1/2} \rightarrow W_{\tilde{I}_A}^{1/2} + 2j$, with j the winding number of the determinant of \mathcal{U} over half of the Brillouin zone.¹ Analogously, to ξ_{I_A} and ξ_{I_B} , we can then finally introduce the invariants χ_{I_A} and

¹For completeness we note that one may drop the time-reversal symmetry constraint Eq. (3.11), by writing

$$W^{1/2}(S_{\tilde{I}_A}) = \frac{i}{2\pi} \int_0^\pi dq \frac{d}{dq} \log(\det S_{\tilde{I}_A}(q)) + \frac{i}{2\pi} \left[\int_0^\pi dq \frac{d}{dq} \log(\det S_{\tilde{T}}(q)) - 2 \log \left(\frac{\text{Pf } S_{\tilde{T}}(\pi)}{\text{Pf } S_{\tilde{T}}(0)} \right) \right].$$

3.2 Edge charge as a probe of band structure topology

χ_{I_B} :

$$\chi_{I_A} := e^{i\pi W_{I_A}^{1/2}} = (-1)^{N_F/2} e^{i\pi W_{I_B}^{1/2}} =: (-1)^{N_F/2} \chi_{I_B}$$

These considerations also allow to define the \mathbb{Z}_2 topological crystalline invariants for rotation- and mirror-symmetric systems. However, there is a fundamental difference between these symmetries. Namely, for rotation and mirror-symmetric systems we find $(\hat{R}\hat{T})^2 = (\hat{M}\hat{T})^2 = 1$, whereas for inversion-symmetric systems we find $(\hat{I}\hat{T})^2 = -1$. As a consequence, in inversion-symmetric and time-reversal symmetric systems the bands are two-fold degenerate, whereas the band structure of mirror-symmetric and rotation-symmetric crystals generally exhibits degeneracies only at the time-reversal symmetric momenta 0 and π . Kramer's theorem therefore ensures that in inversion-symmetric insulators the sewing matrix is block diagonal, *i.e.* $\langle \Psi_m^{II}(q) | \tilde{I}_A(-q) | \Psi_n^I(q) \rangle = 0$, provided the time-reversal constraint Eq. (3.11) is fulfilled. Since the determinant of a block-diagonal matrix is the product of the determinants of the individual blocks, we have $\det S_{\tilde{I}_A}^I(q) = \det S_{I_A}^I(q) \det S_{\tilde{I}_A}^{II}(q)$, which when using that

$$\langle \Psi_m^{II}(-q) | \tilde{I}_A(q) | \Psi_n^{II}(q) \rangle = \langle \Psi_n^I(-q) | \tilde{I}_A(q) | \Psi_m^I(q) \rangle$$

, yields $\det S_{\tilde{I}_A}^I(q) = \det S_{I_A}^I(q)^2$. Using Eq. (3.21) we now find

$$\begin{aligned} W^{1/2}(\mathcal{S}_{\tilde{I}_A}^I) &= \frac{i}{\pi} \int_0^\pi dq \frac{d}{dq} \log(\det \mathcal{S}_{\tilde{I}_A}^I(q)) \\ &= \frac{i}{\pi} \left[\log \det \mathcal{S}_{\tilde{I}_A}^I(\pi) - \log \det \mathcal{S}_{\tilde{I}_A}^I(0) \right], \end{aligned}$$

which finally allows to express the \mathbb{Z}_2 topological invariant as

$$\chi_{I_A} = \det \mathcal{S}_{\tilde{I}_A}^I(\pi) / \det \mathcal{S}_{\tilde{I}_A}^I(0).$$

As a result, the crystalline topological invariant for inversion symmetric atomic chains can be computed using only the knowledge of the eigenstates

If a time-reversal symmetric gauge is employed the r.h.s. of the equation above reduces to Eq. (3.21), and under an arbitrary gauge transformation it can only change by an integer multiple of 2.

3 Berry phase approach to excess charges

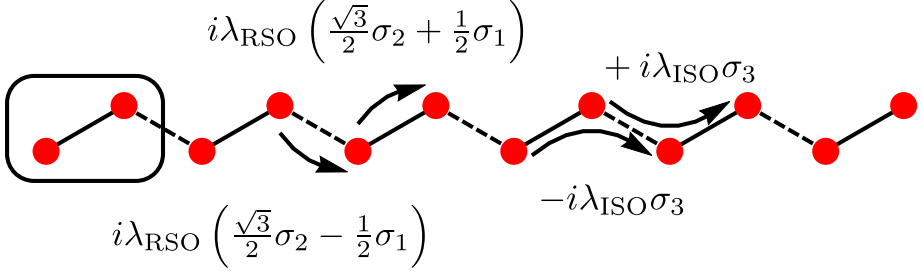


Figure 3.9: Spinfull SSH chain, with C_2 symmetry. Spin-orbit coupling terms are schematically depicted with arrows.

at $q = 0$ and $q = \pi$. This is different from rotation- and mirror-symmetric insulators where one has to find a smooth gauge in the full BZ.

Let us now prove that the crystalline topological invariants χ_{I_A} and χ_{I_B} can be related to the partial Berry phase, which encodes the excess charge in time-reversal symmetric systems. Let us consider the time-reversal symmetric gauge, Eq. (3.11). This ensures that $\mathcal{A}(q) = \mathcal{A}(-q)$. If we combine this with Eq. (3.20) we then find

$$\text{Tr } \mathcal{A}(q) = -\text{Tr } \mathcal{A}(q) - i \frac{d}{dq} \log(\det \mathcal{S}_{I_A}^\dagger(q)) - \rho_B(q),$$

which, when integrated from 0 to π yields the following relation between the partial Berry phase and the \mathbb{Z}_2 topological invariants:

$$\gamma^I = -i \log(\chi_{I_A}) - \pi \rho_B / 2.$$

We now apply this result to a toy model, that can be seen as a spinful SSH atomic chain. In the absence of spin-orbit coupling the Hamiltonian is given by

$$\tilde{H}_0(q) = \begin{pmatrix} 0 & -t_A - t_B e^{-iq} \\ -t_A - t_B e^{iq} & 0 \end{pmatrix} \otimes \sigma_0,$$

where σ_0 is the identity operator acting in spin-space. Let us in addition assume that the electrons are described by p_z -orbitals pointing out of the plane. We then find that the intrinsic spin-orbit coupling induces complex next-nearest neighbor hoppings, see Fig. 3.9. The corresponding Fourier

3.2 Edge charge as a probe of band structure topology

transformed Hamiltonian term reads

$$\tilde{H}_{\text{ISO}}(q) = \lambda_{\text{ISO}} \begin{pmatrix} 2 \sin(q) & 0 \\ 0 & -2 \sin(q) \end{pmatrix} \otimes \sigma_3.$$

Consequently, the full Hamiltonian reads $\tilde{H}(q) = \tilde{H}_0(q) + \tilde{H}_{\text{ISO}}(q)$. Since inversion-symmetry acts trivially in spin space, we find

$$\tilde{I}_A(q) = \begin{pmatrix} 0 & 1 \\ 1 & 0 \end{pmatrix} \otimes \sigma_0.$$

Using that $\tilde{H}_{\text{ISO}}(0) = \tilde{H}_{\text{ISO}}(\pi) = 0$, we find that the invariants for the spinful and spinless SSH chain are identical, i.e. $\chi_{I_A} = \text{sign}(1 - t_B^2/t_A^2)$. Hence, the edge charge is given by $Q = i \log(\text{sign}(1 - t_B^2/t_A^2))/\pi$. We have numerically verified this result by computing the edge charge of atomic chains of 100 unit cells for the cases $t_A = 2t_B = 10\lambda_{\text{ISO}}$, and $t_B = 2t_A = 10\lambda_{\text{ISO}}$.

We can also analyze the situation in which the SSH chain lies on a substrate that breaks the out-of-plane reflection symmetry. This leaves us with a 2-fold rotational symmetry around A and B . The corresponding rotation operator is given by

$$\tilde{C}_{2,A}(q) = \begin{pmatrix} 0 & 1 \\ 1 & 0 \end{pmatrix} \otimes i\sigma_3,$$

where we used that a two-fold rotation around the \hat{z} axis can be represented as $i\sigma_3$ in spin space. This rotation symmetry is preserved when we include a Rashba spin-orbit coupling due to the broken mirror symmetry in the \hat{z} direction. The Rashba spin-orbit coupling indeed yields nearest-neighbor hoppings accompanied by spin-flips (see Fig. 3.9) with an Hamiltonian term:

$$\begin{aligned} \tilde{H}_{\text{RSO}}(q) &= \lambda_{\text{RSO},A} \begin{pmatrix} 0 & 1 \\ -1 & 0 \end{pmatrix} \otimes \left(\frac{\sqrt{3}}{2}\sigma_2 + \frac{1}{2}\sigma_1 \right) \\ &+ \lambda_{\text{RSO},B} \begin{pmatrix} 0 & e^{-iq} \\ -e^{iq} & 0 \end{pmatrix} \otimes \left(-\frac{\sqrt{3}}{2}\sigma_2 + \frac{1}{2}\sigma_1 \right), \end{aligned}$$

such that the full Hamiltonian is given by $\tilde{H}_0(q) + \tilde{H}_{\text{ISO}}(q) + \tilde{H}_{\text{RSO}}(q)$. Now it is easily verified that $\tilde{C}_{2,A}(q)\tilde{H}(q)\tilde{C}_{2,A}(q)^{-1} = \tilde{H}(-q)$. Hence, we can then compute the \mathbb{Z}_2 invariant $\chi_{C_{2,A}}$. Here we find that for $t_A = 2t_B =$

3 Berry phase approach to excess charges

$10\lambda_{\text{ISO}} = 5\lambda_{\text{RSO,A}} = 5\lambda_{\text{RSO,B}}$ a trivial invariant $\chi_{C_{2,A}} = 1$, whereas for $t_B = 2t_A = 10\lambda_{\text{ISO}} = 5\lambda_{\text{RSO,A}} = 5\lambda_{\text{RSO,B}}$ we find $\chi_{C_{2,A}} = -1$. Indeed we find that in the former case the edge charge is trivial, whereas in the latter case a full electron is missing.

Finally, let us consider the spinful binary chain discussed in Sec. 3.1.4. Inspection of Fig. 3.6(a) reveals that this system is mirror-symmetric. The corresponding symmetry operator is given by

$$\tilde{M}_A(q) = \begin{pmatrix} 1 & 0 \\ 0 & e^{-iq} \end{pmatrix} \otimes i\sigma_1.$$

Next, we calculate the \mathbb{Z}_2 -invariant χ_{M_A} . At half-filling we find, using $(-1)^m/t = 10\lambda_{\text{ISO}} = 10\lambda_{\text{RSO}} = 1$, $\chi_{M_A} = (+1) - 1$. Since, the bulk band gap only closes for $m = 0$, we find that the edge charge is given by

$$Q = \begin{cases} 1 + \rho_B/2 & \text{if } \text{sign}(m/t) > 0 \\ \rho_B/2 & \text{if } \text{sign}(m/t) < 0. \end{cases}$$

Hence, the discontinuity in Fig. 3.6(c) can be attributed to a change in the crystalline topology.

3.3 Conclusions

To wrap up, we have shown that the excess charge in one-dimensional insulators, which do not carry a topological invariant according to the Altland-Zirnbauer classification, can be expressed in terms of the Berry phases of the bulk electronic Bloch waves. In presence of time-reversal symmetry, this relation can be conveniently expressed using the notion of the partial Berry phases. For atomic chains possessing spatial symmetries interchanging the chain ends, excess charges always contain a ‘‘topological’’ contribution directly related to the \mathbb{Z}_2 invariants that can be associated with spatial-symmetric one-dimensional systems. Considering that one-dimensional topological crystalline insulating phases cannot be characterized by the presence of protected end modes – these can be only stabilized by an additional non-spatial symmetry – one can conclude that the bulk-boundary correspondence can be only formulated in terms of excess charges and that the latter can be then used to probe one-dimensional crystalline topologies.

B

B.1 Relation between the Zak phase and the Berry phase

Here, we briefly show that the Berry phase as defined in Eq. (3.2) corresponds to the inter-cellular part of the Zak phase $\gamma_{\text{Zak}}^{\text{inter}}$. The Zak phase γ_{Zak} is expressed in terms of the cell-periodic part of the Bloch wave-function, which is given by

$$u_{n,\alpha}(q) = e^{-iqr_\alpha} \Psi_{n,\alpha}(q). \quad (\text{B.1})$$

Here, r_α denotes the position of the α -th orbital (spin, sub-lattice) within the unit-cell with respect to some reference point. With this, we find

$$\begin{aligned} \gamma &= \sum_{n \leq N_{F,\alpha}} \int_{-\pi}^{\pi} dq u_{n,\alpha}^*(q) e^{-iqr_\alpha} i \partial_q e^{iqr_\alpha} u_{n,\alpha}(q) \\ &= \sum_{n \leq N_{F,\alpha}} \int_{-\pi}^{\pi} dq u_{n,\alpha}^*(q) i \partial_q u_{n,\alpha}(q) - \sum_{n \leq N_{F,\alpha}} \int_{-\pi}^{\pi} dq \rho_{n,\alpha}(q) r_\alpha \\ &= \gamma_{\text{Zak}} - \gamma_{\text{Zak}}^{\text{intra}} =: \gamma_{\text{Zak}}^{\text{inter}} \end{aligned} \quad (\text{B.2})$$

B.2 Current operator

Starting point is the Heisenberg equation of motion:

$$\frac{d\hat{\rho}_i}{dt} = i[\hat{H}, \hat{\rho}_i] \quad (\text{B.3})$$

Let us work out the commutator on the right-hand side. Keeping only terms in the Hamiltonian that contain f_i^\dagger or f_i , we find

$$[\hat{H}, \hat{\rho}_i] = \underbrace{\left[\sum_{j;\alpha,\beta} t_j^{\alpha,\beta} f_{i,\alpha}^\dagger f_{i+j,\beta}, \hat{\rho}_i \right]}_{\text{B2.1}} + \underbrace{\left[\sum_{j \neq 0;\alpha,\beta} t_j^{\alpha,\beta} f_{i-j,\alpha}^\dagger f_{i,\beta}, \hat{\rho}_i \right]}_{\text{B2.2}}. \quad (\text{B.4})$$

B

Next, we work out both terms on the right-hand side by making use of the product rule.

$$\begin{aligned}
(\text{B2.1}) &= \sum_{j;\alpha,\beta} t_j^{\alpha,\beta} \left\{ f_{i,\alpha}^\dagger [f_{i+j,\beta}, \hat{\rho}_i] + [f_{i,\alpha}^\dagger, \hat{\rho}_i] f_{i+j,\beta} \right\} \\
&= \sum_{j;\alpha,\beta} t_j^{\alpha,\beta} \left\{ f_{i,\alpha}^\dagger \delta_{j,0} f_{i+j,\beta} - f_{i,\alpha}^\dagger f_{i+j,\beta} \right\} \\
&= - \sum_{j \neq 0; \alpha, \beta} t_j^{\alpha,\beta} f_{i,\alpha}^\dagger f_{i+j,\beta},
\end{aligned} \tag{B.5}$$

and

$$\begin{aligned}
(\text{B2.2}) &= \sum_{j \neq 0; \alpha, \beta} t_j^{\alpha,\beta} \left\{ f_{i-j,\alpha}^\dagger [f_{i,\beta}, \hat{\rho}_i] + [f_{i-j,\alpha}^\dagger, \hat{\rho}_i] f_{i,\beta} \right\} \\
&= \sum_{j \neq 0; \alpha, \beta} t_j^{\alpha,\beta} f_{i-j,\alpha}^\dagger f_{i,\beta}.
\end{aligned} \tag{B.6}$$

Combining Eqs. (B.3), (B.5), and (B.6) we find

$$\frac{d\hat{\rho}_i}{dt} = -i \sum_{j;\alpha,\beta} t_j^{\alpha,\beta} f_{i,\alpha}^\dagger f_{i+j,\beta} + h.c. = - \sum_j \hat{J}_{i \rightarrow i+j}. \tag{B.7}$$

Here we have defined the current operator as

$$\hat{J}_{i \rightarrow i+j} = i \sum_{\alpha,\beta} t_j^{\alpha,\beta} f_{i,\alpha}^\dagger f_{i+j,\beta} + h.c. \tag{B.8}$$

Next, we express this operator in terms of the Fourier transformed creation and annihilation operators

$$\hat{J}_{i \rightarrow i+j} = i \sum_{q \in \text{BZ}} \sum_{\alpha,\beta} t_j^{\alpha,\beta} e^{iqj} f_{q,\alpha}^\dagger f_{q,\beta} + h.c. + \dots \tag{B.9}$$

The dots correspond to term $f_q^\dagger f_{q'}$ with $q \neq q'$. Now we turn to Eq. (3.4), and write using the above result

$$\begin{aligned}
\hat{J}_{m \rightarrow m+1}^{\text{total}} &= \hat{J}_{m \rightarrow m+1} + \hat{J}_{m-1 \rightarrow m+1} + \hat{J}_{m \rightarrow m+2} + \dots \\
&= i \sum_{q \in \text{BZ}} \sum_{\alpha,\beta} \sum_{j \geq 0} j t_j^{\alpha,\beta} e^{iqj} f_{q,\alpha}^\dagger f_{q,\beta} + h.c. \\
&= i \sum_{q \in \text{BZ}} \sum_{\alpha,\beta} \sum_j j t_j^{\alpha,\beta} e^{iqj} f_{q,\alpha}^\dagger f_{q,\beta}
\end{aligned} \tag{B.10}$$

B.2 Current operator

The third equality follows from the Hermiticity of the Hamiltonian, i.e. $t_j^{\alpha,\beta} = (t_{-j}^{\beta,\alpha})^*$. We recognize that the summand is the derivative of the Hamiltonian $\tilde{H}(q)$, i.e.

$$\hat{J}_{m \rightarrow m+1}^{\text{total}} = \sum_{q \in BZ} f_{q,\alpha}^\dagger \nabla_q \tilde{H}^{\alpha,\beta}(q) f_{q,\beta}. \quad (\text{B.11})$$

4 Dislocation charges as probes of crystalline topology

The majority of topological phases of matter are characterized by anomalous surface states, whose presence or absence is linked to a topological index [2, 3]. The Chern number classifying quantum Hall insulators, for instance, counts the number of chiral states appearing at an isolated edge [8]. Their anomaly clearly resides in the fact that it is impossible to have a one-dimensional (1D) crystal with a different number of right-moving and left-moving electronic channels. For topological phases protected by additional (non)spatial symmetries, surface states are anomalous given the protecting symmetry. Time-reversal symmetry dictates that in a 1D system of spin one-half fermions, the Fermi energy E_F must always intersect an even number of Kramers' pairs, a condition that is clearly violated by the helical edge states of two-dimensional quantum spin-Hall insulators [9, 51–53]. The Dirac cones appearing in three-dimensional topological (crystalline) insulators are yet another example of these surface state anomalies [34–43]. The resolution of this paradox is simple: the Dirac cones, chiral or helical edge state partners appearing at the opposite edge always regularize the system and cancel the anomaly. However, revealing the anomaly of the electronic states at isolated surfaces with local probes gives immediate access to the topological invariant of the system.

Not all topological states of matter are characterized by anomalous surface states. This holds, in particular, for topological crystalline invariants associated to spatial symmetries that interchange the edge or surfaces of the system. In two-dimensional crystals with inversion symmetry, for instance, one can define a $\mathbb{Z}_2 \times \mathbb{Z}_2$ topological invariant corresponding to the quotients of the parities of the Bloch waves at $M = (\pi, \pi)$ and $X_1 = (\pi, 0)$ and M and $X_2 = (0, \pi)$, respectively [16]. Signatures of this crystalline topology can be linked to peculiar properties of both the entanglement spectrum [16], and the electronic contribution to the charge polarization [58, 70]. But the presence of anomalous edge states mandated by topology is not guaranteed

4 Dislocation charges as probes of crystalline topology

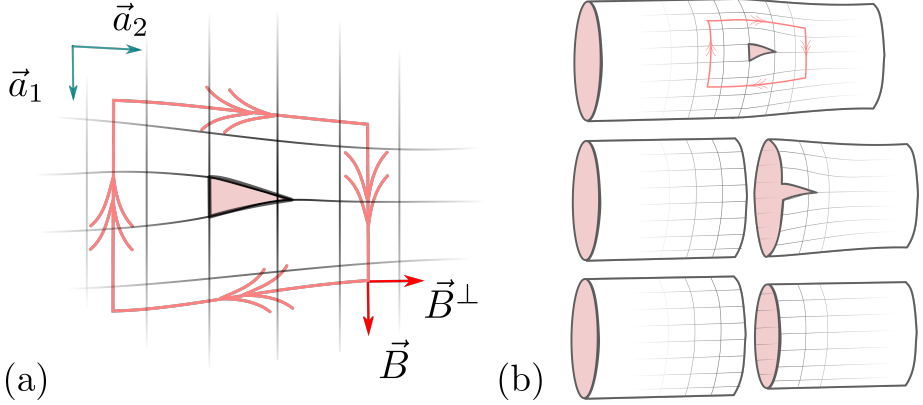


Figure 4.1: (a) Schematic close-up of an edge dislocation. (b) Formation of a dislocation by gluing two cylinders. We find $\vec{B} = \vec{a}_1$, and $\vec{B}^\perp = \vec{b}_2 / (2\pi \|\vec{a}_1 \times \vec{a}_2\|)$. Here, \vec{B}^\perp denotes the vector perpendicular to \vec{B} . The left (right) cylinder has L_1 ($L_1 - 1$) surface unit-cells.

in these crystals. Similarly, the fact that a measurement of the charge polarization of a crystal would concomitantly probe both its ionic and electronic contributions makes it impossible to uniquely probe the crystalline electronic topology.

The aim of this Chapter is to show that the dislocation charge unequivocally reveals the topology of two-dimensional crystals protected by inversion and rotation symmetries. Using a relation between the dislocation charges and the (partial) Berry phases of the bulk crystals, we show indeed that in inversion- and rotation-symmetric insulators the dislocation charge always possesses a topological quantized contribution directly linked to bulk crystalline topological invariants that we identify in our work. Our results complement Refs. [73–75] that relate (Majorana) zero modes bound to dislocations to topological invariants.

4.1 Berry phase formulation of the dislocation charge

Dislocations are topological defects in crystals. They can be associated with a topological invariant, the Burgers vector \vec{B} , which measures the difference between a defect-free and a distorted crystal. It can be defined as follows:

4.1 Berry phase formulation of the dislocation charge

One first traces out a loop surrounding the defect clockwise, and subsequently transfers this loop to a defect-free lattice. Due to the dislocation, the loop will fail to close. The vector that one needs to add to close the loop is the Burgers vector, see Fig. 4.1(a). The presence of this topological defect also produces a local distortion in the otherwise homogeneous charge distribution. For a conventional insulator, in fact, the charge per unit cell ρ_i^z in the vicinity of the dislocation core will deviate from its bulk value N_F , the number of occupied bands. Albeit the precise details of the charge distribution will depend on microscopic details, the dislocation charge Q , defined as the sum of the local charge deviations $\Delta\rho_i^z = \rho_i^z - N_F$, is a bulk quantity. More specifically, and as shown below, it can be related to the Berry connection $\mathcal{A}_j^{m,n}(\vec{q}) = \langle \Psi_m(\vec{q}) | i\partial_{q_j} | \Psi_n(\vec{q}) \rangle$, where $|\Psi_m(\vec{q})\rangle$ denotes a Bloch wave with band index m and momentum \vec{q} .

To derive such a relation, let us imagine that the dislocation is obtained by gluing two cylinders together, see Fig. 4.1(b). Since the total charge in a system must be integer, we find that the dislocation charge (modulo 1) can be related to the edge charges of these cylinders via $Q = -Q_L - Q_R$, with $Q_{L(R)}$ the total left (right) edge charge. Both cylinders are periodic in the \vec{a}_1 direction, and thus can be viewed as a collection of 1D systems parametrized by $q_1 = j2\pi/L_1$ and $q_1 = j2\pi/(L_1 - 1)$, respectively. Hence, we may write

$$Q_L = \sum_{j=0}^{L_1-1} Q_L \left(\frac{j2\pi}{L_1} \right) \quad \text{and} \quad Q_R = \sum_{j=0}^{L_1-2} Q_R \left(\frac{j2\pi}{L_1 - 1} \right),$$

where $Q_{L(R)}(q_1)$ denotes the left (right) edge charge for a 1D insulator governed by the 1D Hamiltonian $\hat{H}_{q_1}(q_2) := \hat{H}(q_1, q_2)$. In Refs. [58, 76], it has been shown that for a 1D crystalline insulator the right (left) edge charge is given by $+(-)\gamma/(2\pi)$, with

$$\gamma = \sum_{n \leq N_F} \int_0^{2\pi} dq \langle \Psi_n(q) | i\partial_q | \Psi_n(q) \rangle.$$

Therefore, we find

$$Q_L = -\frac{1}{2\pi} \sum_{j=0}^{L_1-1} \gamma_2 \left(\frac{j2\pi}{L_1} \right) \quad \text{and} \quad Q_R = \frac{1}{2\pi} \sum_{j=0}^{L_1-2} \gamma_2 \left(\frac{j2\pi}{L_1 - 1} \right)$$

4 Dislocation charges as probes of crystalline topology

with

$$\gamma_2(q_1) = \sum_{n \leq N_F} \int_0^{2\pi} dq_2 \langle \Psi_n(q_1, q_2) | i\partial_{q_2} | \Psi_n(q_1, q_2) \rangle = \int_0^{2\pi} dq_2 \text{Tr} [\mathcal{A}_2(\vec{q})].$$

As a result, we obtain the following expression for the dislocation charge:

$$\begin{aligned} Q &= \frac{1}{2\pi} \sum_{j=0}^{L_1-1} \gamma_2\left(\frac{j2\pi}{L_1}\right) - \frac{1}{2\pi} \sum_{j=0}^{L_1-2} \gamma_2\left(\frac{j2\pi}{L_1-1}\right) \\ &= \frac{1}{2\pi} \sum_{j=0}^{L_1-1} \left[\gamma_2\left(\frac{j2\pi}{L_1}\right) - \gamma_2\left(\frac{j2\pi}{L_1-1}\right) \right] + \frac{1}{2\pi} \gamma_2(2\pi) \end{aligned}$$

To make further progress, we use that $\gamma_2(q + \delta q) - \gamma_2(q) \approx \gamma_2'(q) \delta q$. We then find:

$$\begin{aligned} Q &\approx \frac{1}{2\pi} \sum_{j=0}^{L_1-1} \gamma_2'\left(\frac{j2\pi}{L_1}\right) \frac{j2\pi}{L_1} \frac{-1}{L_1-1} + \frac{1}{2\pi} \gamma_2(2\pi) \\ &\approx -\frac{1}{(2\pi)^2} \int_0^{2\pi} dq_1 \gamma_2'(q_1) q_1 + \frac{1}{2\pi} \gamma_2(2\pi). \end{aligned}$$

In the limit, $L_1 \rightarrow \infty$ the approximations become exact. After partial integration, we find that the dislocation charge is given by

$$Q = \frac{1}{2\pi} \int_0^{2\pi} dq_1 \gamma_2(q_1) =: \frac{\gamma_2}{2\pi} \text{ modulo } 1. \quad (4.1)$$

In obtaining Eq. (4.1), we have implicitly assumed that $\gamma_2(q_1)$ depends continuously on q_1 . We like to point out, that in trivial insulators one may freely change the domain of integration to $[\phi, \phi + 2\pi]$ whereas for insulators with non-zero Chern number, C , we find that $\gamma_2 \rightarrow \gamma_2 + C\phi$. However, this should not surprise us, since a change in the domain of integration corresponds to the situation where an external magnetic flux ϕ is threading the dislocation core. This then contributes a charge $\phi/(2\pi)$ to the dislocation charge. Finally, repeating the analysis above for a dislocation with Burger's vector $\vec{B} = \vec{a}_2$ yields the general expression for the dislocation charge $Q = \vec{B}^\perp \cdot \vec{\gamma}/(2\pi)$ modulo 1, with $\vec{\gamma} = [\gamma_1 \vec{a}_1 + \gamma_2 \vec{a}_2] / \|\vec{a}_1 \times \vec{a}_2\|$.

4.1 Berry phase formulation of the dislocation charge

Let us next consider a time-reversal symmetric system with $\hat{T}^2 = -1$. Then Kramers theorem guarantees that every state is doubly degenerate. In particular, this applies to states bound to the dislocation core. Hence, in the presence of time-reversal symmetry the dislocation charge is well-defined modulo 2. To account for this, we first note that the edge charges associated with the momenta q_1 and $-q_1$ are identical, i.e. $Q_{L(R)}(q_1) = Q_{L(R)}(-q_1)$. For the moment, let us assume that L_1 is even. Then, we find that the total left edge charge is given by

$$\begin{aligned} Q_L &= 2 \sum_{j=1}^{L_1/2-1} Q_L \left(\frac{j2\pi}{L_1} \right) + Q_L(0) + Q_L(\pi) \\ &= -\frac{1}{\pi} \sum_{j=1}^{L_1/2-1} \gamma_2 \left(\frac{j2\pi}{L_1} \right) + Q_L(0) + Q_L(\pi). \end{aligned}$$

For $q_1 = 0, \pi$, we find that the 1D Hamiltonian \hat{H}_{q_1} is time-reversal symmetric. Hence, the corresponding edge charges are well-defined modulo 2, see Ref. [76] and can be expressed in terms of the partial Berry phase

$$\begin{aligned} Q_L(0) &= -Q_R(0) = -\frac{\gamma_2^I(0)}{\pi} \\ &= -\frac{1}{\pi} \left[\int_0^\pi dq_2 \operatorname{Tr} [\mathcal{A}_2(0, q_2)] + i \log \left(\frac{\operatorname{Pf} \mathcal{S}_{\hat{T}}(0, \pi)}{\operatorname{Pf} \mathcal{S}_{\hat{T}}(0, 0)} \right) \right], \end{aligned}$$

and

$$Q_L(\pi) = -\frac{\gamma_2^I(\pi)}{\pi} = -\frac{1}{\pi} \left[\int_0^\pi dq_2 \operatorname{Tr} [\mathcal{A}_2(\pi, q_2)] + i \log \left(\frac{\operatorname{Pf} \mathcal{S}_{\hat{T}}(\pi, \pi)}{\operatorname{Pf} \mathcal{S}_{\hat{T}}(\pi, 0)} \right) \right].$$

Therefore, we find that the total left and right edge charges are given by

$$Q_L = -\frac{1}{\pi} \sum_{j=1}^{L_1/2-1} \gamma_2 \left(\frac{j2\pi}{L_1} \right) - \frac{\gamma_2^I(0)}{\pi} - \frac{\gamma_2^I(\pi)}{\pi},$$

and

$$Q_R = \frac{1}{\pi} \sum_{j=1}^{L_1/2-1} \gamma_2 \left(\frac{j2\pi}{L_1 - 1} \right) + \frac{\gamma_2^I(0)}{\pi}.$$

4 Dislocation charges as probes of crystalline topology

From this it follows that the dislocation charge is given by

$$Q = \frac{1}{\pi} \sum_{j=1}^{L_1/2-1} \left[\gamma_2 \left(\frac{j2\pi}{L_1} \right) - \gamma_2 \left(\frac{j2\pi}{L_1-1} \right) \right] + \frac{\gamma_2^I(\pi)}{\pi},$$

Following the same steps as above, we find

$$\begin{aligned} Q &= \frac{1}{2\pi^2} \int_0^\pi dq_1 \gamma_2(q_1) + \frac{1}{\pi} \gamma_2^I(\pi) - \frac{1}{2\pi} \gamma_2(\pi) \\ &=: \frac{\gamma_2^I}{\pi} \text{ modulo } 2. \end{aligned} \quad (4.2)$$

For a generic dislocation we can write

$$Q = \frac{\vec{B}^\perp \cdot \vec{\gamma}^I}{\pi} \text{ modulo } 2 \quad (4.3)$$

4.2 Inversion- and rotation-symmetric insulators.

Having established the relation between the dislocation charge and the (partial) Berry phases, we now discuss the topological invariants associated to 2D crystalline insulators in the presence of inversion and/or rotational symmetries, see also Refs. [16, 70, 75, 78]. First we note that the topological invariants associated to these spatial symmetries cannot be uniquely defined. This follows from the fact that when considering inversion and rotational symmetries, one can define multiple inversion centers or rotation axes per unit-cell. For example, inversion-symmetric crystals host four inversion centers per unit-cell and threefold rotation symmetric insulators exhibit three rotation axes per unit-cell [c.f. Figs. 4.2(a) and (b)]. Let us analyze the consequences of this for inversion-symmetry, and consider the inversion operator corresponding to the inversion center A shown in Fig. 4.2(a). An electron in the \vec{i} th unit-cell and belonging to partition \mathcal{A} will be mapped to the $-\vec{i}$ th unit-cell. However, electrons belonging to partitions \mathcal{B} , \mathcal{C} , or \mathcal{D} are sent to unit cells $-\vec{i} - (1, 0)$, $-\vec{i} - (1, 1)$, or $-\vec{i} - (0, 1)$, respectively. As a consequence, we find that the Fourier transformed inversion operator is momentum dependent: $\tilde{I}_A(\vec{q}) = \text{diag} \left(\tilde{I}_A, e^{-iq_1} \tilde{I}_B, e^{-i(q_1+q_2)} \tilde{I}_C, e^{-iq_2} \tilde{I}_D \right)$. Performing a similar analysis for the other inversion centers yields that

4.2 Inversion- and rotation-symmetric insulators.

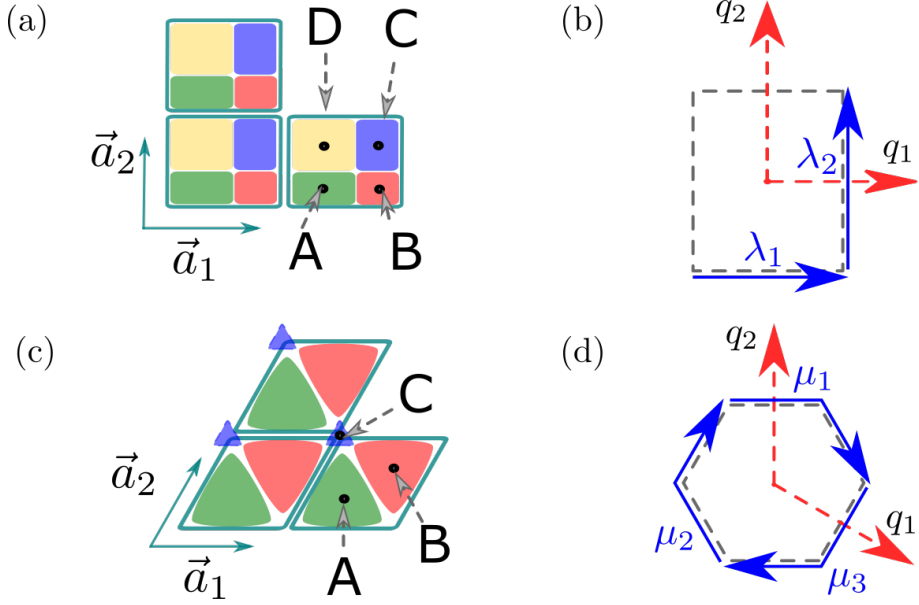


Figure 4.2: Real-space and momentum space structure of inversion and rotation-symmetric crystals. (a) Generic inversion-symmetric crystal. (b) Corresponding Brillouin zone with the two contours λ_1 and λ_2 along high-symmetry lines. (c) Generic threefold rotationally symmetric crystal. (d) Corresponding Brillouin zone, with the contours μ_1 , μ_2 and μ_3 along high-symmetry lines.

all inversion operators are equal up to \vec{q} -dependent phase factors, *i.e.* $\tilde{I}_A(\vec{q}) = e^{iq_1} \tilde{I}_B(\vec{q}) = e^{i(q_1+q_2)} \tilde{I}_C(\vec{q}) = e^{iq_2} \tilde{I}_D(\vec{q})$. Henceforth, topological invariants associated with inversion symmetry are all linked to each other. But a topological index that is coined non-trivial with respect to one inversion center, may be trivial with respect to another inversion center, and vice versa.

Such a topological index can be identified by introducing the sewing matrix $\mathcal{S}_{\tilde{I}_A}^{m,n}(\vec{q}) := \langle \Psi_m(-\vec{q}) | \tilde{I}_A(\vec{q}) | \Psi_n(\vec{q}) \rangle$, with $m, n = 1, \dots, N_F$, and where we chose the inversion center A for convenience. This matrix tracks how the occupied states at \vec{q} and $-\vec{q} = \tilde{I}_A \vec{q}$ are related by inversion symmetry. As long as the inversion operator commutes with the Hamiltonian, $\mathcal{S}_{\tilde{I}_A}$ is a unitary matrix, and one can consider the winding number of the correspond-

4 Dislocation charges as probes of crystalline topology

ing determinant along an arbitrary closed contour C : $W_C(\mathcal{S}_{\tilde{I}_A}) := \frac{i}{2\pi} \int_C d\vec{q} \cdot \nabla \log \det \mathcal{S}_{\tilde{I}_A}(\vec{q}) \in \mathbb{Z}$. For a generic contour this integer is gauge dependent since under an arbitrary gauge transformation $|\Psi_m(\vec{q})\rangle \rightarrow \mathcal{U}_{m,n}(\vec{q})|\Psi_n(\vec{q})\rangle$, we have that $W_C(\mathcal{S}_{\tilde{I}_A}) \rightarrow W_C(\mathcal{S}_{\tilde{I}_A}) + W_C(U) + W_{IC}(\mathcal{U}^*)$. For contours that change orientation under inversion, i.e. $IC = -C$, the winding number can only change by a multiple of 2, and as such it defines a \mathbb{Z}_2 invariant. Here, we have used that $W_{-C}(\mathcal{U}^*) = W_C(\mathcal{U})$. In particular, we may consider the two contours λ_1 and λ_2 , depicted in Fig. 4.2 (b). Since the integrand for the winding number is even along these contours, Therefore, we can express both \mathbb{Z}_2 -invariants in terms of the determinants at the inversion-symmetric invariant momenta

$$\xi_{i=1,2,I_A} := e^{-i\pi W_{\lambda_i}(\mathcal{S}_{\tilde{I}_A})} = \det \mathcal{S}_{\tilde{I}_A}(M) / \det \mathcal{S}_{\tilde{I}_A}(X_i).$$

Inversion symmetry therefore endows two-dimensional crystalline insulators with a $\mathbb{Z}_2 \times \mathbb{Z}_2$ topology [70]. Clearly, the same analysis can be performed for C_2 -invariant insulators, in which case the corresponding invariants can be labelled as $\xi_{1,C_{2,A}}$ and $\xi_{2,C_{2,A}}$.

The unique signature of these topological invariants does not reside in the presence of anomalous edge states but can be rather identified using their one-to-one correspondence to the Berry vector, and consequently to a generic dislocation charge. To derive such a relationship, we first rewrite γ_1 :

$$\begin{aligned} \gamma_1 &= \frac{1}{2\pi} \int_0^{2\pi} dq_2 \gamma_1(q_2) = \gamma_1(0) + \frac{1}{2\pi} \int_0^{2\pi} dq_1 \int_0^{2\pi} dq_2 \mathcal{F}_{1,2}(\vec{q}) q_2 \\ &= \gamma_1(0) + \frac{1}{2\pi} \int_{-\pi}^{\pi} dq_1 \int_{-\pi}^{\pi} dq_2 \mathcal{F}_{1,2}(\vec{q}) q_2 + \int_{-\pi}^{\pi} dq_1 \int_{-\pi}^0 dq_2 \mathcal{F}_{1,2}(\vec{q}) \\ &= \gamma_1(\pi) + \frac{1}{2\pi} \int_{-\pi}^{\pi} dq_1 \int_{-\pi}^{\pi} dq_2 \mathcal{F}_{1,2}(\vec{q}) q_2 \end{aligned} \quad (4.4)$$

The expression on the right-hand side automatically implements the continuity constraint on $\gamma_1(q_2)$. Moreover, the domain is inversion-symmetric. Therefore, we can take advantage of the fact that the sum of Berry connection at \vec{q} and $-\vec{q}$ can be expressed in terms of the sewing matrix $\mathcal{S}_{\tilde{X}_A}(\vec{q})$ with $X = \tilde{I}$ or \tilde{C}_2 and the charges in the partitions \mathcal{B} , \mathcal{C} , and \mathcal{D} , see Eq. (C.2) in Appendix C.1. Using this result we find

$$\gamma_1 = \gamma_1(\pi) - \pi [\rho_{\mathcal{B}} + \rho_{\mathcal{C}}] + \frac{1}{2} \int_{-\pi}^{\pi} dq_1 [\rho_{\mathcal{C}}(q_1, \pi) + \rho_{\mathcal{D}}(q_1, \pi)]$$

4.2 Inversion- and rotation-symmetric insulators.

We can combine the first and last term using the results from the previous Chapter. Then, we finally obtain

$$\gamma_1 = i \log(\xi_{1,X_A}) - \pi [\rho_B + \rho_C]. \quad (4.5)$$

Repeating the same steps for γ_2 , we find

$$\gamma_2 = i \log(\xi_{2,X_A}) - \pi [\rho_C + \rho_D] \quad (4.6)$$

Hence, for a generic dislocation, we find that the charge consists of two parts, one quantized to 0 or 1/2 and a second part which typically is unquantized. Observe that the charge in the \mathcal{B} , \mathcal{C} , and \mathcal{D} partitions can be independently measured in the bulk of the crystal. This proves our claim that the dislocation charge allows us to measure the crystalline topology.

In a similar fashion, one can study the electronic topology of C_3 -symmetric crystals. Then each unit-cell will host 3 rotation axes, which we label as A, B, and C, see Fig. 4.2(c). Again, we limit ourselves to rotation axis A. One can show that the winding number of the sewing matrix $\mathcal{S}_{\tilde{C}_{3,A}}$ along the contour $\mu_1 - \mu_3$, see Fig. 4.2(d), defines a \mathbb{Z}_3 invariant. To show this, we express the winding number in terms of the contours a , b , and c , shown in Fig. C.1

$$W_{\mu_1 - \mu_3}(\mathcal{S}_{C_{3,A}}) = W_{2a+b-c}(\mathcal{S}_{C_{3,A}}).$$

Next, we use that

$$\nabla_{\vec{q}} \det \mathcal{S}_{\tilde{C}_{3,A}}(\vec{q}) \mathcal{S}_{\tilde{C}_{3,A}}(R\vec{q}) \mathcal{S}_{\tilde{C}_{3,A}}(R^2\vec{q}) = 0.$$

Where, R denotes the rotation matrix corresponding to an anti-clockwise rotation of $2\pi/3$, which is given by

$$R = \begin{pmatrix} 0 & -1 \\ 1 & -1 \end{pmatrix}.$$

This yields $W_{b-c}(\mathcal{S}_{C_{3,A}}) = W_a(\mathcal{S}_{C_{3,A}})$, where we have used that $b = -Ra$ and $c = R^2a$. Hence, we find $W_{\mu_1 - \mu_3}(\mathcal{S}_{C_{3,A}}) = 3W_a(\mathcal{S}_{C_{3,A}})$. Therefore, we can express the \mathbb{Z}_3 invariant in terms of the eigenvalues at the of the rotation operator at the high-symmetry points $K^\pm = \pm(2\pi/3, 4\pi/3)$:

$$\xi_{C_{3,A}} := e^{-i\frac{2\pi}{3}W_{\mu_1 - \mu_3}(\mathcal{S}_{\tilde{C}_{3,A}})} = \det \mathcal{S}_{\tilde{C}_{3,A}}(K^+) / \det \mathcal{S}_{\tilde{C}_{3,A}}(K^-)$$

4 Dislocation charges as probes of crystalline topology

Also this invariant is directly related to the Berry vector. By using that the Berry connections at \vec{q} , $R\vec{q}$, and $R^2\vec{q}$ are related to each other via the sewing matrix, we can write

$$\begin{aligned}\gamma_1 &= i \log(\xi_{C_{3,A}}) - 2\pi[\rho_B - \rho_C]/3, \text{ and} \\ \gamma_2 &= i \log(\xi_{C_{3,A}}) - 2\pi[\rho_B + 2\rho_C]/3\end{aligned}\quad (4.7)$$

The detailed derivation is presented in Appendix C.2. In this case, we find that the topological contribution to the dislocation charge is quantized to integer multiples of $1/3$, whereas the non-topological contribution can assume any value.

4.3 Honeycomb lattice

To illustrate the results above, we consider an honeycomb lattice with a dislocation characterized by the Burgers vector $\vec{B} = \vec{a}_1$. In the lattice model, the electrons can hop between neighboring sites with a hopping parameter t , experience a staggered sub-lattice potential $\pm m$, and we include a time-reversal symmetry breaking term corresponding to chiral orbital currents [79]. In the tight-binding formulation the latter yield imaginary next-nearest neighbor hopping processes. In momentum space, the bulk Hamiltonian reads:

$$\tilde{H}(\vec{q}) = \begin{pmatrix} m + f(\vec{q}) & -t(1 + e^{-iq_1} + e^{-iq_2}) \\ -t(1 + e^{iq_1} + e^{iq_2}) & -m - f(\vec{q}) \end{pmatrix}$$

with $f(\vec{q}) = 2\lambda_H[\sin(q_1) - \sin(q_2) + \sin(q_2 - q_1)]$. We first set $m = 0$, in which case the system is inversion-symmetric, with the inversion operator given by the first Pauli matrix τ_1 . Its matrix representation is momentum independent since the unit cell is globally inversion-symmetric. At half-filling we find $\xi_{1,I_A} = \xi_{2,I_A} = -1$ and hence for the dislocation depicted in Fig. 4.3(a), Eq. (4.6) predicts a dislocation charge $Q = 1/2$. We have numerically verified this result by computing the local charge around the dislocation as indicated in Fig. 4.3. We have also analyzed the effect of the inversion-symmetry breaking term reducing the crystal symmetry to C_3 . The rotation operator has the matrix representation $\tilde{C}_{3,A}(\vec{q}) = \text{diag}(1, e^{-iq_2})$,

4.3 Honeycomb lattice

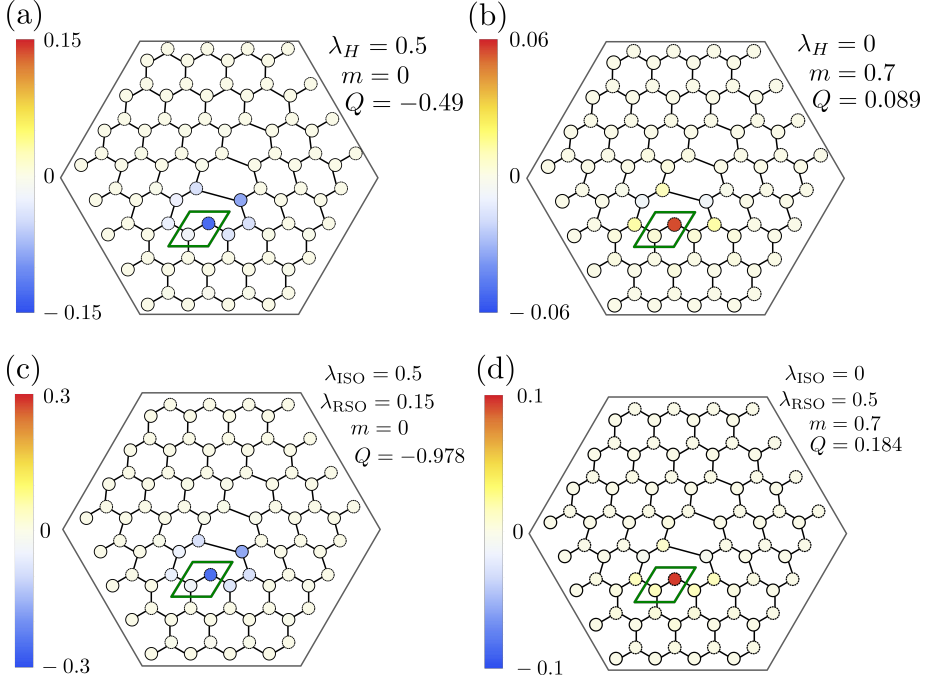


Figure 4.3: Edge dislocation with Burgers vector $\vec{B} = \vec{a}_1$. The color quantifies the charge local charge deviation. The inset depicts the parameters that have been used, and Q corresponds to the sum of the charge deviations within the hexagon. The upper-panels corresponds to a spinless honeycomb lattice, whereas the lower panels include spin-orbit coupling terms.

and acquires a momentum dependence since the unit-cell is not rotation-symmetric. At half-filling the \mathbb{Z}_3 invariant is given by

$$\xi_{C_{3,A}} = \begin{cases} 1 & \text{if } m < -3\sqrt{3}|\lambda_H| \\ e^{i2\pi/3} & \text{if } -3\sqrt{3}|\lambda_H| < m < 3\sqrt{3}|\lambda_H| \\ e^{-i2\pi/3} & \text{if } m > 3\sqrt{3}|\lambda_H| \end{cases}$$

Let us analyze the case $\lambda_H = 0$ and $m = 0.7t$. We have numerically calculated the charge in the \mathcal{B} partition, which is given by $\rho_B = 0.73$. Hence, using Eqs. (4.1) and (4.7) we predict $Q = 1/3 - 0.73/3 = 0.09$, which is in perfect agreement with the result shown in Fig. 4.3(b).

4.4 Time-reversal symmetry

In time-reversal symmetric systems, Kramer's theorem guarantees that inversion- and C_2 -symmetric crystals cannot be characterized topologically by the $\mathbb{Z}_2 \times \mathbb{Z}_2$ invariant introduced above. This follows from the fact that at the time-reversal invariant momenta the determinant of the sewing matrices is always 1. But, this does not preclude the existence of a different topological invariant. In particular, we may consider the winding number of the determinants over half the contour $\lambda_{1(2)}$, i.e. from $X_{2(1)}$ to M . In general, this winding number is gauge-variant. However, if we impose a time-reversal symmetric gauge along these contours, then both yield a \mathbb{Z}_2 -invariant see also Ref. [76]. We denote this winding number with $W_{\lambda_i}^{1/2}(\mathcal{S}_{\tilde{X}_A})$, with $X = I$ or C_2 . In inversion-symmetric insulators, we can simply express this invariant in terms of the eigenvalues of the inversion-operator for half of the Kramers partners:

$$\chi_{i,\tilde{I}_A} = e^{-i\pi W_{\lambda_i}^{1/2}(\mathcal{S}_{\tilde{I}_A})} = \det \mathcal{S}_{\tilde{I}_A}^I(M) / \mathcal{S}_{\tilde{I}_A}^I(X_i)$$

Here, \mathcal{S}^I denotes the restriction of the sewing matrix to a single time-reversed "channel". For C_2 -symmetric insulators, instead, such a simple expression does not exist. This difference stems from the fact that $(\hat{I}\hat{T})^2 = -1$ and $(\hat{C}_2\hat{T})^2 = 1$. The invariant χ_{i,X_A} with $X = I$ or C_2 can be directly related to the partial Berry phase γ_1^I . We express the partial Berry phase in terms of the Berry curvature, i.e.

$$\begin{aligned} \gamma_1^I &= \frac{1}{2\pi} \int_0^\pi dq_2 \gamma_1(q_2) + \gamma_1^I(\pi) - \gamma_1(\pi) \\ &= \frac{1}{2\pi} \int_0^{2\pi} dq_1 \int_0^\pi dq_2 \mathcal{F}_{1,2}(\vec{q}) q_2 + \gamma_1^I(\pi) \\ &= \frac{1}{4\pi} \int_{-\pi}^\pi dq_1 \int_{-\pi}^\pi dq_2 \mathcal{F}_{1,2}(\vec{q}) q_2 + \gamma_1^I(\pi), \end{aligned}$$

where in the final equality we have used that $\mathcal{F}_{1,2}(\vec{q}) = -\mathcal{F}_{1,2}(-\vec{q})$ in the presence of time-reversal symmetry. Making use of Eq. (C.2) we obtain

$$\begin{aligned} \gamma_1^I &= -\frac{\pi}{2} [\rho_B + \rho_C] + \frac{1}{4} \int_0^{2\pi} dq_1 [\rho_C(q_1, \pi) + \rho_D(q_1, \pi)] + \gamma_1^I(\pi) \\ &= i \log(\chi_{1,X_A}) - \frac{\pi}{2} [\rho_B + \rho_C]. \end{aligned} \tag{4.8}$$

4.5 Spinful honeycomb lattice

The final equality is derived in the previous Chapter. Repeating the same steps for γ_2^I , we find

$$\gamma_2^I = i \log(\chi_{2, \tilde{X}_A}) - \pi[\rho_C + \rho_D]/2. \quad (4.9)$$

The \mathbb{Z}_3 -topology does not suffer the same fate in the presence time-reversal symmetry, for the very simple fact that $1 + 1 \neq 0$ modulo 3. Since K^+ and K^- are related by time-reversal symmetry, it follows that we can simplify the expression for ξ_{C_3} , by writing

$$\xi_{C_{3,A}} = \det \mathcal{S}_{\tilde{C}_{3,A}} (K^+)^2 =: \chi_{C_{3,A}}^2.$$

On the right-hand side we have introduced the invariant $\chi_{C_{3,A}}$. Although this invariant does not encode any new information, it is $\chi_{C_{3,A}}$ that is directly related to the partial Berry phase. The contours μ_i are all time-reversal symmetric. Again, we impose a time-reversal symmetric gauge and compute the winding numbers $W_{\mu_1}^{1/2}$ and $W_{\mu_3}^{1/2}$, over half these contours, from X_2 to M , and from X_1 to M , respectively. Then it follows, see Appendix C.3 for a derivation, that the winding number $W_{\mu_1 - \mu_3}^{1/2}(\mathcal{S}_{\tilde{C}_{3,A}})$ can be related to $\chi_{C_{3,A}}$ as

$$W_{\mu_1 - \mu_3}^{1/2}(\mathcal{S}_{\tilde{C}_{3,A}}) = \frac{3}{2\pi} i \log(\chi_{C_{3,A}}).$$

This allows us to express the partial Berry vector solely in terms of $\chi_{C_{3,A}}$, ρ_B , and ρ_C :

$$\begin{aligned} \gamma_1^I &= i \log(\chi_{C_{3,A}}) - \pi[\rho_B - \rho_C]/3 \text{ and} \\ \gamma_2^I &= i \log(\chi_{C_{3,A}}) - \pi[\rho_B + 2\rho_C]/3. \end{aligned} \quad (4.10)$$

See Appendix C.4 for a detailed derivation.

4.5 Spinful honeycomb lattice

To demonstrate these results we consider a time-reversal symmetric honeycomb lattice model for spin-one-half fermions, where we include both intrinsic and Rashba spin-orbit coupling. The latter corresponds to nearest-

4 Dislocation charges as probes of crystalline topology

neighbor hoppings that flip the spin and reads

$$\begin{aligned}\tilde{H}_{\text{RSO}}(\vec{q}) &= i\lambda_{\text{RSO}} \begin{pmatrix} 0 & 1 \\ -1 & 0 \end{pmatrix} \otimes \left(\frac{\sqrt{3}}{2}\sigma_2 + \frac{1}{2}\sigma_1 \right) \\ &+ i\lambda_{\text{RSO}} \begin{pmatrix} 0 & e^{-iq_1} \\ -e^{iq_1} & 0 \end{pmatrix} \otimes \left(-\frac{\sqrt{3}}{2}\sigma_2 + \frac{1}{2}\sigma_1 \right) \\ &- i\lambda_{\text{RSO}} \begin{pmatrix} 0 & e^{-iq_2} \\ -e^{iq_2} & 0 \end{pmatrix} \otimes \sigma_1.\end{aligned}$$

The former leads to spin-dependent chiral orbital currents and is given by

$$\tilde{H}_{\text{ISO}}(\vec{q}) = \lambda_{\text{ISO}} f(\vec{q}) \begin{pmatrix} 1 & 0 \\ 0 & -1 \end{pmatrix} \otimes \sigma_3.$$

It is easily verified that both terms respect the C_3 and C_2 -symmetry. The corresponding symmetry operators read:

$$\tilde{C}_{2,A}(\vec{q}) = \tau_1 \otimes i\sigma_3 \text{ and } \tilde{C}_{3,A}(\vec{q}) = \text{diag}(1, e^{-iq_2}) \otimes e^{i\frac{\pi\sigma_3}{3}}.$$

For the example depicted in Fig. 4.3(c) we find $\chi_{1,C_{2,A}} = \chi_{2,C_{2,A}} = -1$, which yields $Q = 1$ modulo 2. This result is numerically confirmed. In Fig. 4.3(d) we have depicted a spinful C_3 -symmetric crystal. Using these parameters we find $\chi_{C_{3,A}} = e^{-i2\pi/3}$. Moreover, we find that $\rho_B = 1.44$. Therefore, we predict $Q = 2/3 - \rho_B/3 = 0.187$. Again, this is in perfect agreement with the result shown in Fig. 4.3(d).

4.6 Conclusion

To conclude, we have shown that the fractional part of the dislocation charge is a bulk property that can be linked to the Berry phase. In time-reversal symmetric systems, one can link the dislocation charge to the partial Berry phase, and microscopic details can only change the charge by multiples of 2. Finally, we have shown that in inversion- and n-fold symmetric insulators, one can express the (partial) Berry phases in terms of crystalline invariants. Therefore, we believe that dislocations are ideally suited to probe this topology. In particular, we note that one can even probe this topology in Chern insulators and time-reversal symmetric topological insulators.

C

C.1 Useful identities

Here, we state important identities. Let I denote the inversion matrix, i.e. $I\vec{q} = -\vec{q}$. Then we find that for inversion-symmetric system the following identity holds:

$$|\Psi_m(I\vec{q})\rangle = \sum_{n \leq N_F} \mathcal{S}_{\tilde{I}_A}^\dagger(\vec{q})^{m,n} \tilde{I}_A(\vec{q}) |\Psi_n(\vec{q})\rangle,$$

and

$$\langle \Psi_m(I\vec{q}) | = \sum_{n \leq N_F} \langle \Psi_n(\vec{q}) | \tilde{I}_A^\dagger(\vec{q}) \mathcal{S}_{\tilde{I}_A}(\vec{q})^{n,m}.$$

Let R denote the rotation matrix corresponding to an anti-clockwise rotation of $2\pi/3$. Then, for C_3 -symmetric systems we find

$$|\Psi_m(R\vec{q})\rangle = \sum_{n \leq N_F} \mathcal{S}_{\tilde{C}_{3,A}}^\dagger(\vec{q})^{m,n} \tilde{C}_{3,A}(\vec{q}) |\Psi_n(\vec{q})\rangle,$$

and

$$\langle \Psi_m(R\vec{q}) | = \sum_{n \leq N_F} \langle \Psi_n(\vec{q}) | \tilde{C}_{3,A}^\dagger(\vec{q}) \mathcal{S}_{\tilde{C}_{3,A}}(\vec{q})^{n,m}.$$

As stated in the main text, we find that the inversion (two-fold rotation operator) generically is given by

$$\tilde{I}_A(\vec{q}) = \begin{pmatrix} \tilde{I}_A & 0 & 0 & 0 \\ 0 & \tilde{I}_B e^{-iq_1} & 0 & 0 \\ 0 & 0 & \tilde{I}_C e^{-i(q_1+q_2)} & 0 \\ 0 & 0 & 0 & \tilde{I}_D e^{-iq_2} \end{pmatrix}$$

C

and for C_3 -symmetric systems we obtain

$$\tilde{C}_{3,A}(\vec{q}) = \begin{pmatrix} \tilde{C}_{3,A} & 0 & 0 \\ 0 & \tilde{C}_{3,B}e^{-iq_2} & 0 \\ 0 & 0 & \tilde{C}_{3,C}e^{i(q_1-q_2)} \end{pmatrix}$$

As a result, we find

$$\tilde{I}_A(\vec{q})^\dagger i\partial_1 \tilde{I}_A(\vec{q}) = \begin{pmatrix} 0 & 0 & 0 & 0 \\ 0 & 1 & 0 & 0 \\ 0 & 0 & 1 & 0 \\ 0 & 0 & 0 & 0 \end{pmatrix} \quad \text{and} \quad \tilde{I}_A(\vec{q})^\dagger i\partial_2 \tilde{I}_A(\vec{q}) = \begin{pmatrix} 0 & 0 & 0 & 0 \\ 0 & 0 & 0 & 0 \\ 0 & 0 & 1 & 0 \\ 0 & 0 & 0 & 1 \end{pmatrix}.$$

and

$$\tilde{C}_{3,A}(\vec{q})^\dagger i\partial_1 \tilde{C}_{3,A}(\vec{q}) = \begin{pmatrix} 0 & 0 & 0 \\ 0 & 0 & 0 \\ 0 & 0 & -1 \end{pmatrix} \quad \text{and} \quad \tilde{C}_{3,A}(\vec{q})^\dagger i\partial_2 \tilde{C}_{3,A}(\vec{q}) = \begin{pmatrix} 0 & 0 & 0 \\ 0 & 1 & 0 \\ 0 & 0 & 1 \end{pmatrix}.$$

The identities allow us to relate the Berry connections at \vec{q} and $I\vec{q}$ through

$$\text{Tr} [\mathcal{A}(I\vec{q})] = I^T \left[\text{Tr} [\mathcal{A}(\vec{q})] + \vec{\rho}(\vec{q}) + i\nabla_{\vec{q}} \log \left(\det \mathcal{S}_{I_A}^\dagger(\vec{q}) \right) \right] \quad (\text{C.1})$$

with $\vec{\rho}(\vec{q}) = (\rho_B(\vec{q}) + \rho_C(\vec{q}), \rho_C(\vec{q}) + \rho_D(\vec{q}))$. In addition we find that the Berry curvature satisfy

$$\mathcal{F}_{1,2}(I\vec{q}) = \mathcal{F}_{1,2}(\vec{q}) + \nabla \times \vec{\rho}(\vec{q}). \quad (\text{C.2})$$

For C_3 -symmetric systems we find

$$\text{Tr} [\mathcal{A}(R\vec{q})] = (R^T)^2 \left[\text{Tr} [\mathcal{A}(\vec{q})] + \vec{\rho}(\vec{q}) + i\nabla_{\vec{q}} \log \left(\det \mathcal{S}_{\tilde{C}_{3,A}}^\dagger(\vec{q}) \right) \right], \quad (\text{C.3})$$

with $\vec{\rho}(\vec{q}) = (-\rho_C(\vec{q}), \rho_B(\vec{q}) + \rho_C(\vec{q}))$. Which implies the following identity:

$$\mathcal{F}_{1,2}(R\vec{q}) = \mathcal{F}_{1,2}(\vec{q}) + \nabla \times \vec{\rho}(\vec{q}). \quad (\text{C.4})$$

C.2 Derivation of Eq. (4.7)

In this section, we express γ_1 and γ_2 in terms of the invariant $\xi_{C_{3,A}}$. First, we will relate the integral of the Berry connection along the contour μ_1 to $\xi_{C_{3,A}}$. Making use of Eq. (C.3), we find

$$\begin{aligned}\gamma_{\mu_{i+1}} &= \int_{\mu_i} d(R\vec{q}) \cdot \text{Tr} [\mathcal{A}(R\vec{q})] \\ &= \int_{\mu_i} d\vec{q} \cdot \text{Tr} [\mathcal{A}(\vec{q}) + i \int_{\mu_i} d\vec{q} \cdot \nabla_{\vec{q}} \log (\det \mathcal{S}_{C_{3,A}}^\dagger(\vec{q})) + \int_{\mu_i} d\vec{q} \cdot \vec{\rho}(\vec{q})] \\ &= \gamma_{\mu_i} - 2\pi W_{\mu_i} (\mathcal{S}_{C_{3,A}}) + \int_{\mu_i} d\vec{q} \cdot \vec{\rho}(\vec{q})\end{aligned}$$

As a result, we then obtain

$$\gamma_{\mu_1} = \frac{1}{3}[\gamma_{\mu_1} + \gamma_{\mu_2} + 2\pi W_{\mu_1} (\mathcal{S}_{C_{3,A}}) - \int_{\mu_1} d\vec{q} \cdot \vec{\rho}(\vec{q}) + \gamma_{\mu_3}] \quad (\text{C.5})$$

$$\begin{aligned}&- 2\pi W_{\mu_3} (\mathcal{S}_{C_{3,A}}) + \int_{\mu_3} d\vec{q} \cdot \vec{\rho}(\vec{q})] \\ &= \frac{2\pi}{3} W_{\mu_1 - \mu_3} (\mathcal{S}_{C_{3,A}}) - \frac{1}{3} \int_{\mu_1 - \mu_3} d\vec{q} \cdot \vec{\rho}(\vec{q})\end{aligned} \quad (\text{C.6})$$

$$= i \log \xi_{C_{3,A}} - \frac{1}{3} \int_{\mu_1 - \mu_3} d\vec{q} \cdot \vec{\rho}(\vec{q}) \quad (\text{C.7})$$

Next, let us turn to the expression for γ_1 , Eq. (4.4):

$$\gamma_1 = \gamma_1(\pi) + \frac{1}{2\pi} \int_{-\pi}^{\pi} dq_1 \int_{-\pi}^{\pi} dq_2 \mathcal{F}_{1,2}(\vec{q}) q_2$$

To exploit the rotational symmetry, we will change the domain of integration in the second term. For this purpose we divide the domain $[-\pi, \pi] \times [-\pi, \pi]$ into five parts, see Fig. C.1, labeled as I, II, III, IV , and V , i.e.

$$BZ := [-\pi, \pi] \times [-\pi, \pi] = I \cup II \cup III \cup IV \cup V.$$

We wish to express the integral over BZ as an integral over the symmetric domain \overline{BZ} , see Fig. 4, consisting of $\overline{I}, \overline{II}, \overline{III}, \overline{IV}$, and V , i.e.

$$\overline{BZ} := \overline{I} \cup \overline{II} \cup \overline{III} \cup \overline{IV} \cup V.$$

C

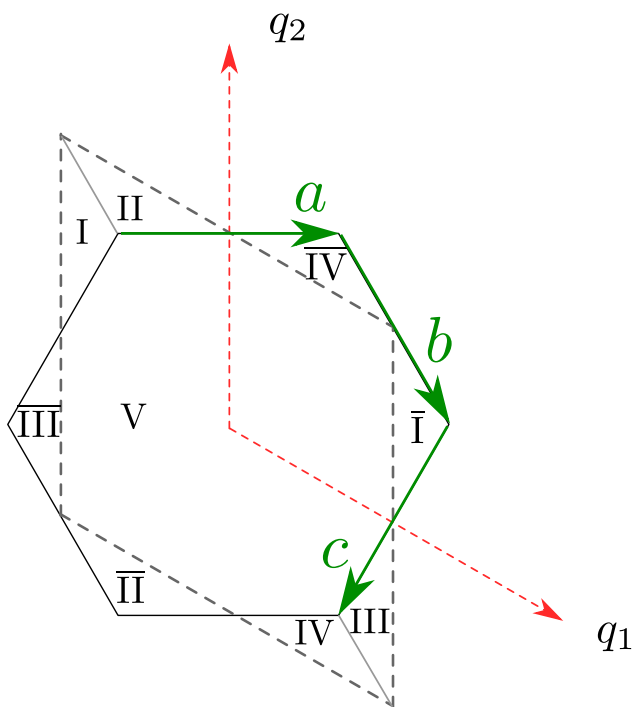


Figure C.1: The dashed lines enclose the domain $BZ = [-\pi, \pi] \times [-\pi, \pi]$. The green arrows denote the contours a , b , and c .

Using this notation, we can write

$$\begin{aligned}
 \gamma_1 &= \gamma_1(\pi) + \frac{1}{2\pi} \int_{\overline{BZ}} d\vec{q} \mathcal{F}_{1,2}(\vec{q}) q_2 + \int_{\overline{II-IV}} d\vec{q} \mathcal{F}_{1,2}(\vec{q}) \\
 &= \gamma_{\mu_1} + \frac{1}{2\pi} \int_{\overline{BZ}} d\vec{q} \mathcal{F}_{1,2}(\vec{q}) q_2.
 \end{aligned} \tag{C.8}$$

In the second equality we have employed Stokes' theorem. To make further progress, we need to specify the integration bounds explicitly. Here, we use the following parametrization:

$$\int_{\overline{BZ}} dq_1 dq_2 = \int_{-4\pi/3}^{4\pi/3} dq_1 \int_{b^-(q_1)}^{b^+(q_1)} dq_2,$$

with $b^+(q_1)$ given by

$$b^+(q_1) = \begin{cases} 2q_1 + 2\pi & \text{if } -\frac{4\pi}{3} \leq q_1 \leq -\frac{2\pi}{3} \\ \frac{1}{2}q_1 + \pi & \text{if } -\frac{2\pi}{3} \leq q_1 \leq \frac{2\pi}{3} \\ -q_1 + 2\pi & \text{if } \frac{2\pi}{3} \leq q_1 \leq \frac{4\pi}{3} \end{cases}$$

and $b^-(q_1)$ given by

$$b^-(q_1) = \begin{cases} -q_1 - 2\pi & \text{if } -\frac{4\pi}{3} \leq q_1 \leq -\frac{2\pi}{3} \\ \frac{1}{2}q_1 - \pi & \text{if } -\frac{2\pi}{3} \leq q_1 \leq \frac{2\pi}{3} \\ 2q_1 - 2\pi & \text{if } \frac{2\pi}{3} \leq q_1 \leq \frac{4\pi}{3} \end{cases}$$

Note that b^+ is related to b^- in the following way

$$b^+(q_1) = \begin{cases} b^-(q_1 + 2\pi) & \text{if } -\frac{4\pi}{3} \leq q_1 \leq -\frac{2\pi}{3} \\ b^-(q_1) + 2\pi & \text{if } -\frac{2\pi}{3} \leq q_1 \leq \frac{2\pi}{3} \\ b^-(q_1 - 2\pi) + 2\pi & \text{if } \frac{2\pi}{3} \leq q_1 \leq \frac{4\pi}{3} \end{cases} \tag{C.9}$$

C

With the help of Eq. (C.4), we can express the second term in Eq. (C.8) as

$$\begin{aligned}
\int_{\overline{BZ}} \mathcal{F}_{1,2}(\vec{q}) q_2 &= \frac{1}{3} \int_{\overline{BZ}} dq [\mathcal{F}_{1,2}(\vec{q}) + \mathcal{F}_{1,2}(R\vec{q}) + \mathcal{F}_{1,2}(R^2\vec{q})] q_2 \\
&\quad - \frac{1}{3} \int dq_1 \int dq_2 (\partial_{q_1} \rho_2(\vec{q}) - \partial_{q_2} \rho_1(\vec{q})) q_2 \\
&\quad - \frac{1}{3} \int dq_1 \int dq_2 (-\partial_{q_2} \rho_2(\vec{q}) - \partial_{q_1} \rho_1(\vec{q}) - \partial_{q_2} \rho_1(\vec{q})) q_2 \\
&= -\frac{1}{3} \underbrace{\int_{-4\pi/3}^{4\pi/3} dq_1 \int_{b^-(q_1)}^{b^+(q_1)} dq_2 [\partial_{q_1} \rho_2(\vec{q})] q_2}_{\text{(C.10)a}} \\
&\quad + \frac{2}{3} \underbrace{\int_{-4\pi/3}^{4\pi/3} dq_1 \int_{b^-(q_1)}^{b^+(q_1)} dq_2 [\partial_{q_2} \rho_1(\vec{q})] q_2}_{\text{(C.10)b}} \\
&\quad + \frac{1}{3} \underbrace{\int_{-4\pi/3}^{4\pi/3} dq_1 \int_{b^-(q_1)}^{b^+(q_1)} dq_2 [\partial_{q_1} \rho_1(\vec{q})] q_2}_{\text{(C.10)c}} \\
&\quad + \frac{1}{3} \underbrace{\int dq_1 \int dq_2 [\partial_{q_2} \rho_2(\vec{q})] q_2}_{\text{(C.10)d}} \tag{C.10}
\end{aligned}$$

Let us now work out the terms on the RHS of the equation above. Let us start with the first term. We move the derivative in front of the integral over q_2 :

$$\begin{aligned}
\text{(C.10)a} &= -\frac{1}{3} \int_{-4\pi/3}^{4\pi/3} dq_1 \partial_{q_1} \int_{b^-(q_1)}^{b^+(q_1)} dq_2 \rho_2(\vec{q}) q_2 \\
&\quad + \frac{1}{3} \int_{-4\pi/3}^{4\pi/3} dq_1 b^+(q_1) \rho_2(q_1, b^+(q_1)) \partial_{q_1} b^+(q_1) \\
&\quad - \frac{1}{3} \int_{-4\pi/3}^{4\pi/3} dq_1 b^-(q_1) \rho_2(q_1, b^-(q_1)) \partial_{q_1} b^-(q_1)
\end{aligned}$$

C.2 Derivation of Eq. (4.7)

The first term on the RHS vanishes because $b^+(\pm 4\pi/3) = b^-(\pm 4\pi/3)$. With the help of Eq. (C.9), we can combine the second and third term:

$$\begin{aligned} \frac{1}{6} \int_{-2\pi/3}^{2\pi/3} dq_1 \rho_2(q_1, b^+(q_1)) \cdot 2\pi + \frac{2}{3} \int_{-4\pi/3}^{-2\pi/3} dq_1 \rho_2(q_1, b^+(q_1)) \cdot 0 \\ - \frac{1}{3} \int_{2\pi/3}^{4\pi/3} dq_1 \rho_2(q_1, b^+(q_1)) \cdot 2\pi = 0. \end{aligned}$$

In the equation above the first and third term cancel against each other. Next, we consider the second term on the RHS of Eq. (C.10). Upon integration by parts, we find

$$\begin{aligned} \text{(C.10)b} &= -\frac{2}{3} \int dq_1 \int dq_2 \rho_1(\vec{q}) \\ &= \frac{2}{3} \int_{-4\pi/3}^{4\pi/3} dq_1 [b^+(q_1) \rho_1(q_1, b^+(q_1)) - b^-(q_1) \rho_1(q_1, b^-(q_1))] \\ &= -\frac{2}{3} \int dq_1 \int dq_2 \rho_1(\vec{q}) + \frac{4\pi}{3} \int_{-2\pi/3}^{4\pi/3} dq_1 \rho_1(q_1, b^+(q_1)) \\ &= -\frac{8\pi^2}{3} \rho_1 + \frac{4\pi}{3} \int_{-2\pi/3}^{4\pi/3} dq_1 \rho_1(q_1, b^+(q_1)). \end{aligned}$$

The third term vanishes for the same reason as the first term:

$$\begin{aligned} \text{(C.10)c} &= \frac{1}{3} \int_{-4\pi/3}^{4\pi/3} dq_1 \partial_{q_1} \int_{b^-(q_1)}^{b^+(q_1)} dq_2 \rho_1(\vec{q}) q_2 \\ &\quad - \frac{1}{3} \int_{-4\pi/3}^{4\pi/3} dq_1 b^+(q_1) \partial_{q_1} b^+(q_1) \rho_1(q_1, b^+(q_1)) \\ &\quad - \frac{1}{3} \int_{-4\pi/3}^{4\pi/3} dq_1 b^-(q_1) \partial_{q_1} b^-(q_1) \rho_1(q_1, b^-(q_1)) \\ &= 0 \end{aligned}$$

C

Finally, let us rewrite the fourth term:

$$\begin{aligned}
\text{(C.10)d} &= -\frac{1}{3} \int dq_1 \int dq_2 \rho_2(\vec{q}) \\
&\quad + \frac{1}{3} \int_{-4\pi/3}^{4\pi/3} dq_1 [b^+(q_1) \rho_2(q_1, b^+(q_1)) - b^-(q_1) \rho_2(q_1, b^-(q_1))] \\
&= -\frac{1}{3} \int dq_1 \int dq_2 \rho_2(\vec{q}) + \frac{2\pi}{3} \int_{-2\pi/3}^{4\pi/3} dq_1 \rho_2(q_1, b^+(q_1)) \\
&= -\frac{4\pi^2}{3} \rho_2 + \frac{2\pi}{3} \int_{-2\pi/3}^{4\pi/3} dq_1 \rho_2(q_1, b^+(q_1))
\end{aligned}$$

Hence, if we now combine Eqs. (C.5), (C.8), and (C.10) we find

$$\begin{aligned}
\gamma_1 &= i \log \xi_{C_{3,A}} - \frac{1}{3} \int_{\mu_1 - \mu_3} d\vec{q} \cdot \vec{\rho}(\vec{q}) - \frac{4\pi}{3} \rho_1 + \frac{2\pi}{3} \rho_2 \\
&\quad + \frac{1}{3} \int_{-2\pi/3}^{4\pi/3} dq_1 \rho_2(q_1, b^+(q_1)) + \frac{2}{3} \int_{-2\pi/3}^{4\pi/3} dq_1 \rho_1(q_1, b^+(q_1)) \\
&= i \log \xi_{C_{3,A}} - \frac{4\pi}{3} \rho_1 - \frac{2\pi}{3} \rho_2 = i \log \xi_{C_{3,A}} - \frac{2\pi}{3} \rho_B + \frac{2\pi}{3} \rho_C
\end{aligned}$$

Here, we have used that the second term cancels the last two integrals. Following the same steps for γ_2 , we obtain

$$\gamma_2 = i \log \xi_{C_{3,A}} + \frac{2\pi}{3} \rho_1 - \frac{2\pi}{3} \rho_2 = i \log \xi_{C_{3,A}} - \frac{2\pi}{3} \rho_B - \frac{4\pi}{3} \rho_C$$

C.3 Relation $W_{\mu_1 - \mu_3}^{1/2}(\mathcal{S}_{C_{3,A}})$ and $\det(\mathcal{S}_{\tilde{C}_{3,A}}(K^+))$

Let us relate $W_{\mu_1 - \mu_3}^{1/2}(\mathcal{S}_{C_{3,A}})$ to the determinant of the sewing matrix at $\vec{q} = K^+$. For this purpose, we write:

$$W_{\mu_1 - \mu_3}^{1/2}(\mathcal{S}_{C_{3,A}}) = W_{2a+b-c}^{1/2}(\mathcal{S}_{C_{3,A}}).$$

Then it follows that

$$\begin{aligned}
W_{\mu_1 - \mu_3}^{1/2}(\mathcal{S}_{C_{3,A}}) &= 3W_a^{1/2}(\mathcal{S}_{C_{3,A}}) \\
&= i \frac{3}{2\pi} \log \det(\mathcal{S}_{\tilde{C}_{3,A}}(K^+)) / \det(\mathcal{S}_{\tilde{C}_{3,A}}(0, \pi)) \\
&= i \frac{3}{2\pi} \log \det(\mathcal{S}_{\tilde{C}_{3,A}}(K^+)).
\end{aligned}$$

In the final equality we have made use of the fact that the determinant is identically equal to 1 at momenta that are time-reversal symmetric.

C.4 Derivation of Eq. (4.10)

First, let us relate the partial Berry phase along the contour μ_1 to the \mathbb{Z}_3 -invariant $\chi_{C_{3,A}}$. For the purpose of the proof, we assume that we have found a time-reversal symmetric gauge along the contours μ_i . Then we can write

$$\begin{aligned}\gamma_{\mu_{i+1}}^I &= \int_{\mu_i^{1/2}} dR\vec{q} \cdot \text{Tr} [\mathcal{A}(R\vec{q})] \\ &= \int_{\mu_i^{1/2}} d\vec{q} \cdot \text{Tr} [\mathcal{A}(\vec{q})] + i \int_{\mu_i^{1/2}} d\vec{q} \cdot \nabla_{\vec{q}} \log \det \mathcal{S}_{\tilde{C}_{3,A}}^\dagger(\vec{q}) + \int_{\mu_i^{1/2}} d\vec{q} \cdot \vec{\rho}(\vec{q}) \\ &= \gamma_{\mu_i}^I - 2\pi W_{\mu_i}^{1/2}(\mathcal{S}_{\tilde{C}_{3,A}}) + \int_{\mu_i^{1/2}} d\vec{q} \cdot \vec{\rho}(\vec{q}).\end{aligned}$$

This implies:

$$\begin{aligned}\gamma_{\mu_1}^I &= \frac{2\pi}{3} W_{\mu_1 - \mu_3}^{1/2}(\mathcal{S}_{\tilde{C}_{3,A}}) - \frac{1}{3} \int_{\mu_1^{1/2} + \mu_3^{1/2}} d\vec{q} \cdot \vec{\rho}(\vec{q}) \\ &= i \log \chi_{C_{3,A}} - \frac{1}{3} \int_{\mu_1^{1/2} - \mu_3^{1/2}} d\vec{q} \cdot \vec{\rho}(\vec{q}) \\ &= i \log \chi_{C_{3,A}} - \frac{1}{6} \int_{\mu_1 - \mu_3} d\vec{q} \cdot \vec{\rho}(\vec{q})\end{aligned}\tag{C.11}$$

Now, let us consider γ_1^I . First, we express γ_1^I as an integral over the rotation-symmetric domain \overline{BZ}

$$\begin{aligned}\gamma_1^I &= \gamma_1^I(\pi) + \frac{1}{4\pi} \int_{-\pi}^{\pi} dq_1 \int_{-\pi}^{\pi} dq_2 \mathcal{F}_{1,2}(\vec{q}) q_2 \\ &= \gamma_1^I(\pi) + \frac{1}{2} \int_{\overline{II-IV}} d\vec{q} \mathcal{F}_{1,2}(\vec{q}) + \frac{1}{4\pi} \int_{\overline{BZ}} d\vec{q} \mathcal{F}_{1,2}(\vec{q}) q_2 \\ &= \gamma_1^I(\pi) + \int_{\overline{II}} d\vec{q} \mathcal{F}_{1,2}(\vec{q}) + \frac{1}{4\pi} \int_{\overline{BZ}} d\vec{q} \mathcal{F}_{1,2}(\vec{q}) q_2 \\ &= \gamma_{\mu_1}^I + \frac{1}{4\pi} \int_{\overline{BZ}} d\vec{q} \mathcal{F}_{1,2}(\vec{q}) q_2.\end{aligned}$$

C

In the third equality we have used that $\mathcal{F}_{1,2}(\vec{q}) = -\mathcal{F}_{1,2}(-\vec{q})$, and in the fourth equality we have employed Stokes theorem. Using Eqs. (C.10) and (C.11) we finally obtain

$$\gamma_1^I = i \log(\chi_{C_{3,A}}) - \frac{\pi}{3} \rho_B + \frac{\pi}{3} \rho_C.$$

In a similar fashion we find

$$\gamma_2^I = i \log(\chi_{C_{3,A}}) - \frac{\pi}{3} \rho_B - \frac{2\pi}{3} \rho_C.$$

5 Dirac cones beyond the honeycomb lattice: a symmetry-based approach

The synthesis of graphene has opened the world of Dirac cones and the physics that derives from them [80]. Since then, Dirac systems have attracted a huge interest not only from a fundamental point of view, but also with a view on applications. Indeed, graphene holds promises to revolutionize nanotechnology because it is ultrathin, light, transparent, and resilient to bending. Current applications range from sensors to transparent flexible electronics, field-effect devices, and spintronics. In addition, many phenomena first discussed in the realm of elementary-particle physics now find their way to tabletop experiments. Examples include the Klein paradox, Zitterbewegung, and connections to gravity [81]. Moreover, Dirac fermions have been of great importance to the field of topological quantum matter. Firstly, experiments at very high magnetic fields revealed that in graphene the quantum Hall effect may be observed at room-temperature [82]. Secondly, graphene is the system for which the quantum spin Hall effect was originally proposed [9].

During the first decade after the initial synthesis of graphene, the field of Dirac materials has evolved into various directions. One of these focuses on graphene's honeycomb lattice, and is concerned whether one can obtain different or more versatile materials by replacing the carbon atoms by different group IV elements [83]. This pursuit led to the successful synthesis of silicene, germanene, and stanene [84–86]. Since these atoms have a larger atomic radius than carbon, they buckle out of the two-dimensional plane and this buckling is useful for applications in electronic devices. In particular, one can generate a mass for the Dirac fermions in silicene by the application of an external electric field, which is exploited in field-effect transistors [87]. Moreover, stanene is supposedly a near room-temperature topological insulator [88]. Furthermore, honeycomb lattices composed of alternating Boron (Silicon) and Nitrogen (Carbon) atoms have been synthesized [89, 90]. In these binary compounds, the asymmetry between the different atoms induces

5 Dirac cones beyond the honeycomb lattice: a symmetry-based approach

a large gap in the spectrum, such that SiC is a semiconductor and hBN is an insulator.

Although the honeycomb lattice has proven to be a very successful platform for designing novel Dirac materials, quite some progress has been made in the field of non-honeycomb systems as well. A very promising class of materials in this respect is provided by graphynes [91]. These are two-dimensional carbon allotropes that are characterized by the presence of acetylene bonds ($-C \equiv C-$) in their lattice structure. In particular, the alternating presence and absence of the acetylene bond leads to more complicated lattice structures, and consequently to a richer band structure. For example, β -graphyne exhibits six inequivalent Dirac cones in the Brillouin zone (BZ), whereas the recently proposed square graphynes have four [92]. Although graphynes have not yet been experimentally realized, the structurally similar graphdiyne has already been successfully synthesized [93]. Recent studies show that similar Dirac systems can also be realized in non-carbon materials. Indeed, a monolayer of the metal diboride TiB_2 exhibits six Dirac cones [94], and the rectangular Boron allotrope pmmn Boron has one pair of Dirac cones [95].

The above examples show that Dirac materials can thus have very different crystalline lattices, and may even be composed of different elements. If we forget in a first instance about the chemical composition, and focus instead on symmetries, we may distinguish three different classes of Dirac materials. The first class is formed by graphene, and the other materials that have the Dirac cones located at the high-symmetry (HS) K and K' points. Similarly, we may group together the Dirac systems that have their cones located along the HS lines. β -graphyne, square graphynes, pmmn Boron, and TiB_2 belong to this class. Finally, one may consider the systems that have their Dirac cones located at generic points in the BZ. A typical example of those is the organic conductor α -(BEDT-TTF) $_2\text{I}_3$ [96].

Given the diversity of chemical composition and lattice structure of the current Dirac materials, it is essential to acquire a better understanding of the conditions for the emergence of Dirac cones. This is precisely the aim of this chapter. Therefore, we first discuss in Sec. 5.1 the occurrence of band-crossing points in two-dimensional crystals. Then, in Sec. 5.2, we show that the Dirac cones along HS lines are a mere consequence of the mirror-reflection symmetry of the different materials. This allows us to promptly engineer Hamiltonians that display Dirac behaviour, and in particular, to realize a

multitude of Dirac cones, which bring us from the $SU(4)$ case in graphene to a generic $SU(2N)$, for N -valley degrees of freedom ($N=1,2,4,6,8,12$). Then, in Sec. 5.3 we extend the discussion to systems that have Dirac cones located at arbitrary points in the BZ. Throughout this chapter, we illustrate our analysis by discussing the various cousins of graphene. Our conclusions are presented in Sec. 5.4.

5.1 Band crossing points

Dirac systems are characterized by a band-crossing point (BCP), from which the two bands disperse linearly. Such a BCP can be studied using a minimal two-band model, for which the Hamiltonian is given by a Hermitean 2×2 matrix $\tilde{H}(\vec{q})$, with elements $\tilde{H}_{ij}, i, j = 1, 2$. The presence of a degeneracy means that there exist two eigenvectors $|\Psi\rangle$ and $|\Phi\rangle$ with the same energy E . This requires the following relations to hold:

$$\tilde{H}_{11} = \tilde{H}_{22}, \quad \text{Im}[\tilde{H}_{12}] = \text{Re}[\tilde{H}_{12}] = 0. \quad (5.1)$$

Hence, three conditions must be fulfilled for the degeneracy to occur, while there are only two variables, q_x and q_y , to tune. This result is known as the Wigner-von Neumann theorem [97] (see also Ref. [98] for a generalized Wigner-von Neumann theorem). Therefore, for a BCP an additional symmetry is required, to ensure that at least one of these conditions is automatically satisfied. We will now discuss three different possibilities that may occur. Here and in the remainder of this text, we restrict ourselves to spinless fermions in the presence of time-reversal symmetry (TRS).

(I) In the case of the honeycomb lattice, the BCP occurs at the K^+ and K^- points, which are located at the corners of the hexagonal BZ. At these HS points, the symmetry of the lattice ensures that all three conditions are automatically satisfied. This is due to the combination of a threefold rotational symmetry around each lattice point, and the reflection symmetry relating the two sublattices. For this reason, the Dirac cone in graphene is called an essential degeneracy. Other systems with Dirac cones at the K^+ and K^- points include the ruby and Kagomé lattices [99]. Moreover, the Kagomé lattice exhibits a quadratic BCP at the Γ point [100].

(II) Let us consider a system that is governed by the Hamiltonian \tilde{H} , in the presence of a mirror-symmetry \hat{M} . For a momentum \vec{q} that lies along the HS

5 Dirac cones beyond the honeycomb lattice: a symmetry-based approach

Lattice	Brillouin zone	Representation	Space group	Examples
(a) <i>square</i>		s/d_{xy}	 p4mm	square-graphynes
		$s/d_{x^2-y^2}$	 p4mg & p4mm	
(b) <i>rectangular</i>		s/p_y	 pm, p2mg & p2mm	<i>pmmn</i> -Boron
		s/p_x	 pm, p2mg & p2mm	
(c) <i>triangular</i>		$s/f_{x(3y^2-x^2)}$	 p6mm & p3m1	β -graphyne
		$s/f_{y(3x^2-y^2)}$	 p6mm & p31m	TiB ₂
(d) <i>centered rectangular</i>		s/p_y	 cm & c2mm	strained graphene
		s/p_x	 cm & c2mm	

Figure 5.1: Table displaying different realizations of Dirac system with cones along high-symmetry lines. The first column shows four different Bravais lattices. Here, the mirror-symmetry is indicated by the red and blue dashed lines. The corresponding high-symmetry lines are displayed in the Brillouin zone in the second column. For each lattice, we can choose two different representations for the valence and conduction band, which we label by the corresponding atomic orbitals. Furthermore, we denote the different space groups that can host these Dirac cones, and give examples of materials where they occur.

5.2 2D lattices with cones along high-symmetry lines

lines, we have $[\tilde{M}, \tilde{H}(\vec{q})] = 0$. Now, by combining this commutation relation with the fact that $\tilde{M}^2 = I$, where I is the identity, we can block-diagonalize $\tilde{H}(\vec{q})$

$$\tilde{H}(\vec{q}) = \begin{pmatrix} \tilde{H}_+(\vec{q}) & 0 \\ 0 & \tilde{H}_-(\vec{q}) \end{pmatrix}, \quad (5.2)$$

where $\tilde{H}_\pm(\vec{q})$ corresponds to the even and odd states, respectively. If we assume that near the Fermi energy one may describe the system by two bands (even/odd), then the condition for the existence of a Dirac cone along the HS line reduces simply to $H_+(\vec{q}) = H_-(\vec{q})$. Hence, the number of conditions matches the number of variables, and there might be Dirac cones in such a system for a finite region in the parameter space of hopping- and on-site energies.

This discussion leads us to the following requirements for constructing a Dirac system with cones along the HS lines: (i) The system should exhibit mirror-symmetry; (ii) the two bands closest to the Fermi level should have opposite eigenvalues under the mirror-symmetry; (iii) the bands should cross.

Notice that we have not made use of the TRS. However, in the absence of TRS the hopping parameters can pick up a phase, which may break the mirror symmetry.

(III) Finally, we consider a system that exhibits both inversion and TRS. TRS implies that $\tilde{H}(\vec{q}) = \tilde{H}^*(-\vec{q})$, whereas typically the inversion symmetry imposes that $\tilde{H}(\vec{q}) = \sigma_i \tilde{H}(-\vec{q}) \sigma_i$, with $i = 0, 1$, or 3 , where σ_i denote the Pauli matrices and σ_0 the identity matrix. Hence, if we combine the two relations we obtain $\tilde{H}(\vec{q}) = \sigma_i \tilde{H}^*(\vec{q}) \sigma_i$. In this case, just one of the relations in Eq. (5.2) is automatically satisfied, and one might find Dirac cones, because the number of equations matches the number of variables.

Finally, we remark that in the remainder of this chapter we limit ourselves to Dirac systems for which the cones are related by symmetry. In particular, this ensures that all Dirac cones lie precisely at the Fermi level.

5.2 2D lattices with cones along high-symmetry lines

Here, we investigate the various Dirac systems belonging to class II. Given such a system, we may classify it depending on the symmetry of the crystal lattice and the set of HS lines along which the Dirac cones are located.

Equivalently, we need to specify the mirror symmetries for which the valence and conduction bands have opposite parity.

The full symmetry of the crystal lattice is given by the space group. A crystal can be seen as a Bravais lattice that encodes the translational symmetry together with a basis that specifies the positions and chemical composition of the atoms in the unit-cell. For example, graphene consists of a two-atom basis of carbon with an underlying triangular Bravais lattice. In general, the crystal corresponds to a decorated Bravais lattice. Hence, the space group that describes the combined symmetry of the Bravais lattice and the basis does not need to coincide with the underlying Bravais lattice. In particular, in two dimensions there are 17 different space groups, see e.g. Ref. [101]. Since the class II Dirac systems can only occur for crystals with mirror-symmetry, we will only encounter 9 of them.

Given the space group, we can identify the sets of HS lines and study the corresponding Dirac systems. Moreover, for each realization we construct a minimal Hamiltonian. This Hamiltonian is only valid at low energies around the Dirac cone because away from the Dirac cone other bands may become important. These minimal models can always be chosen to be chiral, meaning that the Hamiltonian is a linear combination of just two Pauli matrices. For each model, we discuss a novel Dirac material as a concrete example. Our analysis focuses on the four primitive Bravais lattices depicted in Fig. 5.1. Here, we do not consider the oblique lattice, as it does not have any mirror symmetry. Then, for each Bravais lattice we extend the discussion to the space groups that have the same underlying lattice. We discuss the different Bravais lattices in the following order: (i) square, (ii) rectangular, (iii) triangular, and (iv) the centered rectangular. The results of this section are schematically summarized in Fig. 5.1.

5.2.1 Square lattice

A prototypical example of a Dirac system with a square Bravais lattice is square graphyne. Its crystal lattice and band structure are shown, respectively, in Figs. 5.2(a) and 5.2(b). Whereas in graphene each unit cell contains two carbon atoms, for square graphyne there are 24 carbon atoms. Its band structure exhibits four highly anisotropic Dirac cones, all located at the boundary of the BZ (B point in Fig. 5.2(b)). Moreover, along the lines connecting the Γ and M points, the band structure exhibits a small gap.

5.2 2D lattices with cones along high-symmetry lines

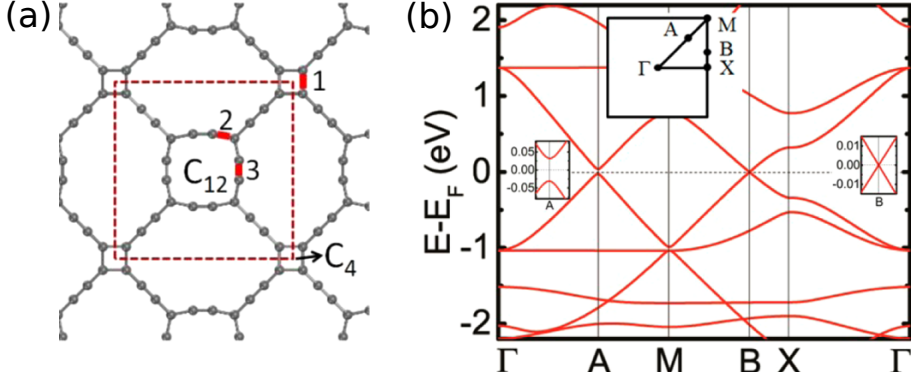


Figure 5.2: (a) Lattice structure of square-graphyne; (b) Band structure along HS lines, obtained from *ab initio* calculations. Reprinted (adapted) with permission from Ref. [92]. Copyright (2015) American Chemical Society.

The location of the Dirac cones hints at the fact that the existence of these cones can be understood from the mirror-reflection symmetries of the square lattice.

(i) s and d_{xy}

Inspection of Fig. 5.1(a) shows that the boundary of the BZ together with the lines connecting the $\Gamma-X$ and $\Gamma-Y$ points are associated to the mirror symmetries indicated by the red dashed lines. In particular, one can realize Dirac cones along the red dashed lines by constructing a two-band model composed of two Bloch waves, of which one is even with respect to all mirror-reflection symmetries, and the other is odd with respect to the symmetries indicated by the red dashed lines, but even with respect to the remaining ones. This is achieved, for example, in a two-band model composed of an s and d_{xy} orbital. The minimal Hamiltonian for such a system is given by

$$\hat{H} = \sum_{\vec{q}} g(\vec{q})(s_{\vec{q}}^\dagger s_{\vec{q}} - d_{\vec{q}}^\dagger d_{\vec{q}}) + \sum_{\vec{q}} h(\vec{q}) s_{\vec{q}}^\dagger d_{\vec{q}} + h.c., \quad (5.3)$$

with $g(q_x, q_y) = \epsilon_0 + V_{nn}[\cos(q_x) + \cos(q_y)]$ and $h(q_x, q_y) = V_{sd}[\cos(q_x + q_y) - \cos(q_x - q_y)]$. Here, ϵ_0 is an on-site energy, V_{nn} is the nearest-neighbor hopping parameter, and V_{sd} accounts for the hybridization among next-nearest neighbor s and d orbitals. In particular, this model exhibits Dirac cones if $|\epsilon_0| < 2|V_{nn}|$.

5 Dirac cones beyond the honeycomb lattice: a symmetry-based approach

Note that one does not require specifically atomic s and d_{xy} orbitals; this only illustrates under which representation the bands should transform. For example, in square-graphynes the bands are composed of the atomic p_z orbitals.

(ii) s and $d_{x^2-y^2}$

To realize Dirac cones along the blue-dashed lines connecting the $\Gamma - M$ points, the Bloch waves should transform under the same representation as the s and $d_{x^2-y^2}$ orbitals, such that they have opposite parity with respect to the symmetries indicated by the blue-dashed lines in Fig. 5.1. To our knowledge, there are no known materials that realize this model, although it may be promptly engineered using cold atoms. Here, the minimal Hamiltonian with the desired properties is still given by Eq. (5.3), but now one has to replace the d_{xy} orbital by a $d_{x^2-y^2}$ orbital. As a result, the hybridization is between nearest-neighbor s and d orbitals and $h(q_x, q_y) = V_{sd}[\cos(q_x) - \cos(q_y)]$. This model also exhibits Dirac cones for $|\epsilon_0| < 2|V_{nn}|$. In addition, the full symmetry of the square Bravais lattice is not required, as this model can also be realized for the space group $p4mg$.

5.2.2 Rectangular lattice

Rectangular crystals with Dirac cones are pervasive; some recent examples that have attracted much attention include multilayer phosphorene, pmmn Boron, and 6, 6, 12-graphyne. Whereas pmmn Boron and biased multilayer phosphorene exhibit a single pair of Dirac cones [24, 28], the 6, 6, 12-graphyne has two pairs. Because these two pairs of Dirac cones are not related by any symmetry, we will not discuss 6, 6, 12-graphyne here. In phosphorene, the Dirac cones actually arise due to the presence of glide-reflection symmetry. Therefore we defer its discussion to Sec. 5.4.

The rectangular lattice exhibits mirror-reflection symmetry in the vertical and horizontal direction, which is represented, respectively, by the red- and blue-dashed lines in Fig. 5.1(b). For the rectangular Dirac system pmmn Boron (see Figs. 5.3(a) and 5.3(b), where the lattice and band structure are depicted, respectively), the Dirac cones are located along the HS line connecting the $\Gamma - X$ points. This indicates that these Dirac cones are a consequence of the mirror-symmetry in the vertical direction.

(i) s and p_x (p_y)

The HS lines connecting the $\Gamma - X(Y)$ points and the $Y(X) - M$ points are

5.2 2D lattices with cones along high-symmetry lines

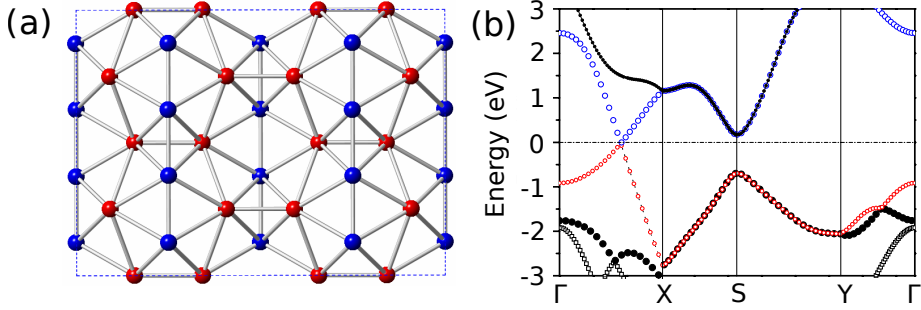


Figure 5.3: (a) Lattice structure of pmmn Boron; (b) Band structure along HS lines, obtained from *ab initio* calculations. Figures extracted and edited from Ref. [95].

associated to the mirror-symmetry indicated by the blue (red) dashed lines in Fig. 5.1(b). A two-band model with Dirac cones along these HS lines should be composed of Bloch waves with opposite parity under reflection in the $y(x)$ -direction. In particular, this is realized in a two-band model composed of s and $p_x(p_y)$ -orbitals, for which the minimal Hamiltonian reads

$$\hat{H} = \sum_{\vec{q}} g(\vec{q}) (s_{\vec{q}}^\dagger s_{\vec{q}} - p_{\vec{q}}^\dagger p_{\vec{q}}) + \sum_{\vec{q}} h(\vec{q}) s_{\vec{q}}^\dagger p_{\vec{q}} + h.c., \quad (5.4)$$

with $g(q_x, q_y) = \epsilon_0 + V_{nn,x} \cos(q_x) + V_{nn,y} \cos(q_y)$, and $h(q_x, q_y) = iV_{sp} \sin(q_x)$ or $h(q_x, q_y) = iV_{sp} \sin(q_y)$. Here, $V_{nn,x(y)}$ denotes the hopping parameter in the $x(y)$ direction, and V_{sp} is the nearest-neighbor hopping parameter that hybridizes the s and p orbitals. This band structure exhibits Dirac cones for $|\epsilon_0 + V_{nn,x}| < |V_{nn,y}|$ and $|\epsilon_0 - V_{nn,x}| < |V_{nn,y}|$. Note that this Dirac system can be realized in the absence of spatial inversion symmetry, as it can occur for the space groups pm, p2mg, and p2mm. Here, we have assumed that the translation vectors of the rectangular lattice are still given by the unit vectors pointing in the x and y directions.

5.2.3 Triangular lattice

Most of the already synthesized two-dimensional materials have a triangular Bravais lattice. In particular, this applies to graphene, silicene, germanene, and stanene. However, for these systems the Dirac cone is an essential

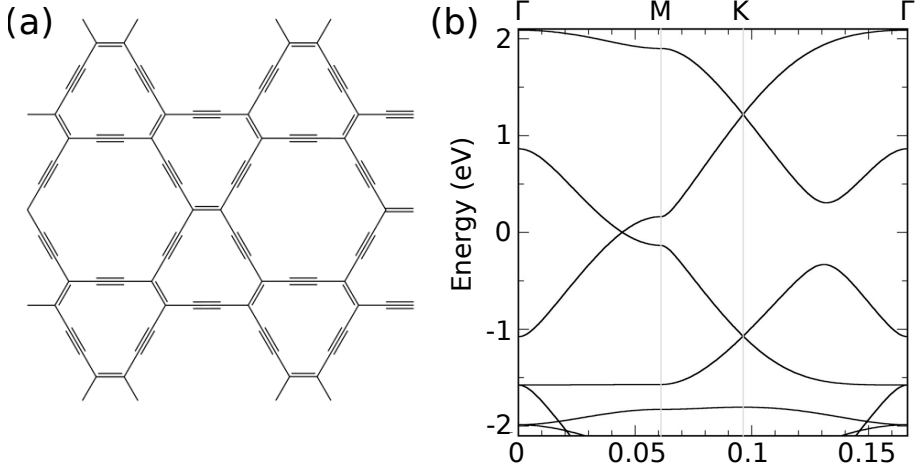


Figure 5.4: (a) Lattice structure of β -graphyne; (b) Band structure along HS lines, obtained from *ab initio* calculations. Figures extracted and edited from Ref. [91].

degeneracy. A typical example of a material with a triangular lattice and Dirac cones along HS lines is β -graphyne, see Fig. 5.4(a). Its unit cell consists of 18 carbon atoms, and has the shape of a hexagon. This carbon allotrope has six inequivalent Dirac cones located along the lines Γ -M (see Fig. 5.4(b)). A different example is provided by TiB_2 (see Fig. 5.5(a)). This material has also six Dirac cones, but they are located along the HS lines Γ -K and Γ -K' (see Fig. 5.5(b)). Each of these systems can be seen as a typical example of a triangular Dirac system.

(i) s and $f_x(3y^2-x^2)$

From Fig. 5.1(c), we infer that the HS lines connecting the Γ -M points are associated with the mirror-reflection symmetry indicated by the red-dashed lines. To realize Dirac cones along this set of HS lines, one should construct a two-band model for which the Bloch waves have equal (opposite) parity with respect to the blue (red) dashed lines. This can be realized in a model composed of s and $f_x(3y^2-x^2)$ orbitals, for which the minimal Hamiltonian

5.2 2D lattices with cones along high-symmetry lines

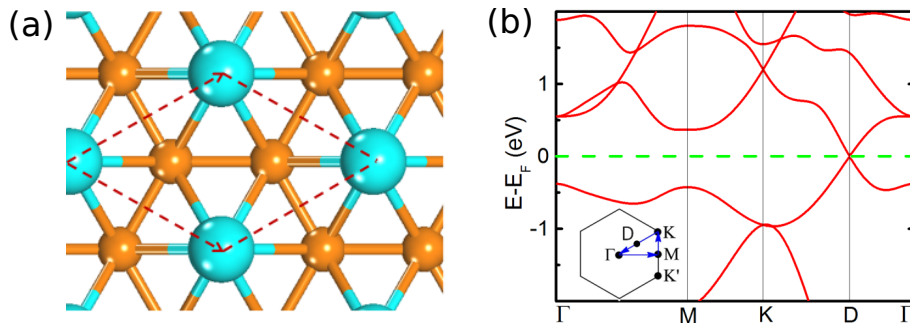


Figure 5.5: (a) Lattice structure of TiB_2 ; (b) Band structure along HS lines, obtained from *ab initio* calculations. Figures extracted and edited from Ref. [94].

reads

$$\hat{H} = \sum_{\vec{q}} g(\vec{q})(s_{\vec{q}}^\dagger s_{\vec{q}} - f_{\vec{q}}^\dagger f_{\vec{q}}) + \sum_{\vec{q}} h(\vec{q})s_{\vec{q}}^\dagger f_{\vec{q}} + h.c., \quad (5.5)$$

with $g(q_x, q_y) = \epsilon_0 + V_{nn}[\cos(q_x) + \cos(q_x/2 + q_y\sqrt{3}/2) + \cos(q_x/2 - q_y\sqrt{3}/2)]$ and $h(q_x, q_y) = iV_{sf}[\sin(q_x) + \sin(-q_x/2 - q_y\sqrt{3}/2) + \sin(-q_x/2 + q_y\sqrt{3}/2)]$. Here, V_{sf} denotes the nearest-neighbor hopping between s and f orbitals. This Hamiltonian exhibits Dirac cones for $|\epsilon_0 + V_{nn}| < 2|V_{nn}|$.

Note that one does not require the full six-fold rotational symmetry of the triangular Bravais lattice because this model can be realized for the space group $p3m1$.

(ii) s and $f_{y(3x^2-y^2)}$

The remaining set of HS lines connects the $\Gamma - K$ and $\Gamma - K'$ points. These HS lines are associated to the mirror-reflection symmetry indicated by the blue-dashed lines in Fig. 5.1(c). Now, instead, one requires that the two relevant Bloch waves transform as the atomic s and $f_{y(3x^2-y^2)}$ orbitals. In particular, this is realized in TiB_2 . The minimal Hamiltonian is also given by Eq. (5.5), but now $h(q_x, q_y) = iV_{sf}[\sin(q_x\sqrt{3}/2 + q_y\sqrt{3}/2) + \sin(-\sqrt{3}q_y) + \sin(-q_x\sqrt{3}/2 + q_y\sqrt{3}/2)]$. Due to the symmetry, the hybridization between s and f orbitals here involves next-nearest neighbor hopping parameters. This minimal model exhibits Dirac cones for $|\epsilon_0 + 1.75V_{nn}| < 2.25|V_{nn}|$.

5.2.4 Centered rectangular lattice

We finalize our analysis with the centered-rectangular lattice. One can obtain this lattice in graphene strained along the armchair direction. The lattice exhibits mirror-reflection symmetry in the horizontal and in the vertical direction, indicated by the red and blue dashed lines in Fig. 5.1(d).

(i) *s* and p_y

The HS lines connecting the $\Gamma - X$ and the $Y - M$ points are associated to the vertical mirror reflection symmetry. To construct a model with cones along these HS lines, one should ensure that the Bloch waves have opposite parity with respect to the vertical mirror reflection. This is, for example, realized in a system composed of *s* and p_y orbitals. In this case, the minimal Hamiltonian is given by

$$\hat{H} = \sum_{\vec{q}} g(\vec{q})(s_{\vec{q}}^\dagger s_{\vec{q}} - p_{\vec{q}}^\dagger p_{\vec{q}}) + \sum_{\vec{q}} h(\vec{q})s_{\vec{q}}^\dagger p_{\vec{q}} + h.c. \quad (5.6)$$

with $g(q_x, q_y) = \epsilon_0 + V_{nn,y}[\cos(q_x/2 + q_y\sqrt{3}/2) + \cos(q_x/2 - q_y\sqrt{3}/2)] + V_{nn,x} \cos(q_x)$ and $h(q_x, q_y) = iV_{sp}[\sin(q_x/2 + q_y\sqrt{3}/2) + \sin(-q_x/2 + q_y\sqrt{3}/2)]$. This system may also be realized for the space group *cm*.

(ii) *s* and p_x

The remaining HS line connects the $\Gamma - Y$ points. In this case, the Hamiltonian should be composed of Bloch waves that transform in the same way as the *s* and p_x orbitals. The corresponding minimal Hamiltonian is still given by Eq. (5.6) but now with $h(q_x, q_y) = iV_{sp} \sin(q_x)$. Note that for the centered rectangular lattice we have taken the same lattice vectors as for the triangular lattice.

5.3 Away from high-symmetry lines

The Dirac systems that we have just presented do not form an exhaustive list by any means, as we have limited ourselves to systems with cones along the HS lines. From our analysis in Sec. 5.1, we know that the systems with Dirac cones away from HS lines must exhibit inversion symmetry. Unless such a system has a single pair of Dirac cones, one needs an additional symmetry that relates the different Dirac cones. In particular, this symmetry can be the rotational symmetry of the lattice, or the combination of rotational and

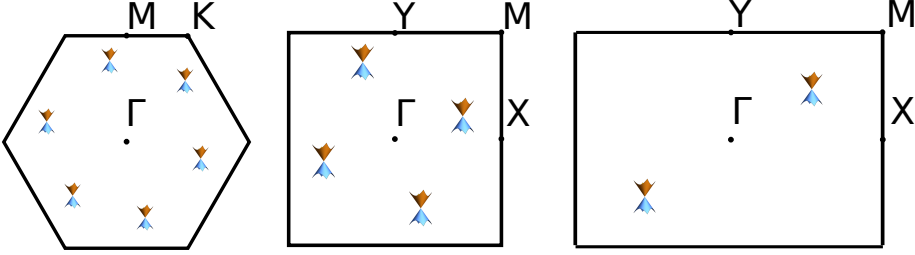


Figure 5.6: The class III Dirac systems, which do not exhibit mirror symmetry.

mirror-symmetry. Here, we discuss these cases separately. Moreover, we show how these systems may be seen to descend from class II Dirac systems.

First, we examine the systems for which the mirror-symmetry is broken, but the rotational symmetry is intact. Specifically, one may obtain such a system by adding a mirror-symmetry breaking term to a class II Dirac Hamiltonian. In real materials, this may be the case due to a substrate. There exist three different space groups describing systems without mirror symmetry but with the inversion symmetry, namely P6, P4, and P2. Note that space group PN has N -fold symmetry. For each of these space groups, we present an elementary model. The three different Dirac systems are schematically displayed in Fig. 5.6.

5.3.1 P6

Starting from the minimal Hamiltonian given in Eq. (5.5), which describes either β -graphyne or TiB_2 , we may easily break the mirror symmetry, while preserving the six-fold symmetry. In this way, we obtain a Hamiltonian that interpolates between the two systems, which is given by

$$\hat{H} = \sum_{\vec{q}} g(\vec{q})(s_{\vec{q}}^\dagger s_{\vec{q}} - f_{\vec{q}}^\dagger f_{\vec{q}}) + \sum_{\vec{q}} h(\vec{q}) s_{\vec{q}}^\dagger f_{\vec{q}} + h.c., \quad (5.7)$$

with $g(q_x, q_y) = \epsilon_0 + V_{nn}[\cos(q_x) + \cos(q_x/2 + q_y\sqrt{3}/2) + \cos(q_x/2 - q_y\sqrt{3}/2)]$ and $h(q_x, q_y) = iV_{sf,1}[\sin(q_x) + \sin(-q_x/2 - q_y\sqrt{3}/2) + \sin(-q_x/2 + q_y\sqrt{3}/2)] + iV_{sf,2}[\sin(q_x\sqrt{3}/2 + q_y\sqrt{3}/2) + \sin(-\sqrt{3}q_y) + \sin(-q_x\sqrt{3}/2 + q_y\sqrt{3}/2)]$. For $V_{sf,1} = 0$ or $V_{sf,2} = 0$, we retrieve the mirror-symmetric models. Depending on the sign of $V_{sf,2}/V_{sf,1}$, the Dirac cones are either shifted to the left or right with respect to the original location.

5.3.2 P4

In a similar fashion, we can smoothly deform the s/d_{xy} and $s/d_{x^2-y^2}$ (see Eq. (5.3)) models into each other. Then, the Hamiltonian reads

$$\hat{H} = \sum_{\vec{q}} g(\vec{q})(s_{\vec{q}}^\dagger s_{\vec{q}} - d_{\vec{q}}^\dagger d_{\vec{q}}) + \sum_{\vec{q}} h(\vec{q})s_{\vec{q}}^\dagger d_{\vec{q}} + h.c., \quad (5.8)$$

with $g(q_x, q_y) = \epsilon_0 + V_{nn}[\cos(q_x) + \cos(q_y)]$ and $h(q_x, q_y) = V_{sd,1}[\cos(q_x) - \cos(q_y)] + V_{sd,2}[\cos(q_x + q_y) - \cos(q_x - q_y)]$.

5.3.3 P2

Finally, we would like to discuss the least symmetric Dirac system, which only has a two-fold symmetry, as encountered in $\alpha\text{ET}_2\text{I}_3$. Whereas the two previously discussed systems can only exist on a triangular and square Bravais lattice, respectively, this Dirac system can be hosted on any Bravais lattice. Hence, this is the most robust Dirac system, for it only requires the presence of spatial-inversion symmetry. A minimal model defined on the rectangular Bravais lattice reads

$$\hat{H} = \sum_{\vec{q}} g(\vec{q})(s_{\vec{q}}^\dagger s_{\vec{q}} - p_{\vec{q}}^\dagger p_{\vec{q}}) + \sum_{\vec{q}} h(\vec{q})s_{\vec{q}}^\dagger p_{\vec{q}} + h.c., \quad (5.9)$$

with $g(q_x, q_y) = \epsilon_0 + V_{nn,x} \cos(q_x) + V_{nn,y} \cos(q_y)$ and $h(q_x, q_y) = iV_{sp,1} \sin(q_x) + iV_{sp,2} \sin(q_y)$. By putting $V_{sp,1} = 0$ ($V_{sp,2} = 0$), we recover the s/p_x (s/p_y) models discussed in Sec. 5.2.

These three Dirac systems can be seen to descend from the more symmetric class II systems. Yet, this is not true for all the class III Dirac systems. In particular, β -graphyne, in the presence of Rashba spin-orbit coupling, exhibits twelve Dirac cones [103, 104]. Moreover, proposals have been made to realize rectangular optical lattices with four Dirac cones located away from HS lines [102].

The conditions to realize these systems are very restrictive, because both inversion and mirror symmetry are required. The inversion symmetry protects the BCP, whereas the mirror symmetry guarantees that all Dirac cones are related. Specifically, for the space groups $p6mm$, $p4mm$, and $p2mm$ one may obtain a system with twelve, eight, or four symmetry related Dirac cones, see Fig. 5.7. Now, we discuss possible realizations of these systems for each of the space groups.

5.3.4 P6mm

It is possible to obtain a system with twelve symmetry related Dirac cones in several ways. The example of β -graphyne shows that one may start from six spin-degenerate Dirac cones along HS lines, and then use the Rashba spin-orbit coupling to split these into twelve Dirac cones. However, one does not need to use the spin degree of freedom. In particular, one might realize such a system in twisted bilayers of class II systems. If the two lattices are commensurate, a Moiré pattern is formed, see Fig. 5.8(a) [105]. To describe such a bilayer, one has to enlarge the unit cell. Correspondingly, the new BZ is reduced in size, see Fig. 5.8(b). More importantly, the original Dirac cones are not located along HS lines anymore. In particular, this applies to β -graphyne and TiB_2 . Furthermore, the inter-layer coupling may shift the position of the Dirac cones. This construction does not depend on any peculiarities of the triangular lattice, therefore, this can easily be extended to the square and rectangular Bravais lattices.

5.3.5 P4mm and P4mg

For the square lattice, it is possible to obtain a system with eight Dirac cones. The previous discussion shows that this may be realized in twisted-bilayer-square graphynes. However, this is not the only way to obtain eight symmetry-related Dirac cones. To see this, we start from a square lattice that is described by the s/d_{xy} model, for which the Dirac cones are located at the boundary of the BZ, as in square-graphynes. Now, we imagine for a moment that we are studying two uncoupled square lattices that are arranged as in Fig. 5.9(a). Then, if the filled and empty circles are equivalent, the

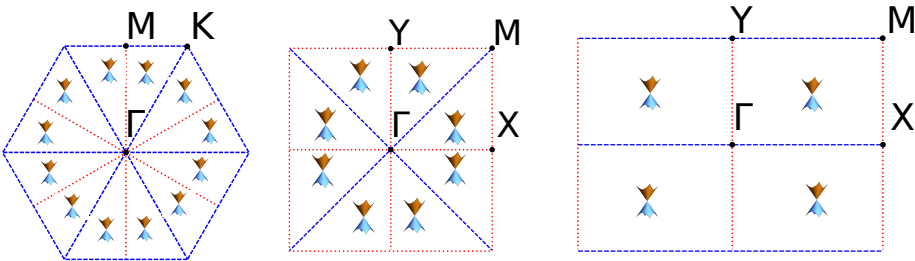


Figure 5.7: The class III Dirac systems, with rotational and mirror symmetry.

5 Dirac cones beyond the honeycomb lattice: a symmetry-based approach

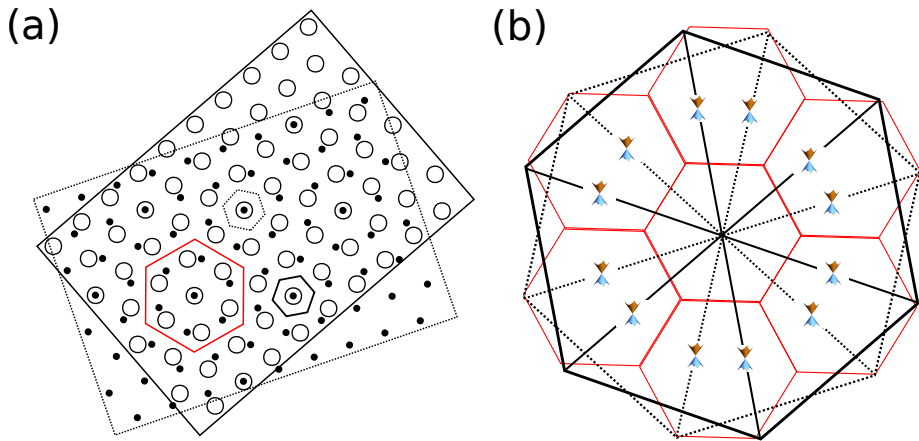


Figure 5.8: (a) A Moiré pattern is formed in a twisted bilayer. The original unit cells for the triangular lattices are denoted by the smaller solid and dashed hexagons. The red hexagon denotes the increased unit cell; (b) Here, the dashed (solid) BZ corresponds to the lattice formed by the filled (empty) circles. The reduced BZ is represented by the red central hexagon. We have drawn also the neighbor hexagons to illustrate how these are folded. In this example, we have assumed that the Dirac cones were originally located along the HS lines connecting the $\Gamma - K^+(K^-)$ points.

unit cell is decreased by half, and correspondingly the BZ is doubled. The new BZ features eight distinct Dirac cones, located away from HS lines (see Fig. 5.9(b)). The inclusion of a coupling between the two square lattices moves these cones away from their original position. Precisely this situation can be realized in bilayer-square graphynes, stacked in such a way that the smaller squares (C_4 in Fig. 5.2) are on top of the larger squares (C_{12} in Fig. 5.2). Note that such a construction does not apply to the triangular lattice, as there one has to triple the BZ, and hence the number of Dirac cones.

5.3.6 P2mm, P2mg, and C2mm

For the rectangular lattice, one may easily obtain a system with four Dirac cones. For example, one may start from a square lattice with four Dirac cones along the HS lines connecting the $\Gamma - M$ points. Then, if one transforms the square lattice into a rectangular one, while preserving the mirror symmetries of the rectangular lattice in the x and y direction, one keeps the four Dirac cones.

5.4 Conclusions and discussion

Dirac systems are very interesting because they are the heart of several unconventional phenomena, like the transparency of graphene or the Klein paradox. They were recently found to occur in materials like graphene, square graphyne or Pmmn boron, which have different lattice structures, ranging from honeycomb to square or triangular, and are composed of different atoms. In this work, we investigate the role of crystal symmetries in Dirac materials. The different systems have been classified within a unified two-band model, which effectively describes the different band structures that one may obtain for various space groups when one properly accounts for the symmetries of the valence and conduction bands.

We distinguish between three different classes of Dirac systems. Graphene belongs to the first class, and these systems are characterized by a BCP at the HS K and K' points. The class II Dirac systems have their Dirac cones located at HS lines. We have shown that for these systems the Dirac cones occur as a simple consequence of the mirror symmetries of the underlying crystal. This class hosts systems with two, four, and six Dirac cones. The

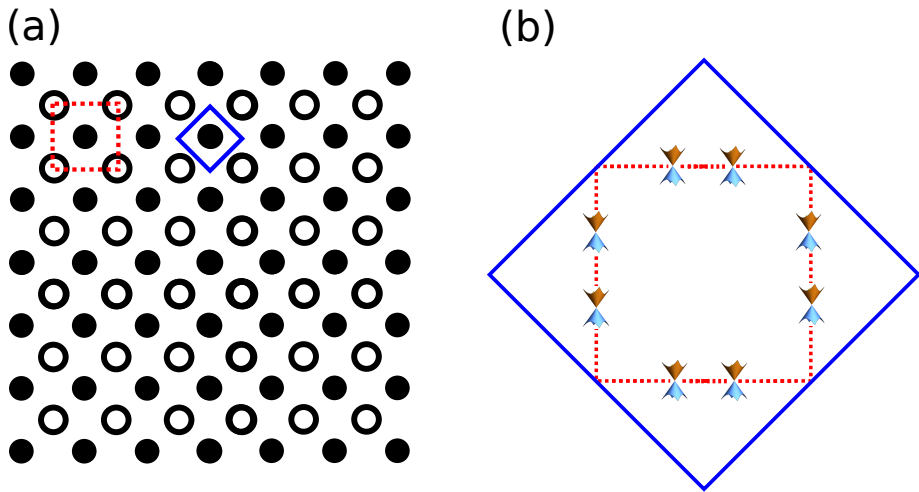


Figure 5.9: Sketch illustrating the doubling of the BZ, and the Dirac cones for the square lattice. (a) The filled and empty dots form a bipartite square lattice. When the filled and empty dots are different (identical), the unit cell is given by the red (blue) square. (b) The red (blue) dashed (solid) square shows the BZ, corresponding to the larger (smaller) unit cell in (a).

third class contains materials for which the Dirac cones occur at generic points in the BZ. We have shown that these systems can be realized in bilayers composed of class II systems. For example, in bilayer-square graphyne one realizes eight Dirac cones, while this number raises to twelve in twisted-bilayer β -graphyne.

A careful look at these different classes shows that these systems do not simply differ by the number of Dirac cones and by their position in the BZ, but there are other consequences. For example, in the class I Dirac systems, one can not remove the BCP unless one breaks one of the symmetries. Instead, for the class II and III systems, one may gap out the Dirac cones, whilst preserving all the symmetries. In particular, for class II systems the Dirac cones can annihilate at the time-reversal invariant momenta, whereas it has been shown that for class III systems this can occur at HS lines [103, 104].

The classification scheme proposed here relies on certain assumptions. Firstly, we have constrained ourselves to spinless fermions. Hence, we have not touched upon the effects of spin-orbit coupling in these systems. Moreover, we considered time-reversal symmetric systems and described them by generic two-band models. We should stress, however, that this minimal two-band model should be used with caution, especially when higher bands cannot be neglected. Another open question is what happens if we break the TRS. Finally, we did not consider glide-reflection symmetry in our analysis. Nevertheless, our results can be promptly extended to this case. Consider a system described by the Hamiltonian H with glide-reflection symmetry \hat{G} . Then, for a momentum \vec{q} that is invariant under the glide we find $[\hat{H}(\vec{q}), \hat{G}] = 0$. Since $\hat{G}^2 = \hat{T}_{\vec{a}_1}$, with \vec{a}_1 a lattice vector, the eigenvalues of \hat{G} are not simply ± 1 as for reflection symmetry. Instead, we find the eigenvalues $\pm \exp(i\vec{q} \cdot \vec{a}_1/2)$, but the bands along the HS lines with opposite eigenvalues still do not repel. The Dirac cones in phosphorene can be understood from such a glide-reflection symmetry.

Our results are relevant to many branches of physics. First of all, one may revert our analysis and use the understanding acquired here to design new Dirac materials. In particular, this approach can be very fruitful in the recently discovered semiconducting nanocrystal superlattices [106]. In these systems, the lattice is formed by the nanocrystals, which can be considered as artificial atoms. The advantage then is that one has control over the orbital content and hopping parameters. In this respect, they may serve as the ideal

5 Dirac cones beyond the honeycomb lattice: a symmetry-based approach

platform to realize the minimal two-band models that we have presented. An even higher degree of control can be obtained in patterned two-dimensional quantum wells and optical lattices loaded with cold atoms [107]. Honeycomb optical lattices have been recently realized [108], and experiments impossible in graphene have been viable in these systems. An illustrative example is the merging of Dirac cones upon a deformation of the honeycomb lattice that introduces anisotropies along the different hopping directions [109]. This anisotropy may be driven by shaking [110] or by superposing different square optical lattices and tuning the relative weight of each of them [111].

A very important consequence of the study performed here is that it opens the possibility to realize $SU(2N)$ pseudospin models, which exploit the multiple valley internal degrees of freedom. The possibility to realize optical lattices with high-spin atoms, like Sr or Dy has attracted much attention recently [112]. These systems allows one to study $SU(2N)$ magnetism, and were proposed to be a paradigm to engineer synthetic dimensions [113]. Here, we show that these concepts can be extended to the valley degree of freedom, with N up to 12.

Finally, we envision that the minimal models can be used in calculations to study the effects of disorder, transport properties, or to study the lattice Green's function beyond the linear dispersion. In addition, these models can be promptly used to study the effects of spin-orbit coupling and to verify whether this leads to topological states with high-spin Chern numbers. Similarly, these models are very suited to study the appearance of edge states in nanoribbons, depending on the termination. Therefore, we hope that our results will provide a motivation to realize these more exotic Dirac systems and trigger further experiments in the field.

6 Band structure engineering on Cu(111)

Geometry, whether on the atomic or nanoscale, is a key factor for the electronic band structure of materials. A notable example is given by the honeycomb lattice of graphene, which yields a linear dispersion relation. At the other extreme we find flat-band systems, where particles do not have any dispersion at all. It turns out that the Lieb lattice features both. The Lieb lattice is a square-depleted lattice, described by three sites in a square unit cell as illustrated in Fig. 6.1(a). Two of the sites (indicated in red) are neighbored by two other sites. The third site in the unit cell (blue) has four neighbors. In the remainder of this chapter, these sites will be referred to as edge (red) and corner (blue) sites, respectively. A minimal tight-binding model for the Lieb lattice is given by the following Hamiltonian

$$\hat{H} = -t \sum_{i_1, i_2} a_{i_1, i_2}^\dagger (b_{1; i_1, i_2} + b_{1; i_1-1, i_2} + b_{2; i_1, i_2} + b_{2; i_1, i_2-1}) + h.c., \quad (6.1)$$

where a_{i_1, i_2}^\dagger creates an electron on the corner site, and $b_{1(2); i_1, i_2}^\dagger$ creates an electron on the horizontal (vertical) edge in unit-cell (i_1, i_2) , and t indicates the nearest-neighbor hopping constant. The band structure for this model is shown in Fig. 6.1(b). It is characterized by two remarkable features; a flat band, and a conical dispersion that touches the flat band at the M point. The origin of these features can be traced back to the lattice symmetries. First, let us address the flat band. The tight-binding Hamiltonian only contains terms hybridizing corner sites with edge sites. As a result, the Fourier transformed Hamiltonian is block-diagonal $\hat{H} = \sum_{\vec{q}} \tilde{H}(\vec{q})$, with

$$\tilde{H}(\vec{q}) = \begin{pmatrix} 0 & H_{AB}(\vec{q}) \\ H_{AB}^\dagger(\vec{q}) & 0 \end{pmatrix} = -t \begin{pmatrix} 0 & 1 + e^{-iq_x} & 1 + e^{-iq_y} \\ 1 + e^{iq_x} & 0 & 0 \\ 1 + e^{iq_y} & 0 & 0 \end{pmatrix}.$$

This block-diagonal structure is equivalent to the statement that $\tilde{H}(\vec{q})$ anti-commutes with a unitary matrix \tilde{C} , which in this case is given by $\tilde{C} =$

6 Band structure engineering on Cu(111)

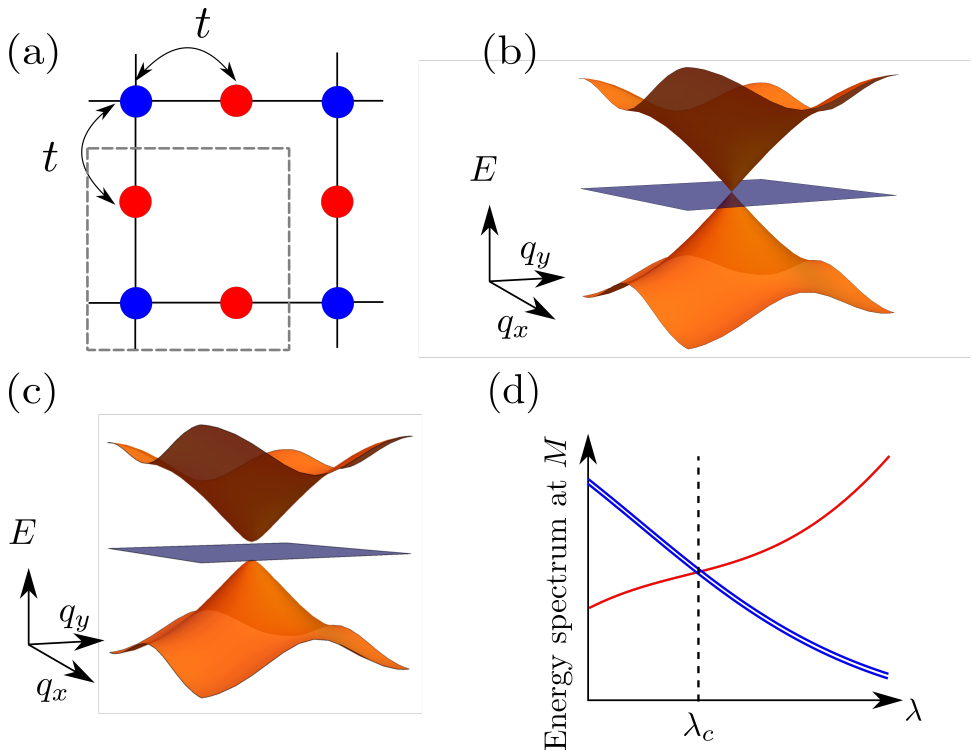


Figure 6.1: (a) Lieb lattice. Edge sites are shown in red and corner sites in blue. (b) Lieb lattice band structure with flat band and touching cone. (c) Lieb lattice band structure with only a flat band. (d) Evolution of spectrum at the M point as a function of some arbitrary parameter λ . The degenerate states with rotation eigenvalues i and $-i$ are shown in blue, whereas the singlet is shown in red.

$\text{diag}(1, -1, -1)$. Now, suppose that $|\epsilon\rangle$ is an eigenstate with energy ϵ , then it follows that $\tilde{C}|\epsilon\rangle$ is an eigenstate with energy $-\epsilon$. However, $\tilde{H}(\vec{q})$ is an odd-dimensional matrix, and therefore it follows that there is at least one eigenstate with eigenvalue 0. Although the sublattice symmetry is at the heart of the flat band, it does not guarantee the presence of the touching cones. For example, we can gap the cone by including anisotropic hoppings, see Fig. 6.1(c), where we have plotted the dispersion corresponding to

$$\tilde{H}(\vec{q}) = -t \begin{pmatrix} 0 & 1 + 1.1e^{-iq_x} & 1 + .8e^{-iq_y} \\ 1 + 1.1e^{iq_x} & 0 & 0 \\ 1 + .8e^{iq_y} & 0 & 0 \end{pmatrix}.$$

It turns out that the touching cone can be attributed to the combination of inversion and sublattice symmetry. Let us consider inversion with respect to the corner site. In that case the inversion operator is given by $\tilde{I}_A(\vec{q}) = \text{diag}(1, e^{-iq_x}, e^{-iq_y})$. Now, the crux of the story is that at the M point the inversion operator $\tilde{I}_A(M)$ coincides with the chiral operator $\tilde{C} = \text{diag}(1, -1, -1)$. Hence, $\tilde{H}(M)$ commutes and anti-commutes with the matrix $\text{diag}(1, -1, -1)$, therefore it follows that $\tilde{H}(M) = 0$.

In practice there will always be terms that break the sublattice symmetry. However, one may also understand the triple degeneracy at the M point in another way. Namely, the Lieb lattice exhibits a fourfold symmetry axis. Since the M point is invariant under this rotation, we can label the different eigenstates by their energy and rotation eigenvalues. Now suppose that we find an eigenstate at M which has rotation eigenvalue i , i.e.

$$\tilde{H}(M)|\epsilon, i\rangle = \epsilon|\epsilon, i\rangle \quad \text{and} \quad \tilde{C}_{4,A}|\epsilon, i\rangle = i|\epsilon, i\rangle.$$

If in addition the system is time-reversal symmetric, then $\tilde{T}|\epsilon, i\rangle$ is also an eigenstate of $\tilde{H}(M)$, with energy ϵ . Moreover, it also an eigenstate of $\tilde{C}_{4,A}$:

$$\tilde{C}_{4,A}(\tilde{T}|\epsilon, i\rangle) = \tilde{T}\tilde{C}_{4,A}|\epsilon, i\rangle = \tilde{T}i|\epsilon, i\rangle = -i(\tilde{T}|\epsilon, i\rangle)$$

hence $\tilde{T}|\epsilon, i\rangle$ has opposite eigenvalue with respect to $\tilde{C}_{4,A}$, and therefore the two states are orthogonal. Therefore, from this simple symmetry analysis we have learned that in the presence of fourfold-rotational symmetry and time-reversal symmetry we can have double degeneracies at the M point. Now suppose that the Hamiltonian depends on a tunable parameter, say

6 Band structure engineering on Cu(111)

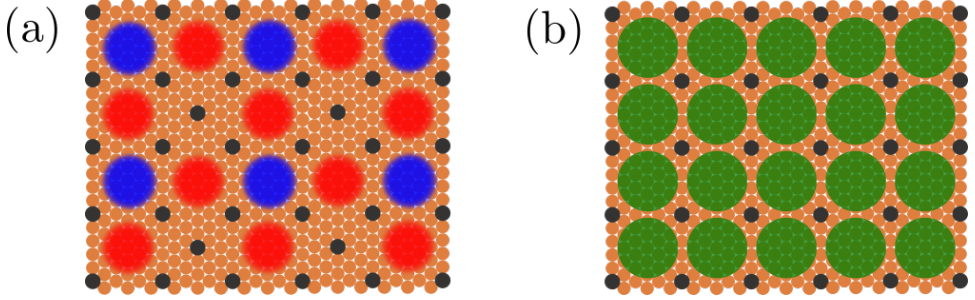


Figure 6.2: (a) Sketch of molecular Lieb lattice. (b) Sketch of a molecular square lattice.

λ . Hence, it might be that for $\lambda < \lambda_c$ the lowest band has eigenvalue ± 1 and there is a double degeneracy, with eigenvalues $+i$ and $-i$, whereas for $\lambda > \lambda_c$ the roles are reversed, now the double degeneracy is lowest in energy. Then, precisely at $\lambda = \lambda_c$ there is a triple degeneracy at the M -point, which resembles the Lieb-lattice dispersion, see also Fig. 6.1(d). Below we show that one can engineer such a Lieb-like dispersion on the surface of copper.

6.1 Experimental results

Recently new techniques have been proposed and applied to generate artificial 2D electronic lattices [107]. For example it has been shown that one can use electron-beam lithography to engineer a Lieb lattice in ultra-thin semi-conductor films [114]. Alternatively, one can create a Lieb lattice by assembling a molecular lattice on a substrate that features a surface state using a scanning tunneling microscope, as has been used before to prepare an artificial graphene system [115]. In the following, we will describe how atomic scale manipulation of carbon monoxide (CO) molecules on Cu(111) can be used to generate and characterize an electronic Lieb lattice.

The design of the molecular Lieb lattice is not trivial for several reasons. First, the Lieb lattice has four-fold rotational symmetry, whereas substrates that exhibit a surface state close to the Fermi energy such as Cu(111) have hexagonal symmetry. Furthermore, the CO molecules on Cu(111) act as repulsive scatterers, confining the electrons to the space between the CO molecules [115–118]. This implies that the CO molecules should compose

the anti-lattice of the electronic Lieb lattice. Our design consists of a CO square lattice, which defines the trivial anti-lattice of a square lattice, with one CO placed in the center of four CO molecules to form the anti-lattice of a depleted square lattice (*cf.* Fig.6.3 (a)). This design was recently proposed independently by Qiu *et al.* [119]. The size of the unit cell is chosen to be $6\sqrt{3}a_0 \times 10a_0 (\approx 2.66 \text{ nm} \times 2.56 \text{ nm})$, where $a_0 = 0.256 \text{ nm}$ is the Cu(111) nearest-neighbour distance. Two factors play a critical role in the design. First, this arrangement of CO molecules provides the best approximation to the four-fold symmetry of the Lieb lattice on the hexagonal Cu(111) substrate. Furthermore, the size of the unit cell determines the position of the bands of the lattice with respect to the Fermi level of the Cu(111) [115]. With the lattice constants described above, the lowest three bands are close to the Fermi level.

A lattice of 5×5 unit cells was assembled in the way shown in Fig. 6.3 (a). To provide further evidence that any observed features are due to the Lieb lattice, a small square lattice was created immediately next to the Lieb lattice, see also Fig. 6.2(b). Differential conductance spectra were acquired above various positions of the lattice (indicated by the blue and red points in Fig. 6.3 (a)). The spectra were normalized by the spectrum acquired on the clean Cu(111) surface, analogously to Ref. [115]. The resulting spectra above corner (blue) and edge sites (red) are shown in Fig. 6.3(b). We first focus on the spectrum acquired above a corner site (blue). Two peaks are observed, one at $V = -0.20 \text{ V}$ and one at $+0.18 \text{ V}$. These peaks can be assigned to the Van Hove singularities in the local density of states (LDOS). In between these two peaks, the LDOS reaches a minimum, which suggests a conical dispersion. In contrast, the edge-site spectrum (red) exhibits three peaks. In addition to the peaks at -0.20 V and $+0.18 \text{ V}$ there is another peak located at $V = -0.07 \text{ V}$.

To investigate the spatial distribution of the states, we acquired differential conductance maps, as well as 100 spectra along the line indicated in Fig. 6.3(a). This line starts and ends at an edge site and passes four corner-sites. The resulting contour plot is shown in Fig. 6.3(c). The peaks described above can be clearly recognized for each site, demonstrating that the LDOS features are a property of the lattice. For comparison, a differential conductance spectrum acquired over a site in the *square* lattice is shown in Fig.6.3(d), while a contour plot showing 125 spectra along a line are shown in Fig. 6.3(e). The spectra along the line again demonstrate the

6 Band structure engineering on Cu(111)

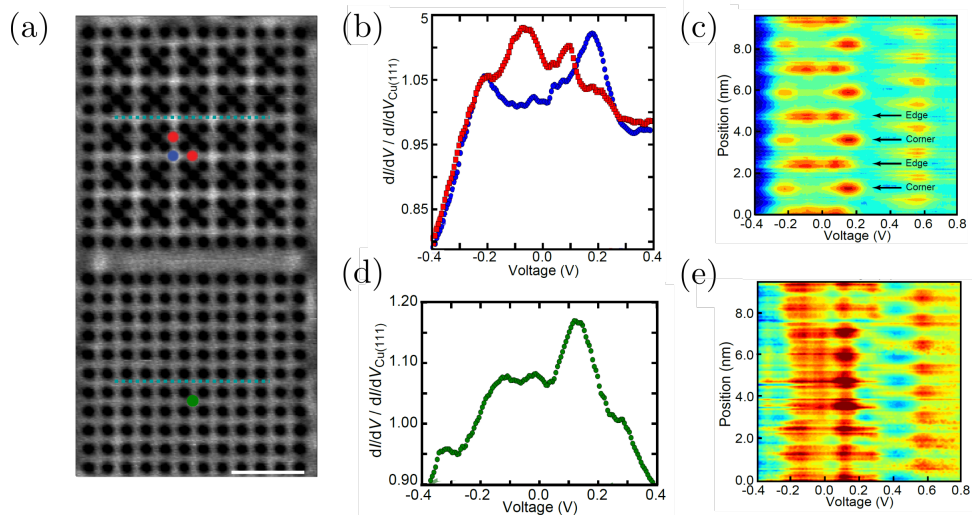


Figure 6.3: Electronic structure of a Lieb lattice. (a) STM image of a 5x5 Lieb (top) and square (bottom) lattice. Two edge sites and one corner site of the Lieb lattice are indicated in red and blue, respectively. The green circle indicates a site of the square lattice. Imaging parameters: $V = 50$ mV, $I = 1$ nA. Scale bar: 5 nm. (b) Normalized differential conductance spectra acquired above edge (red squares) and corner (blue circles) sites and local density of states at these sites calculated using the tight-binding method (solid lines). (c) Contour plot of 100 spectra taken along the line indicated in (a). The features observed in the spectra shown in (b) can be clearly recognized (see arrows). (d), (e) same as (b), (c), but for a square lattice. Note that the spectrum on the square lattice is qualitatively different from the spectra of the Lieb lattice.

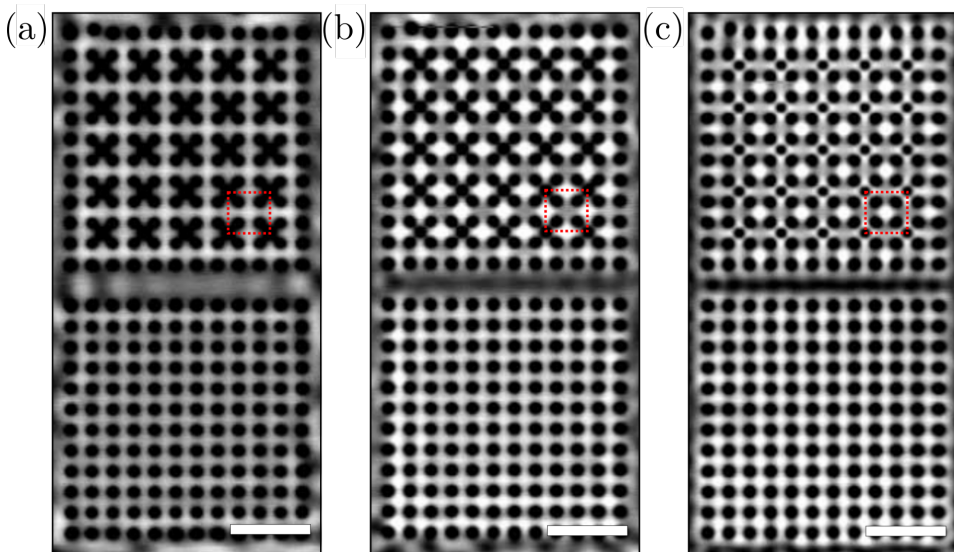


Figure 6.4: (a)-(c) Differential conductance maps acquired above a Lieb and a small square lattice at -0.200 V, -0.050 V, and $+0.150$ V, respectively. Scale bars: 5 nm.

6 Band structure engineering on Cu(111)

similarity of the features for equivalent sites (Fig. 6.3(e)). Importantly, the spectra are qualitatively different from the spectra obtained over the Lieb lattice. This further demonstrates that the features observed in the differential conductance spectra shown in Fig.6.3(b) are due to the Lieb lattice.

Fig. 6.4 shows several experimental constant-height differential conductance maps of the two lattices. For the square lattice, all equivalent sites appear identical at all three energies. In contrast, for the Lieb lattice at $V = -0.200$ V, both the edge and corner sites contribute significantly to the density of states. At $V = -0.050$ V, only the edge sites contribute. At $V = +0.150$ V, again both corner and edge sites contribute, with the first being dominant.

6.2 Numerical results

To establish whether the design described above leads to a Lieb-like dispersion, we perform numerical calculations. We describe the surface state on Cu(111) as a two-dimensional electron gas with an effective electron mass $m^* \approx 0.40m_e$ [120], where m_e is the electron mass. The band bottom is located at 445 meV below the Fermi level E_F [121]. We account for the CO molecules by including a potential V_{CO} . Hence, the Hamiltonian for the system of interest reads

$$\hat{H} = -\frac{\hbar^2}{2m^*}\nabla^2 + V_{CO}(r).$$

Since we consider a periodic array of CO molecules, we can label the eigenstates of H by a wavevector \vec{q} and band label n

$$\hat{H}\Psi_{\vec{q},n} = E_{\vec{q},n}\Psi_{\vec{q},n}.$$

Bloch's theorem states that we can write the eigenstates as the product of a plane wave and a periodic function, $\Psi_{\vec{q},n}(r) = e^{i\vec{q}\cdot\vec{r}}u_{\vec{q},n}(\vec{r})$, where $u_{\vec{q},n}(\vec{r} + \vec{a}_i) = u_{\vec{q},n}(\vec{r})$.

We now consider the case that $V_{CO}(r) = V_0$ if $\|\vec{r} - \vec{r}_{CO}\| \leq D/2$ and zero elsewhere, where \vec{r}_{CO} denotes the position of a CO molecule. This is also known as a muffin-tin potential. The range of the potential is set to the diameter of the CO molecules as they appear on the STM maps. We find $D = 0.6$ nm, in good agreement with DFT studies that were used for calculations

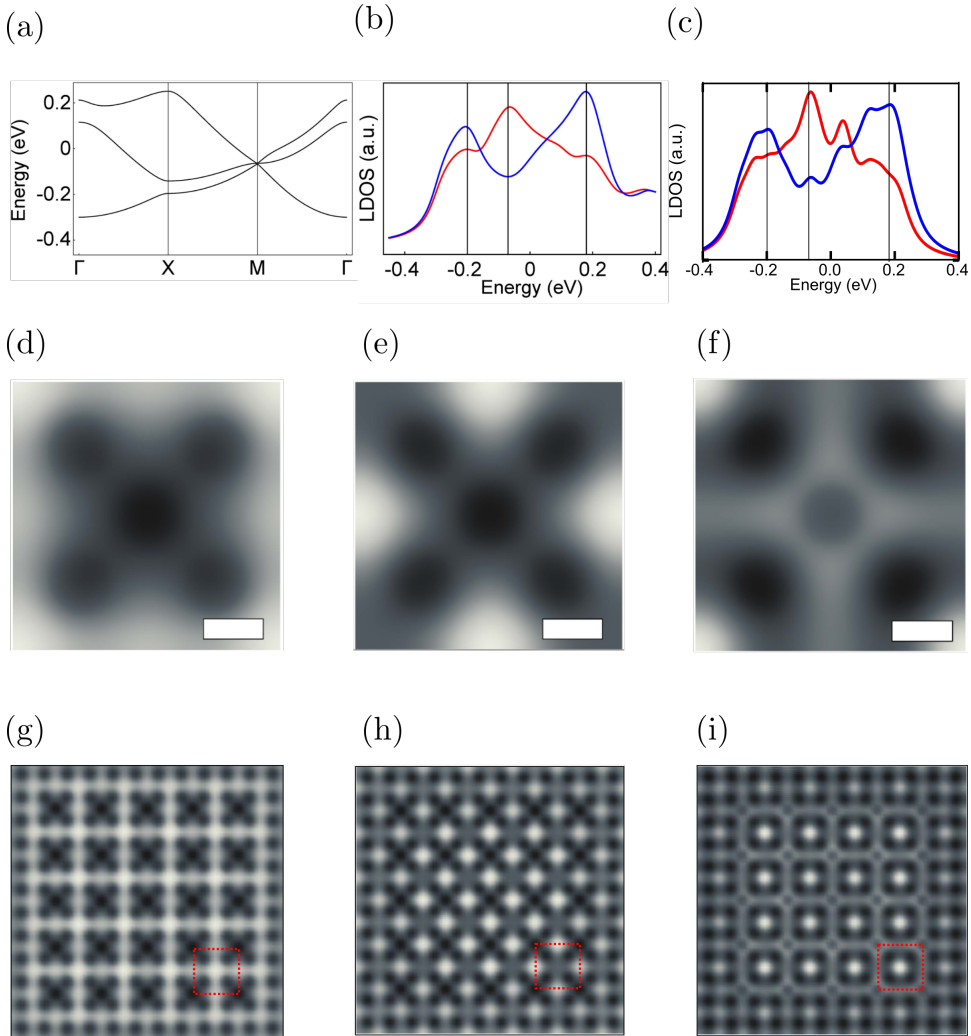


Figure 6.5: (a) Band structure along high-symmetry lines based on a muffin-tin approximation with $V_0 = 0.9$ eV, $D = 0.6$ nm and $a = 2.66$ nm. (b) Corresponding LDOS for an edge (red) and corner (blue) site. The vertical lines correspond to the first three Van Hove singularities. We included a Lorentzian energy level broadening of 80 meV. (c) LDOS for an edge and corner in a finite system. (d)-(f) Simulated maps at -0.200 eV, -0.070 eV, and 0.180 eV, respectively, corresponding to the Van Hove singularities. The scale bars are 0.6 nm. (g)-(i) Simulated STM maps for the finite geometry.

6 Band structure engineering on Cu(111)

on artificial graphene [118, 122]. For the height of the muffin-tin potential, we choose $V_0 = 0.9\text{eV}$. First, we calculate the bulk band structure for the geometry with 5 CO molecules per unit cell of $2.66\text{ nm} \times 2.66\text{ nm}$ using the described parameters in the muffin-tin approximation. The result is shown in Fig. 6.5(a). We find that the three lowest bands are indeed degenerate at the M point. The DOS exhibits three Van Hove singularities at -0.20eV , -0.07eV , and 0.18eV . These features are also present in the simulated STM maps and LDOS, as shown in Fig. 6.5(d)-(f) and Fig. 6.5(c), and , which are in good agreement with the measurements shown in Fig. 6.3(b) and Figs. 6.4(a)-(c). In particular, we also find that at the first (second) Van Hove singularity the simulated STM maps light up at the corners (edges). Note that we have included Lorentzian energy level broadening. We attribute this to the hybridization of the surface states with the bulk, induced by the CO molecules. Namely, due to the increased unit cell, the bulk and surface states overlap both in energy and momentum.

To study the role of finite-size effects in the experimentally realized lattice, we have solved the Schrödinger equation for the finite system with the same lattice geometry as in the experiment, *i.e.* a lattice with 5×5 unit cells surrounded by a 2DEG. We employed periodic boundary conditions for this entire system. The resulting LDOS for the edge and corner sites is displayed in Fig. 6.5(c) and the simulated STM maps at the Van Hove singularities are shown in Fig. 6.5(g)-(i). Both the LDOS and the simulated maps are in agreement with the experimental data shown in Figs. 6.3(b) and 6.4(a)-(c), respectively.

We have also performed muffin-tin calculations where we arrange the CO molecules in a square lattice, with the same unit-cell size, *i.e.* $2.66\text{ nm} \times 2.66\text{ nm}$ and using the same parameters. The corresponding band structure, LDOS, and simulated STM maps are shown in Fig. 6.6 (a)-(d). This large square lattice exhibits similar features as before. Most importantly, we obtain a triple degeneracy at the M point, which is located at -0.18eV . This degeneracy corresponds to the second Van Hove singularity in the LDOS. One can clearly see that the electrons localize at the edge sites. In contrast, we find that the first Van Hove singularity, which is located at -0.32eV , corresponds to the case where the electrons mainly localize on the corner sites. These results are also in good agreement with experimental results shown in Figs. 6.6(e) and (f). Compared to the design with 5 CO molecules per unit cell we find that the gaps between the bands at X and Γ are considerably

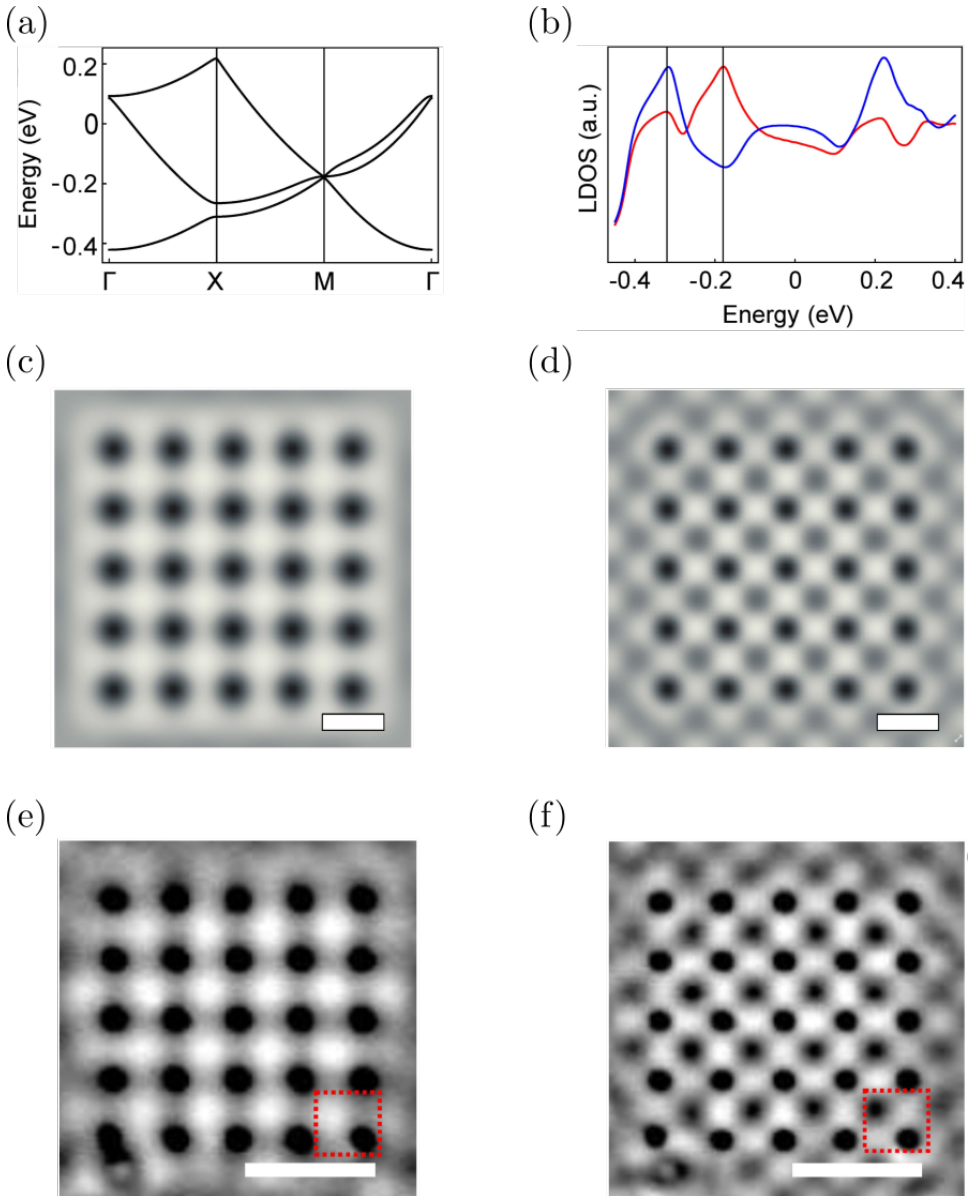


Figure 6.6: (a) Band structure of a large square lattice along high-symmetry lines. (b) LDOS for pseudo-edge (red) and pseudo-corner (blue) sites. The two vertical lines correspond to the first two Van Hove singularities. We included a broadening of 40 meV. (c), (d) Simulated maps at -0.320 eV and -0.180 eV for the finite system, including a broadening of 80 meV. Scale bar: 2.66 nm. (e), (f) Experimental differential conductance maps acquired above the large square lattice at -0.300 V and -0.150 V, respectively. Scale bar: 5 nm.

6 Band structure engineering on Cu(111)

smaller. Especially, we do not see a band gap opening between the second and third band at the Γ point.

6.3 Conclusion

The ability to generate electronic lattices using CO molecules on Cu(111) allows experimental realization and characterization of lattices that have only been investigated theoretically so far. Furthermore, this system is an ideal test-bed as it allows tuning of parameters that cannot be easily varied in a real solid-state material. In particular, one may tune the Fermi level by changing the lattice constant, one can consider specific strain profiles [115] and create (topological) defects [123].

7 Conclusion and Outlook

This thesis can roughly be divided into two parts. The first part comprises Chapters 2-4. There, we have investigated how the interplay between topology and symmetry manifests itself around defects in the crystal structure. In particular, we considered the presence of in-gap edge states, as well as edge and dislocation charges. The second part comprises Chapters 5 and 6, and concerns how symmetry and topology affect the band structure. Below, we give a summary of the results, as well as a small outlook.

7.1 Summary of the results

In Chapter 2, we have studied the presence of trivial edge states in inversion-symmetric insulators and semimetals. We have shown that the interplay between time-reversal and inversion-symmetry gives rise to a topological \mathbb{Z}_2 invariant, which is directly related to the quantization of the Zak phase $\gamma_{\text{Zak}}(k_{\parallel})$. In particular, we find that a non-trivial Zak phase generally leads to edge states. Hereby, we have generalized the result by Ryu and Hatsugai [11] to systems lacking chiral symmetry. These results are relevant for a broad range of 2D materials, including graphene, phosphorene and their multilayer configurations. This work, therefore, complements earlier studies on edge states in graphene based on the Dirac equation. Finally, we would like to point out that the relevance of our results is not restricted to 2D materials because the Zak phase has been recently used to explain the existence of drumhead surface states in the three-dimensional materials Cu_3N and Ca_3P_2 .

The Zak phase discussed in Chapter 2 is origin-dependent. For this reason, we considered an inversion-symmetric unit-cell, and put the origin at the center of the unit-cell. Moreover, we have seen that in the absence of edge states, the invariant can be linked to the edge charge. This has motivated us to study the excess edge charge in 1D crystalline insulators in greater detail, which is the subject of Chapter 3. We have found that in general the

7 Conclusion and Outlook

edge charge can be expressed as a Berry phase of the bulk electronic Bloch waves. For atomic chains possessing spatial symmetries interchanging the chain ends, excess charges always contain a topological contribution directly related to the topological invariants that can be associated with spatial-symmetric 1D systems. Finally, we have shown that for spinful time-reversal symmetric systems, the excess charge can be expressed using the notion of the partial Berry phases.

Then, in Chapter 4, we applied these results to derive a one-to-one correspondence between the charge localized around a dislocation characterized by a generic Burgers vector and the Berry phase associated with the electronic Bloch waves of two-dimensional crystalline insulators. Using this correspondence, we revealed a link between dislocation charges and the topological invariants of inversion and rotation symmetry-protected topological insulating phases both in the absence and in the presence of time-reversal symmetry. Our findings demonstrate that dislocation charges can be used as generic probes of crystalline topologies.

In Chapter 5, we provided a symmetry analysis of two-dimensional Dirac materials. We distinguish between three different classes of Dirac systems. Graphene belongs to the first class, and is characterized by two band-crossing points at the high-symmetry K^+ and K^- points. The class II Dirac systems have their Dirac cones located at high-symmetry lines. We have shown that for these systems the Dirac cones occur as a simple consequence of the mirror symmetries of the underlying crystal. This class hosts systems with two, four, and six Dirac cones. The third class contains materials for which the Dirac cones occur at generic points in the Brillouin zone. We have shown that these systems can be realized in bilayers composed of class II systems. For example, in bilayer-square graphyne one realizes eight Dirac cones, while this number raises to twelve in twisted-bilayer β -graphyne.

Chapter 6 is the result of an experimental collaboration with the groups of Daniël Vanmaekelbergh and Ingmar Swart. There the aim is to engineer artificial electronic lattices. Using an STM, CO molecules have been arranged on the Cu(111) surface. The CO molecules act as a repulsive potential, which therefore changes the band structure of Cu(111) surface state. We have compared both the differential conductance maps and the LDOS with muffin-tin calculations. In this way we have shown that the corresponding band structure features a Lieb-like dispersion.

7.2 Outlook

We hope that our work will spark further research on the interplay between topology and symmetry. Below, we discuss possible future research directions that are closely related to the contents of this thesis.

In Chapters 2-4 we have considered both 1D and 2D systems, but, essentially everything is still one-dimensional. We have simply relied on the fact that an edge is translation-invariant, and a dislocation can be made from gluing two translation-symmetric cylinders. However, there are scenarios where this is no longer true. In particular, this applies to excess charges surrounding a corner or a disclination. It would be interesting to ask whether the excess charges are still a bulk quantity, and if so, whether they correspond to some topological invariant.

In Chapter 5 we have discussed several Dirac systems. It would be natural to design artificial lattices that yield the class II Dirac systems. Some work along these lines has recently been performed for square lattices [124]. There it was found that by etching away a Lieb lattice from a 2D quantum well, one may engineer a system with four Dirac cones along high-symmetry lines. In addition, we would like to point out that these artificial lattices provide a natural platform to experimentally detect the topological invariants discussed in Chapters 2-4.

All in all, we believe that there is still a lot to be learned about the interplay between topology and crystalline symmetries.

8 Samenvatting

Dit proefschrift gaat hoofdzakelijk over het samenspel van symmetrie en topologie in kristallijne isolatoren en halfmetalen. In hoofdstukken 2-4 behandelen wij hoe dit samenspel zich manifesteert op de rand van een materiaal, maar ook rondom een dislocatie. Vervolgens beschouwen wij in hoofdstukken 5 en 6 hoe een kristalsymmetrie een singulariteit in de bandenstructuur stabiliseert. Alvorens dieper in te gaan op de resultaten van dit proefschrift zullen wij kort beschrijven wat een kristal is, en wat er bedoeld wordt met het samenspel van symmetrie en topologie.

8.1 De symmetrie en topologie van een kristal

Een kristal, of kristallijn materiaal, bestaat uit atomen die een regelmatig patroon vormen dat zich in de ruimte herhaalt. Als dit patroon zich slechts in 1 ruimtelijke dimensie herhaalt spreekt men van een 1-dimensionaal kristal, terwijl 2 en 3 dimensionale kristallen een patroon vormen dat zich herhaalt in respectievelijk twee en drie richtingen. Voor het gemak beperken we ons nu tot 1-dimensionale kristallen, zie Fig. 8.1 voor een schets van twee verschillende kristallen. De punten stellen atomen voor die met elkaar zijn verbonden door de chemische bindingen. De sterkte van deze binding wordt geïllustreerd met de dikte van de binding die we tekenen.

De twee getoonde kristallen zijn duidelijk verschillend, zo is de roosterconstante niet hetzelfde, en bestaat het ene kristal uit groene atomen, terwijl het andere kristal uit rode en blauwe atomen bestaat. Belangrijker nog is dat de twee kristallen een andere symmetrie hebben. Het groene kristal ziet er anders uit als u het voor een spiegel houdt, terwijl het blauw-rode kristal er nog steeds hetzelfde uitziet. Tegelijkertijd ziet het blauw-rode kristal er weer anders uit als u de pagina 180 graden draait, terwijl het groene kristal er nog steeds hetzelfde uitziet. Het blauw-rode kristal is spiegel-symmetrisch terwijl het groene kristal rotatie-symmetrisch is. Merk overigens op dat spiegelen en roteren met 180 graden wel iets gemeen hebben, namelijk als

8 Samenvatting

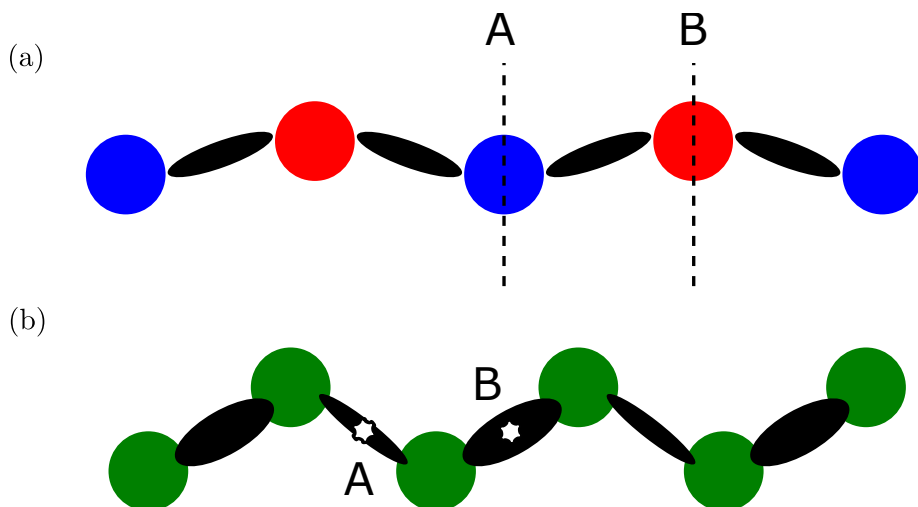


Figure 8.1: (a) Spiegel-symmetrisch kristal. (b) Rotatie-symmetrisch kristal.

we de operatie twee keer uitvoeren, verandert er helemaal niks (dit is een eigenschap van het spiegelen en roteren, en dus niet van het figuur dat gerooteerd of gespiegeld wordt). Precies deze eigenschap zorgt ervoor dat we in beide gevallen een topologische \mathbb{Z}_2 -invariant kunnen identificeren.

Topologie is de wiskunde die ziet op de eigenschappen van een object die onveranderd blijven bij een kleine vervorming. Een topologische invariant is een geheel getal dat zo'n object karakteriseert, in dit geval karakteriseert het getal een symmetrisch kristal. Het idee is dus dat de waarde van een topologische invariant niet kan veranderen zolang de natuur van het object min of meer hetzelfde blijft. Dus in ons geval, zolang het kristal symmetrisch is kan de invariant niet van waarde veranderen. Men spreekt van een \mathbb{Z}_n invariant als dit getal slechts n verschillende waarden kan aannemen. Met deze definitie op zak, is het nu tijd om aan te tonen dat 1-dimensionale kristallen met rotatie- of spiegel-symmetrie een topologische invariant kennen. We concentreren ons eerst op rotatie-symmetrische kristallen en generaliseren dan naar spiegel-symmetrische kristallen. Binnen iedere eenheidscel herkent men twee punten waaromheen men het kristal kan roteren, wij noemen deze twee punten A en B . Laat vervolgens N_A en N_B het aantal atomen zijn dat op deze punten zit. Dan geldt dat N_A en N_B slechts kunnen veranderen in veelvouden van twee. Immers als een atoom weg beweegt van zo'n

symmetrisch punt, dan moet een ander atoom in tegenovergestelde richting bewegen. Daarom zijn $\nu_A = (-1)^{N_A}$ en $\nu_B = (-1)^{N_B}$ twee topologische \mathbb{Z}_2 invarianten, die simpelweg het onderscheid maken tussen een rotatiesymmetrisch kristal met een even ($\nu_{A/B} = +1$) en oneven ($\nu_{A/B} = -1$) aantal atomen op A/B . Merk op dat voor het groene kristal $\nu_A = \nu_B = +1$. Op vergelijkbare wijze kan men in een spiegel-symmetrisch kristal de invarianten ν_A en ν_B definiëren die in dat geval aangeven of er een even of oneven aantal atomen in spiegelvlakken A en B zitten, zie Fig. 8.1 Voor het rood-blauwe kristal vinden we $\nu_A = \nu_B = -1$.

8.2 Ladingsophoping en topologie

In de voorgaande sectie hebben wij ons op de atomen (of beter de atoomkernen) van een kristal gericht. Dit proefschrift daarentegen beschouwt de topologie van de elektronen in een kristal. Het verschil tussen die twee zit hem primair in het feit dat de elektronen veel lichter zijn en daardoor zich veel meer als een kwantum-mechanische golf gedragen dan als een klassiek punt deeltje. Hierdoor is het niet mogelijk om de elektronische ν_A en ν_B te definiëren en observeren door simpelweg naar het kristal te kijken.

Wat wij hebben laten zien is dat men naar de ladingsophoping op de rand van een isolerend kristal moet kijken. Zo kan men bijvoorbeeld het groene kristal beschouwen met 1 elektron per eenheidscel. Door het golf-karakter van een elektron kan deze lading zich evenwichtig verdelen over de twee atomen. Dus ieder groen atoom herbergt een half elektron. Echter dicht bij de randen wijkt de lading per atoom af van een half. Dit is een direct gevolg van het feit dat de rand de kwantum-mechanische golven weerkaatst. Nu kan men deze verschillen gaan optellen om tot de totale linker- en rechterrandlading te komen. Aangezien de linker en rechter rand door middel van de rotatie-symmetrie aan elkaar gerelateerd zijn, volgt dat ze aan elkaar gelijk zijn. Gecombineerd met het feit dat het totaal aantal elektronen altijd een geheel getal moet zijn, volgt dat de randlading ofwel heeltallig is dan wel half-tallig. Het blijkt dat als we het kristal beëindigen met een dunne binding de randlading half-tallig is en anders heeltallig. Tegelijkertijd volgt uit ons onderzoek dat de elektronische ν_A in het half-tallige geval gelijk is aan -1 , en $+1$ in het heeltallige geval. Daarmee hebben we aangetoond dat de topologie van spiegel-, rotatie- en inversie-symmetrische kristallen kan

8 Samenvatting

worden geobserveerd door specifiek naar de randlading te kijken.

Vervolgens hebben we dit resultaat gegeneraliseerd. In het bijzonder hebben we gekeken naar isolerende kristallen met een even aantal elektronen per eenheidscel in afwezigheid van magnetische velden. In dat geval is de randlading altijd heeltallig, en daardoor lijkt topologie ons weinig nieuws te leren. Echter, in dit geval kan men het onderscheid maken tussen een randlading die even of oneven is. Wij hebben dit gerelateerd aan een nieuwe \mathbb{Z}_2 -invariant.

Aansluitend hebben wij de topologie beschouwd van 2-dimensionale kristallen, die ofwel inversie-, tweevoudig rotatie- of drievoudig rotatie-symmetrisch zijn. In de eerste twee gevallen kan men twee onafhankelijke \mathbb{Z}_2 invarianten definiëren, en in het laatste geval een enkele \mathbb{Z}_3 -invariant. Ook deze invarianten hebben wij gerelateerd aan de ladingsophoping op de rand. Daarnaast hebben wij aangetoond dat de ladingsophoping rondom een dislocatie deze topologie kan meten. Een dislocatie is een defect in atomaire kristalstructuur.

8.3 Dirac kegels

In bovenstaande kwam al kort aan bod dat elektronen veel lichter zijn dan de atomen. Hoe moeilijk of makkelijk een elektron zich kan voortbewegen wordt bepaald door de dispersie relatie. Zo volgt uit de dispersie relatie van een vrij elektron dat om twee keer zo snel te gaan, er vier keer zo veel energie nodig is. Meer specifiek is de dispersie relatie een grafiek die de energie van een elektron uitdrukt als functie van zijn impuls. De helling van deze grafiek is gelijk aan de snelheid van een elektron. In hoofdstuk 5 hebben wij ons gericht op 2-dimensionale Dirac halfmetalen. In deze materialen heeft de dispersie relatie de vorm van twee perfect op elkaar geplakte (Dirac) kegels, zie Fig. 8.2. Het punt waar de twee kegels elkaar raken kan worden gezien als een singulariteit in de dispersierelatie aangezien de helling daar niet goed gedefinieerd is. Doordat de energie van de elektronen lineair afhangt van de impuls, volgt dat elektronen met verschillende energie toch dezelfde snelheid hebben. Een bekend Dirac materiaal is grafeen, een honingraat rooster bestaande uit koolstof atomen. De vraag die wij in hoofdstuk 5 beantwoorden is in hoeverre andere roosters ook tot zo'n dispersie relatie kunnen leiden. Wij onderscheiden drie categorieën Dirac

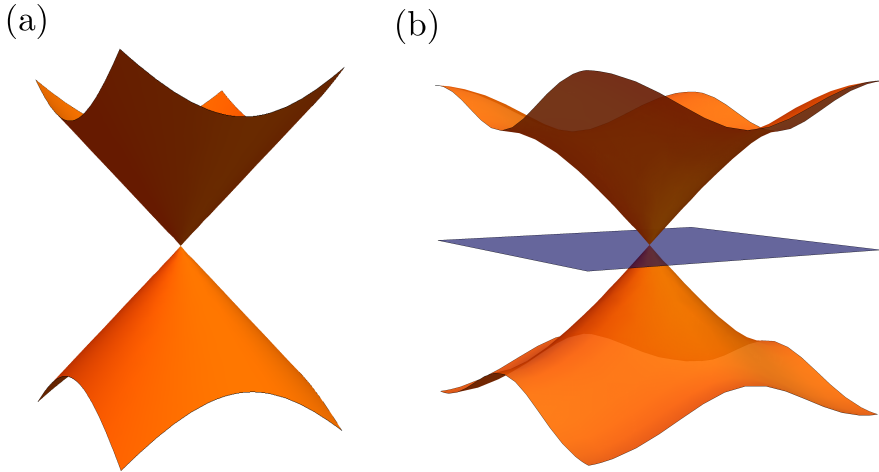


Figure 8.2: (a) Dirac kegels. (b) Lieb-achtige dispersie relatie.

materialen. Categorie I bevat het honingraat rooster. In dit geval kan de Dirac kegels gerelateerd worden aan een drievoudige rotatie-symmetrie en een spiegel-symmetrie. Categorie II daarentegen bevat materialen waarbij de Dirac kegels gestabiliseerd worden door een spiegel-symmetrie eventueel gecombineerd met een rotatie-symmetrie. Tot slot bevat categorie III Dirac materialen die inversie-, rotatie- en spiegel-symmetrisch zijn. Wij illustreren vervolgens de resultaten met een aantal minimale modellen en relateren onze resultaten aan zogenaamde ab-initio berekeningen.

Het is onze hoop dat deze inzichten ook van nut kunnen zijn in de zoektocht naar nieuwe Dirac materialen. Naast echte kristalroosters, kan men echter ook naar kunstmatige roosters kijken. Een voorbeeld hiervan wordt gegeven in hoofdstuk 6 dat het resultaat is van een experimentele samenwerking met de groepen van Daniël Vanmaekelbergh en Ingmar Swart. Hier tonen wij aan dat door koolstofmonoxide moleculen te positioneren op een koperoppervlak, wij de dispersie relatie van de koper elektronen kunnen aanpassen. Meer specifiek hebben we aangetoond dat de elektronen in dit kunstmatige rooster een Lieb-achtige dispersie relatie hebben. Dat wil zeggen de dispersie relatie ziet eruit als twee elkaar rakende kegels, met een vlak

ertussen, zie Fig. 8.2.

8.4 En hoe nu verder?

Het is onze hoop dat dit proefschrift als inspiratiebron kan dienen voor nieuw onderzoek. We zullen hier kort een paar mogelijkheden bespreken.

In hoofdstukken 3 en 4 hebben wij specifiek gekeken naar ladingsophoping op de rand en rondom dislocaties. Het ligt voor de hand om te bestuderen de topologie van de elektronen zich ook uit in de ladingsophoping rondom andere defecten, in het bijzonder op een hoek of rondom een disclinitie. Dit is met name interessant in het licht van de recente aandacht voor hogere orde topologische isolatoren.

In relatie tot hoofdstukken 5 en 6 is het interessant om te kijken in hoeverre de besproken Dirac materialen kunnen worden gerealiseerd in kunstmatige roosters. Daarnaast bieden kunstmatige roosters door hun grote roosterconstante een geschikt platform om de ladingsophoping rondom defecten te beschouwen.

Al met al is er nog genoeg te ontdekken, laten wij dan ook afsluiten met een heerlijk cliché: “Further research is needed”.

List of Publications

This thesis is based on the following publications:

1. Chapter 2 is based on G. van Miert, C. Ortix, and C. Morais Smith. Topological origin of edge states in inversion-symmetric insulators and semi-metals. *2D Materials* 4, 015023 (2017).
2. Chapter 3 is based on G. van Miert and C. Ortix. Excess charges as a probe of one-dimensional topological crystalline insulating phases. *Phys. Rev. B* 96, 235130 (2017).
3. Chapter 4 is based on G. van Miert and C. Ortix. Dislocation charges reveal two-dimensional topological crystalline invariants. *ArXiv*:1802.00715.
4. Chapter 5 is based on G. van Miert and C. Morais Smith. Dirac cones beyond the honeycomb lattice: a symmetry-based approach. *Phys. Rev. B* 93, 035401 (2016).
5. Chapter 6 is partially based on M. Slot, T. Gardenier, P. Jacobse, G. van Miert, S. Kempkes, S. Zevenhuizen, C. Morais Smith, D. Vanmaekelbergh, and I. Swart. Experimental realization and characterization of an electronic Lieb lattice. *Nat. Phys.* 13, 672 (2017).

The author also contributed to the following works which are not part of this thesis:

1. G. van Miert and C. Ortix. Symmetry-based indicators for roto-inversion-symmetric insulators. *In preparation*.
2. F. Kunst, G. van Miert, and E. Bergholtz. Generalization of exactly solvable surface state solutions. *In preparation*.

List of Publications

3. F. Kunst, G. van Miert, and E. Bergholtz. Lattice models with exactly solvable topological hinge and corner states.
ArXiv:1712.07911.
4. G. van Miert, V. Juricic, and C. Morais Smith. Tight-binding theory of spin-orbit coupling in graphynes.
Phys. Rev. B 90, 195414 (2014).
5. G. van Miert, C. Morais Smith, and V. Juricic. High-Chern-number bands and tunable Dirac cones in β -graphyne.
Phys. Rev. B 90, 081406(R) (2014).

Bibliography

- [1] M.J. Rice and E.J. Mele, Phys. Rev. Lett. **49**, 1455 (1982).
- [2] M. Z. Hasan and C. L. Kane, Rev. Mod. Phys. **82**, 3045 (2010).
- [3] X.-L. Qi and S.-C. Zhang, Rev. Mod. Phys. **83**, 1057 (2011).
- [4] A. Altland and M. R. Zirnbauer, Phys. Rev. B **55**, 1142 (1997).
- [5] A.P. Schnyder, S. Ryu, A. Furusaki, and A.W.W. Ludwig, Phys. Rev. B **78**, 195125 (2008).
- [6] A. Kitaev, AIP Conf. Proc. **1134**, 22 (2009).
- [7] S. Ryu, A.P. Schnyder, A. Furusaki, and A.W.W. Ludwig, New J. Phys. **12**, 065010 (2010).
- [8] D. J. Thouless, M. Kohmoto, M. P. Nightingale, and M. den Nijs, Phys. Rev. Lett. **49**, 405 (1982).
- [9] C. L. Kane and E. J. Mele, Phys. Rev. Lett. **95**, 146802 (2005).
- [10] R. B. Laughlin, Phys. Rev. B **23**, 5632 (1981).
- [11] S. Ryu and Y. Hatsugai, Phys. Rev. Lett. **89**, 077002 (2002).
- [12] P. Delplace, D. Ullmo, and G. Montambaux, Phys. Rev. B **84**, 195452 (2011).
- [13] M. Ezawa, New J. Phys. **16**, 115004 (2014).
- [14] R. D. King-Smith and D. Vanderbilt, Phys. Rev. B **47**, 1651(R) (1993).
- [15] J. Zak, Phys. Rev. Lett. **62**, 2747 (1989).
- [16] T.L. Hughes, E. Prodan, B.A. Bernevig, Phys. Rev. B **83**, 245132 (2011).

Bibliography

- [17] F. Wegner, *Z. Phys. B* **36**, 209 (1980).
- [18] L. Li, Y. Yu, G. Jun Ye, Q. Ge, X. Ou, H. Wu, D. Feng, X. Hui Chen, and Y. Zhang, *Nat Nanotechnol* **9**, 372 (2014).
- [19] M. Buscema, D.J. Groenendijk, S.I. Blanter, G.A. Steele, H.S.J. van der Zant, and A. Castellanos-Gomez, *Nano Lett.* **14**, 3347 (2014).
- [20] S. P. Koenig, R. A. Doganov, H. Schmidt, A. H. Castro Neto, and B. Özyilmaz, *Appl. Phys. Lett.* **104**, 103106 (2014).
- [21] H. Liu, A. T. Neal, Z. Zhu, D. Tomanek, and P. D. Ye, *ACS Nano* **8**, 4033 (2014).
- [22] F. Xia, H. Wang, and Y. Jia, *Nat. Commun.* **5**, 4458 (2014).
- [23] A. N. Rudenko, S. Yuan, and M. I. Katsnelson, *Phys. Rev. B* **92**, 085419 (2015).
- [24] Q. Liu, X. Zhang, L. B. Abdalla, A. Fazzio, and A. Zunger, *Nano Lett.* **15**, 1222 (2015).
- [25] R.-J. Slager, A. Mesaros, V. Juricic, and J. Zaanen, *Nat. Phys.* **9**, 98 (2013).
- [26] A. R. Akhmerov and C. W. J. Beenakker, *Phys. Rev. B* **77**, 085423 (2008).
- [27] C. Pauly, B. Rasche, K. Koepf, M. Liebmann, M. Pratzner, M. Richter, J. Kellner, M. Eschbach, B. Kaufmann, L. Plucinski, C. M. Schneider, M. Ruck, J. van den Brink, and M. Morgenstern, *Nat. Phys.* **11**, 338 (2015).
- [28] J. Kim, S. S. Baik, S. H. Ryu, Y. Sohn, S. Park, B.-G. Park, J. Denlinger, Y. Yi, H. J. Choi, and K. S. Kim, *Science* **349**, 723 (2015).
- [29] S.S. Baik, K.S. Kim, Y. Yi, and H.J. Choi, *Nano Lett.* **15**, 7788 (2015).
- [30] J.-H. Park, G. Yang, J. Klinovaja, P. Stano, D. Loss, *Phys. Rev. B* **94**, 075416 (2016).

- [31] Y.-H. Chan, C.-K. Chiu, M. Y. Chou, and A. P. Schnyder, *Phys. Rev. B* **93**, 205132 (2016).
- [32] M. Diez, D.I. Pikulin, I.C. Fulga, and J. Tworzydło, *New. J. Phys.* **17**, 043014 (2015).
- [33] Y. Kim, B.J. Wieder, C.L. Kane, and A.M. Rappe, *Phys. Rev. Lett.* **115**, 036806 (2015).
- [34] L. Fu, C.L. Kane, and E.J. Mele, *Phys. Rev. Lett.* **98**, 106803 (2007).
- [35] J.E. Moore and L. Balents, *Phys. Rev. B* **75**, 121306(R) (2007).
- [36] L. Fu and C. L. Kane, *Phys. Rev. B* **76**, 045302 (2007).
- [37] H.J. Zhang, C.-X. Liu, X.-L. Qi, Z. Fang, and S.-C. Zhang, *Nat. Phys.* **5**, 438 (2009).
- [38] C.-X. Liu, X.-L. Qi, H.J. Zhang, X. Dai, Z. Fang, and S.-C. Zhang, *Phys. Rev. B* **82**, 045122 (2010).
- [39] B. Rasche, A. Isaeva, M. Ruck, S. Borisenko, V. Zabolotnyy, B. Büchner, K. Koepf, C. Ortix, M. Richter, and J. van den Brink, *Nat. Mater.* **12**, 422 (2013).
- [40] L. Fu, *Phys. Rev. Lett.* **106**, 106802 (2011).
- [41] T.H. Hsieh, H. Lin, J. Liu, W. Duan, A. Bansil, and L. Fu, *Nat. Commun.* **3**, 982 (2012).
- [42] Y. Tanaka, Z. Ren, T. Sato, K. Nakayama, S. Souma, T. Takahashi, K. Segawa, Y. Ando, *Nat. Phys.* **8**, 800 (2012).
- [43] Y. Ando and L. Fu, *Ann. Rev. Condens. Matter Phys.* **6**, 361 (2015).
- [44] A.A. Burkov and L. Balents, *Phys. Rev. Lett.* **107**, 127205 (2011).
- [45] X. Wan, A.M. Turner, A. Vishwanath, and S.Y. Savrasov, *Phys. Rev. B* **83**, 205101 (2011).
- [46] S.-M. Huang, S.-Y. Xu, I. Belopolski, C.-C. Lee, G. Chang, B.K. Wang, N. Alidoust, G. Bian, M. Neupane, C. Zhang, S. Jia, A. Bansil, H. Lin, and M. Z. Hasan, *Nat. Commun.* **6**, 7373 (2015).

Bibliography

- [47] B.Q. Lv, H.M. Weng, B.B. Fu, X.P. Wang, H. Miao, J. Ma, P. Richard, X.C. Huang, L.X. Zhao, G.F. Chen, Z. Fang, X. Dai, T. Qian, and H. Ding, *Phys. Rev. X* **5**, 031013 (2015).
- [48] S.-Y. Xu, I. Belopolski, N. Alidoust, M. Neupane, G. Bian, C. Zhang, R. Sankar, G. Chang, Z. Yuan, C.-C. Lee, S.-M. Huang, H. Zheng, J. Ma, D.S. Sanchez, B.K.Wang, A. Bansil, F. Chou, P.P. Shibayev, H. Lin, S. Jia, and M. Z. Hasan, *Science* **349**, 613 (2015).
- [49] A. Lau, K. Koepernik, J. van den Brink, and C. Ortix, *Phys. Rev. Lett.* **119**, 076801 (2017).
- [50] K. von Klitzing, G. Dorda, and M. Pepper, *Phys. Rev. Lett.* **45**, 494 (1980).
- [51] C. L. Kane and E. J. Mele, *Phys. Rev. Lett.* **95**, 226801 (2005).
- [52] B.A. Bernevig, T.L. Hughes, and S.-C. Zhang, *Science* **314**, 1757 (2006).
- [53] M. König, S. Wiedmann, C. Brüne, A. Roth, H. Buhmann, L.W. Molenkamp, X.-L. Qi, and S.-C. Zhang, *Science* **318**, 766 (2007).
- [54] J. Friedel, *Philos. Mag.* **43**, 153 (1952).
- [55] E. Prodan, *Phys. Rev. B* **73**, 085108 (2006).
- [56] S. Gangadharaiah, L. Trifunovic, and D. Loss, *Phys. Rev. Lett.* **108**, 136803 (2012).
- [57] P. Szumniak, J. Klinovaja, and D. Loss, *Phys. Rev. B* **93**, 245308 (2016).
- [58] J.W. Rhim, J. Behrends, J.H. Bardarson, *Phys. Rev. B* **95**, 035421 (2017).
- [59] D. Vanderbilt and R. D. King-Smith, *Phys. Rev. B* **48**, 4442 (1993).
- [60] C.-K. Chiu, H. Yao, and S. Ryu, *Phys. Rev. B* **88**, 075142 (2013).
- [61] K. Shiozaki and M. Sato, *Phys. Rev. B* **90**, 165114 (2014).

- [62] A. Lau, C. Ortix, J. van den Brink, Phys. Rev. Lett. **115**, 216805 (2015).
- [63] A. Lau, J. van den Brink, and C. Ortix, Phys. Rev. B **94**, 165164 (2016).
- [64] L. Fu and C. L. Kane, Phys. Rev. B **74**, 195312 (2006).
- [65] D. J. Thouless, Phys. Rev. B **27**, 6083 (1983).
- [66] G. Rigolin, G. Ortiz, and V.H. Ponce, Phys. Rev. A **78**, 052508 (2008).
- [67] W. Kohn, Phys. Rev. **115**, 809 (1959).
- [68] J. Zak, Phys. Rev. B **32**, 2218 (1985).
- [69] Q. Niu, Phys. Rev. B **33**, 5368 (1986).
- [70] C. Fang, M. J. Gilbert, and B.A. Bernevig, Phys. Rev. B **86** 115112 (2012).
- [71] A. Alexandradinata, X. Dai, B.A. Bernevig, Phys. Rev. B **89**, 155114 (2014).
- [72] W. P. Su, J. R. Schrieffer, and A. J. Heeger, Phys. Rev. Lett. **42**, 1698 (1979).
- [73] F. de Juan, A. Regg, and D.-H. Lee, Phys. Rev. B **89**, 161117(R) (2014).
- [74] V. Jurii, A. Mesaros, R.-J. Slager, and J. Zaanen, Phys. Rev. Lett. **108**, 106403 (2012).
- [75] W. A. Benalcazar, J. C. Y. Teo, and T. L. Hughes, Phys. Rev. B **89**, 224503 (2014).
- [76] G. van Miert and C. Ortix, Phys. Rev. B **96**, 235130 (2017).
- [77] P. Jadaun, D. Xiao, Q. Niu, and S.K. Banerjee, Phys. Rev. B **88**, 085110 (2013).
- [78] J.C.Y. Teo and T.L. Hughes, Phys. Rev. Lett. **111**, 047006 (2013).

Bibliography

- [79] F. D. M. Haldane, *Phys. Rev. Lett.* **61**, 2015 (1988).
- [80] A. H. Castro Neto, F. Guinea, N. M. R. Peres, K. S. Novoselov, and A. K. Geim, *Rev. Mod. Phys.* **81**, 109 (2009).
- [81] M. I. Katsnelson, K. S. Novoselov, and A. K. Geim, *Nat. Phys.* **2**, 620 (2006).
- [82] Y. Zhang, Y.W. Tan, H.L. Stormer, and P. Kim, *Nature* **438**, 201 (2005).
- [83] P. Mir, M. Audiffred, and T. Heine, *Chem. Soc. Rev.* **43**, 6537 (2014).
- [84] P. Vogt, P. De Padova, C. Quaresima, J. Avila, E. Frantzeskakis, M.C. Asensio, A. Resta, B. Ealet, and G. Le Lay, *Phys. Rev. Lett.* **108**, 155501 (2012).
- [85] M.E. Dávila, L. Xian, S. Cahangirov, A. Rubio, and G. Le Lay, *New J. Phys.* **16**, 095002 (2014).
- [86] F. Zhu, W. Chen, Y. Xu, C. Gao, D. Guan, C. Liu, D. Qian, S.C. Zhang, and J. Jia, *Nat. Mat.* **14**, 1020 (2015).
- [87] L. Tao, E. Cinquanta, D. Chiappe, C. Grazianetti, M. Fanciulli, M. Dubey, A. Molle, and D. Akinwande, *Nature Nanotechnology* **10**, 227 (2015).
- [88] C.C. Liu, H. Jiang, and Y. Yao, *Phys. Rev. B* **84**, 195430 (2011).
- [89] D. Pacilé, J.C. Meyer, C.Ö. Girit, and A. Zettl, *Appl. Phys. Lett.* **92**, 133107 (2008).
- [90] S. S. Lin, *J. Phys. Chem. C* **116**, 3951 (2012).
- [91] D. Malko, C. Neiss, F. Vines, and A. Görling, *Phys. Rev. Lett.* **108**, 086804 (2012).
- [92] L.Z. Zhang, Z.F. Wang, Z.M. Wang, S.X. Du, H.-J. Gao, and F. Liu, *J. Phys. Chem. Lett.* **6**, 2959 (2015).
- [93] G. X. Li, Y. L. Li, H. B. Liu, Y. B. Guo, Y. J. Li, and D. B. Zhu, *Chem. Commun.* **46**, 3256 (2010).

- [94] L. Z. Zhang, Z. F. Wang, S. X. Du, H.-J. Gao, and F. Liu, *Phys. Rev. B* **90**, 161402(R) (2014).
- [95] X.-F. Zhou, X. Dong, A.R. Oganov, Q. Zhu, Y. Tian, and H.-T. Wang, *Phys. Rev. Lett.* **112**, 085502 (2014).
- [96] S. Katayama, A. Kobayashi, and Y. Suzumura, *J. Phys. Soc. Jpn.* **75**, 054705 (2006).
- [97] J. von Neumann and E. Wigner, *Physik Z.* **30**, 467 (1929).
- [98] K. Asana and C. Hotta, *Phys. Rev. B* **83**, 245125 (2011).
- [99] L. Cano-Cortés, C. Ortix, and J. van den Brink, *Phys. Rev. Lett.* **111**, 146801 (2013).
- [100] K. Sun, H. Yao, E. Fradkin, and S. A. Kivelson, *Phys. Rev. Lett.* **103**, 046811 (2009).
- [101] M.S. Dresselhaus, G. Dresselhaus, A. Jorio, *Group Theory Application to the Physics of Condensed Matter* (Springer, 2008).
- [102] J.M. Hou, W.X. Yang, and X.J. Liu, *Phys. Rev. A* **79**, 043621 (2009).
- [103] G. van Miert, C. Morais Smith, and V. Juričić, *Phys. Rev. B* **90**, 081406(R) (2014).
- [104] G. van Miert, V. Juričić, and C. Morais Smith, *Phys. Rev. B* **90**, 195414 (2014).
- [105] G. Li, A. Luican, J.M.B. Lopes dos Santos, A.H. Castro Neto, A. Reina, J. Kong, and E.Y. Andrei, *Nat. Phys.* **6**, 109 (2010).
- [106] E. Kalesaki, C. Delerue, C. Morais Smith, W. Beugeling, G. Allan, and D. Vanmaekelbergh, *Phys. Rev. X* **4**, 011010 (2014).
- [107] M. Polini, F. Guinea, M. Lewenstein, H.C. Manoharan, and V. Pellegrini, *Nature Nanotechnology* **8**, 625 (2013).
- [108] P. Soltan-Panahi, J. Struck, P. Hauke, A. Bick, W. Plenkers, G. Meineke, C. Becker, P. Windpassinger, M. Lewenstein, and K. Sengstock, *Nat. Phys.* **7**, 434 (2011).

Bibliography

- [109] G. Montambaux, F. Pichon, J.-N. Fuchs, and M.O. Goerbig, *Phys. Rev. B* **80**, 153412 (2009).
- [110] S. Koghee, L.K. Lim, M.O. Goerbig, and C. Morais Smith, *Phys. Rev. A* **85**, 023637 (2012).
- [111] L. Tarruell, D. Greif, T. Uehlinger, G. Jotzu, and T. Esslinger, *Nature* **483**, 303 (2012).
- [112] B.J. DeSalvo, M. Yan, P.G. Mickelson, Y.N. Martinez de Escobar, and T. C. Killian, *Phys. Rev. Lett.* **105**, 030402 (2010).
- [113] O. Boada, A. Celi, J. I. Latorre, and M. Lewenstein, *Phys. Rev. Lett.* **108**, 133001 (2012).
- [114] A. Tadjine, G. Allan, and C. Delerue, *Phys. Rev. B* **94**, 075441 (2016).
- [115] K.K. Gomes, W. Mar, W. Ko, F. Guinea, and H.C. Manoharan, *Nature* **483**, 306 (2012).
- [116] C.R. Moon, L.S. Mattos, B.K. Foster, G. Zeltzer, W. Ko, and H.C. Manoharan, *Science* **319**, 782 (2008).
- [117] C.R. Moon, L.S. Mattos, B.K. Foster, G. Zeltzer, and H.C. Manoharan, *Nature Nanotechnology* **4**, 167 (2009).
- [118] M. Ropo, S. Paavilainen, J. Akola, and E. Räsänen, *Phys. Rev. B* **90**, 241401(R) (2014).
- [119] W.-X. Qiu, S. Li, J.-H. Gao, Y. Zhou, and F.-C. Zhang, *Phys. Rev. B* **94**, 241409(R) (2016).
- [120] L. Bürgi, L. Petersen, H. Brune, and K. Kern, *Surf. Sci.* **447**, L157L161 (2000).
- [121] J. Kröger, L. Limot, H. Jensen, R. Berndt, and P. Johansson, *Phys. Rev. B* **70**, 033401 (2004).
- [122] S. Li, W.-X. Qiu, and J.-H. Gao, *Nanoscale* **8**, 12747 (2016).
- [123] R. Drost, T. Ojanen, A. Harju, and P. Liljeroth, *Nat. Phys.* **13**, 668 (2017).
- [124] W. Uijttewaal, Bachelor's thesis, Utrecht University (2018).

CV

Ik ben geboren op 15 februari 1990 te Amstelveen. Het middelbaar onderwijs heb ik aan het St. Ignatiusgymnasium te Amsterdam gevolgd. Aansluitend ben ik in 2008 Natuur- en Wiskunde gaan studeren aan de Universiteit Utrecht. Vervolgens ben ik aan diezelfde universiteit in 2011 aan de Master Theoretical Physics begonnen. Deze opleiding heb ik in 2014 afgerond met een scriptie over grafynen, onder begeleiding van Prof. Dr. C. Morais Smith. Hierna ben ik aan de Universiteit Utrecht begonnen aan mijn promotieonderzoek onder begeleiding van Prof. Dr. C. de Morais Smith en Dr. C. Ortix.